

Molecular insights of the human zinc transporter hZIP4

by

Sagar Antala

A Dissertation

Submitted to the Faculty

of the

WORCESTER POLYTECHNIC INSTITUTE

in partial fulfillment of the requirements for the

Degree of Doctor of Philosophy

in

Biochemistry

March 2016

Approved:

Dr. Robert E. Dempski

Major Advisor

Dr. José Argüello

Committee Member

Dr. Arne Gericke

Committee Member

Dr. Haley Melikian

Committee Member

Abstract

Zinc is the second most abundant transition metal in the body. Despite the fact that hundreds of biomolecules require zinc for proper function and/or structure, the mechanism of zinc transport into cells is not well-understood. ZnT and ZIP proteins are members of the SoLute Carrier (SLC) family of membrane transporters and are one of the principal family of proteins involved in regulating intracellular zinc concentration. ZnT (Zinc Transporters) decrease the cytosolic concentration of zinc, while ZIP (for Zinc or Iron regulated Proteins) transporters function to increase the cytosolic zinc concentration. Mutations in one member of the ZIP family of proteins, the human ZIP4 (hZIP4; SLC39A4) protein, can result in the disease *acrodermatitis enteropathica* (AE). AE is characterized by growth retardation, diarrhea, behavioral disturbances and neurological disorders. While the cellular distribution of hZIP4 protein expression has been elucidated, the cation specificity, kinetic parameters of zinc transport, residues involved in cation translocation and structural details are unresolved questions.

To elucidate cation specificity and kinetic parameters of zinc transport by hZIP4, we have established a high signal to noise zinc uptake assay following heterologous expression of hZIP4 in *Xenopus laevis* oocytes. The results from our experiments have demonstrated that zinc, copper (II) and nickel can be transported by hZIP4 when the cation concentration is in the micromolar range. We have also identified a nanomolar affinity for copper (II) and zinc transport by hZIP4. In contrast, under nanomolar conditions, nickel can bind, but is not transported by hZIP4. Finally, labeling of hZIP4 with maleimide or DEPC indicates that extracellularly accessible histidine, but not cysteine, residues are required, either directly or indirectly, for cation uptake. The results from our experiments describe at least two coordination sites for divalent cations and provide a new framework to investigate the ZIP family of proteins.

Members of the ZIP family of proteins are a central participant in transition metal homeostasis as they function to increase the cytosolic concentration of zinc and/or iron. However the lack of a crystal structure hinders elucidation of the molecular mechanism of ZIP transport proteins. We employed GREMLIN, a co-evolution based contact prediction approach in conjunction with the ROSETTA structure prediction program to construct a structural model of the human (h) ZIP4 transporter. The resulting computational data is best fit by modeling hZIP4 as a dimer. Mutagenesis of residues that comprise a central putative hZIP4 transmembrane transition metal coordination site in the structural model alter the kinetics and specificity of hZIP4. Comparison of the hZIP4 dimer model to all known membrane protein structures identifies the twelve transmembrane monomeric PiPT, a member of the major facilitator superfamily (MFS), as a likely structural homolog.

hZIP4 has eight transmembrane domains and encodes a large intracellular loop between transmembrane domains III and IV, M3M4. Previously, it has been postulated that this domain regulates hZIP4 levels in the plasma membrane in a zinc-dependent manner. To elucidate the zinc binding properties of the large intracellular loop of hZIP4, we have recombinantly expressed and purified M3M4 and showed that this fragment binds two zinc ions. Using a combination of site-directed mutagenesis, metal binding affinity assays, and X-ray absorption spectroscopy, we demonstrated that the two Zn^{2+} ions bind sequentially, with the first Zn^{2+} binding to a CysHis3 site with a nanomolar binding affinity, and the second Zn^{2+} binding to a His4 site with a weaker affinity. Circular dichroism spectroscopy revealed that the M3M4 peptide is intrinsically disordered, with only a small structural change induced upon Zn^{2+} coordination. Our data supports a model in which the intracellular M3M4 domain senses high cytosolic Zn^{2+} concentrations and regulates the plasma membrane levels of the hZIP4 transporter in response to Zn^{2+} binding.

Acknowledgements

I would like to thank my advisor, Robert E. Dempski, for being supportive to all my endeavors during my PhD studies. He has been extremely supportive throughout this journey.

I would like to thank my committee members José Argüello, Arne Gericke and Haley Melikian for their constructive criticism and suggestions for making my work more impactful.

I would like to thank my past and current lab members Tuong-Vi Nguyen, Ryan Richards and Elizabeth Bafaro for their support and playing active role in minting fresh ideas for future directions.

I would like to thank Argüello lab for their friendship and support especially Sarju Patel and Teresita Padilla. I would also like to thank Gericke lab for their help at various stages of my PhD.

I would also like to thank Ann Mondor for providing constant support by taking care of all the non-academic work.

Lastly, I would like to thank my parents and brother for their constant support and encouragement.

Abbreviations

AE: <i>Acrodermatitis enteropathica</i>	IPTG: Isopropyl- β -D-thiogalactopyranoside
ATP: Adenosine triphosphate	KGlu: Potassium Gluconate
AAS: Atomic absorption spectroscopy	M3M4: Loop between transmembrane III and IV
CD: Circular dichroism	MFS: Major facilitator superfamily
CPM: Counts per minute	MOPS: 4-morpholinepropanesulfonic acid
DCCD: <i>N,N'</i> -dicyclohexyl carbodiimide	mZIP4: Mouse ZIP4
DDM: N-dodecyl-beta D-maltoside	NaGlu: Sodium Gluconate
DEPC: Diethyl pyrocarbonate	NaCit: Sodium Citrate
DIDS: 4,4'-diisothiocyanatostilbene-2,2'-disulfonic acid	NEM: N-ethylmaleimide
DLS: Dynamic light scattering	NTA: Nitrilotriacetic acid
DM: N-Decyl- β -D-Maltopyranoside	NTAde Cage: NTA decarboxylation photoCage
DPM: Disintegrations per minute	PBS: Phosphate buffer saline
EDTA: Ethylenediaminetetraacetic acid	PMSF: Phenylmethanesulfonyl fluoride
EGTA: Ethylene glycol tetraacetic acid	PPII: Poly-L-proline type II
EXAFS: Extended X-ray absorption fine structure	SDS: Sodium dodecyl sulfate
HEPES: 4-(2-Hydroxyethyl) piperazine-1-ethanesulfonic acid	SLC: SoLute Carrier
hZIP4: Human ZIP4	TCEP: Tris(2-chloroethyl) phosphate
IDA: Iminodiacetic acid	TM: Transmembrane
IDPs: Intrinsically disordered proteins	WT: Wild-type hZIP4
IDPRs: Intrinsically disordered protein regions	XANES: X-ray absorption near edge structure
	XAS: X-ray absorption spectroscopy

ZIP: Zinc or Iron regulated Proteins

ZnT: Zinc Transporters

Publications

1. **Antala S**, and Dempksi RE (2012) The human ZIP4 transporter has two distinct binding affinities and mediates transport of multiple transition metals. *Biochemistry*. 51, 963-973.
2. **Antala S***, Ovchinnikov S*, Kamisetty H, Baker D, and Dempksi RE (2015) Computation and functional studies provide a model for the structure of the Zinc transporter hZIP4. *J. Biol. Sci.*290, 17796-17805.
3. Bafaro EM*, **Antala S***, Nguyen TV, Dzul SP, Doyon B, Stemmler TL, and Dempksi RE (2015) The large intracellular loop of hZIP4 is an intrinsically disordered zinc binding domain. *Metallomics*. 7, 1319-1330.
4. Basa PN, **Antala S**, Dempksi RE, and Burdette SC (2015) A Zinc (II) Photocage Based on a Decarboxylation Metal Ion Release Mechanism for Investigating Homeostasis and Biological Signaling. *Angew. Chem.* 127, 13219-13223.

Table of Contents

1	INTRODUCTION	1
1.1	Zinc: An essential micronutrient for humans	2
1.2	Zinc inside the cell	2
1.3	Zinc biochemical properties.....	3
1.4	Proteins important for zinc cellular distribution	5
1.4.1	Metallothionein.....	5
1.4.2	ZnT proteins.....	7
1.4.3	ZIP proteins.....	8
1.5	hZIP4 protein	12
2	The Human ZIP4 Transporter Has Two Distinct Binding Affinities and Mediates Transport of Multiple Transition Metals	18
2.1	Introduction.....	19
2.2	Materials and method.....	20
2.2.1	Reagents.....	20
2.2.2	Plasmid construct	20
2.2.3	Preparation of <i>Xenopus laevis</i> oocytes for <i>in situ</i> expression of hZIP4.....	20
2.2.4	<i>In vitro</i> expression of hZIP4	21
2.2.5	Immunofluorescence microscopy	21
2.2.6	Uptake assay	22
2.2.7	Maleimide and DEPC labeling of hZIP4	23

2.2.8	Driving force for hZIP4 mediated $^{65}\text{Zn}^{2+}$ transport.....	23
2.2.9	Zn-Cage compounds and Zn^{2+} transport in <i>X. laevis</i> oocytes	24
2.3	Results.....	27
2.3.1	hZIP4 localizes on <i>Xenopus laevis</i> oocytes membrane surface	27
2.3.2	hZIP4 transports zinc in <i>X. laevis</i> oocytes	27
2.3.3	Determination of K_m and V_{max} for hZIP4-mediated zinc uptake	30
2.3.4	hZIP4 may transport multiple transition metals.....	32
2.3.5	hZIP4 can transport nickel	34
2.3.6	hZIP4 transports copper (II) in oocytes	36
2.3.7	Extracellular histidine residues are important for hZIP4 mediated $^{65}\text{Zn}^{2+}$ transport 36	
2.3.8	Multiple factors were tested to define the driving force for hZIP4 mediated $^{65}\text{Zn}^{2+}$ transport 40	
2.3.9	hZIP4 expressing <i>X.laevie</i> oocytes can be used for Zn^{2+} photocage compound in evaluating their application in biological system.....	40
2.4	Discussion.....	45
3.	Computational modeling and functional studies provide a structural scaffold for the zinc transporter hZIP4	50
3.1	Introduction.....	51
3.2	Materials and Methods.....	54
3.2.1	Reagents.....	54
3.2.2	Expression of hZIP4 in <i>Xenopus laevis</i> oocytes	54

3.2.3	Radio-isotope uptake assay	54
3.2.4	Detection of hZIP4 surface expression in oocytes	55
3.2.5	Computational modelling of the hZIP4 protein (In collaboration with the David Baker lab, University of Washington and Howard Hughes Medical Institute)	55
3.2.5.1	Prediction of contact residues in hZIP4 protein	55
3.2.5.2	Rosetta Membrane ab initio modeling for hZIP4	56
3.2.6	Oligomeric state of hZIP4	61
3.2.7	Glycosylation of hZIP4	61
3.3	Results	62
3.3.1	The effect of histidine to alanine mutations on hZIP4 zinc transport	62
3.3.2	Histidine 624 is essential for biometal translocation	67
3.3.3	Residues contribute to cation selectivity of ZIP transporters	67
3.3.4	Residue-residue contacts predicted from co-evolution (in collaboration with the David Baker lab)	70
3.3.5	Structural Alignment of hZIP4 with membrane protein structures (in collaboration with the David Baker lab)	73
3.3.6	Oligomeric State of hZIP4	73
3.4	Discussion	79
4.	The large intracellular loop of hZIP4 is an intrinsically disordered zinc binding domain	84
4.1	Introduction	85
4.2	Materials and Methods	88
4.2.1	Materials	88

4.2.2	Bioinformatics.....	88
4.2.3	Molecular cloning	88
4.2.4	Protein expression, purification and labeling.....	89
4.2.5	Circular dichroism spectroscopy.....	89
4.2.6	Binding affinity (K_d) determination of M3M4.....	90
4.2.7	Atomic absorption spectroscopy	91
4.2.8	X-ray absorption spectroscopy.....	91
4.3	Results.....	93
4.3.1	The intracellular loop of hZIP4 is disordered	93
4.3.2	The intracellular M3M4 domain binds Zn^{2+} with nanomolar affinity	97
4.3.3	Histidine and cysteine residues are involved in Zn^{2+} binding in the M3M4 domain 98	
4.3.4	EXAFS reveals the coordination geometry of Zn^{2+} bound to M3M4 (In collaboration with Timothy L. Stemmler Lab, Wayne State University)	102
4.3.5	Structural changes to the M3M4 domain upon Zn^{2+} binding.....	107
4.4	Discussion	109
5.	Future work.....	113
6.1	Define the driving force conditions for hZIP4.....	114
6.2	Oligomeric state of hZIP4.....	115
6.	References.....	116

List of Figures

Figure 1. Zn ²⁺ coordination geometries	4
Figure 2. Cellular Zn ²⁺ homeostasis.....	6
Figure 3. Predicted schematic diagram of the human ZIP4 protein.....	13
Figure 4. Representative images of three oocytes injected with hZIP4 mRNA tagged with Strep tag on the C-terminus and probed with Chromeo488-conjugated anti-Strep antibody.....	28
Figure 5. Evaluation of ⁶⁵ Zn ²⁺ radioisotope uptake assay in hZIP4 expressing oocytes.....	29
Figure 6. Zinc affinity and transport by hZIP4	31
Figure 7. Competition of ⁶⁵ Zn ²⁺ uptake with a series of divalent cations in WT hZIP4 expressing oocytes	33
Figure 8. Nickel affinity and transport by hZIP4	35
Figure 9. Time course and kinetics of hZIP4-mediated Cu ²⁺ uptake.....	37
Figure 10. Extracellular histidines are involved in zinc translocation.....	39
Figure 11. Effect of pH, salt concentration on hZIP4 mediated Zn ²⁺ transport	41
Figure 12. Effect of different buffers on hZIP4 mediated Zn ²⁺ transport	42
Figure 13. Evaluation of hZIP4 expressing oocytes as a model system to test photocaged Zn ²⁺ in biological system	43
Figure 14. Sigmoidal distance restraint function	58
Figure 15. Contact map showing top co-evolved TM residues in hZIP4	59
Figure 16. Distribution of GREMLIN restraint scores for Rosetta Ab initio models.....	60
Figure 17. The Zn ²⁺ transport parameters, Km and Vmax, of the H540A mutant.....	63
Figure 18. Relative velocity of WT hZIP4 and mutant transporters	64
Figure 19. Time course of zinc uptake for mutant constructs	66
Figure 20. Competition of ⁶⁵ Zn ²⁺ uptake in H624Q expressing oocytes with a series of divalent cations	68

Figure 21. Contact maps showing contacts made within each cluster, below that are cartoons of the top three models colored blue to red (n to c terminus) for each cluster	71
Figure 22. Models of hZIP4 were generated using Rosetta structure prediction guided by coevolution based contacts, as described in the text.....	72
Figure 23. Variations within cluster A are consistent within context of a dimer.....	74
Figure 24. Structural homology of hZIP4 dimer to other membrane proteins.....	75
Figure 25. Comparison of hZIP4 model and MFS Transporter structure	76
Figure 26. Western blot analysis of tryptophan scanning mutagenesis studies along TM7	77
Figure 27. Comparison of hZIP4 with YIIP	81
Figure 28. The hZIP4 domain structure and predicted regions of disorder	94
Figure 29. Purification of the recombinantly expressed M3M4 domain using the heat-cooling extraction method.....	95
Figure 30. CD spectra of the purified M3M4 domain	96
Figure 31. Normalized competitive binding curves for the determination of Zn ²⁺ dissociation constants to the wild-type, labeled and mutant M3M4 proteins	99
Figure 32. Normalized XANES spectra for wild-type and triple mutant Zn ²⁺ -loaded M3M4 samples.....	104
Figure 33. EXAFS and Fourier transform of the EXAFS data for wild-type and mutant Zn ²⁺ -loaded M3M4 proteins.....	105
Figure 34. Effect of Zn ²⁺ on M3M4 CD spectra.....	108
Figure 35. Proposed model of Zn ²⁺ binding to M3M4	110

List of Tables

Table 1. ZIP protein distribution in human body	9
Table 2. The specificity and selectivity of ZIP proteins	11
Table 3. Reported missense hZIP4 mutations in cancer and <i>AE</i> patients	14
Table 4. Conditions tried to elucidate the driving force for hZIP4 mediated Zn^{2+} transport	26
Table 5. Zinc Transport Kinetic Parameters for WT and mutant hZIP4 transporters.....	65
Table 6. Relative Specificity for Zn^{2+} and Fe^{2+} for WT and mutant hZIP4 transporters	69
Table 7. Zn(II) binding stoichiometry and dissociation constants for M3M4	100
Table 8. EXAFS and Fourier transform of the EXAFS data for wild-type and mutant Zn^{2+} -loaded M3M4 proteins	106

1 INTRODUCTION

1.1 Zinc: An essential micronutrient for humans

Zinc is the second most abundant transition metal found in the living organisms. However, the nutritional value of zinc was first realized in 1869, when the role of zinc was associated with *Aspergillus niger's* growth¹. It took almost another century to extend the importance of zinc to human health. In 1963, zinc was first speculated to have a nutritional value in human health^{2, 3}. Later in 1973, the World Health Organization recommended the inclusion of zinc to the list of essential micronutrients. Since then, there have been extensive studies conducted on zinc deficiency and symptoms in humans. The total zinc found in an adult human is about two grams of zinc and its deficiency can cause growth retardation, weight loss, impaired immune system, hypogonadism, alopecia, diarrhea, neurological abnormalities and delayed wound healing²⁻⁵. Excess of zinc can cause vomiting, diarrhea, muscular cramp and nausea⁶.

1.2 Zinc inside the cell

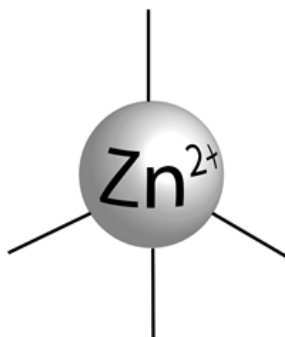
Iron is the most abundant transition metal in the human body followed by zinc and copper. The total cellular concentration of zinc is in the micromolar range⁷. At the cellular level, zinc is associated with gene translation, gene transcription and cell division. Cellular Zn^{2+} deficiency impairs protein synthesis, cell growth and metabolism^{8, 9}. On the other hand, excess of free cellular Zn^{2+} can compete with other transition metal ions and thereby interfere with their function by causing protein-misfolding or aggregation, leading to cellular toxicity¹⁰. Therefore, the concentration of free zinc is tightly regulated inside the cells. Free zinc concentration in eukaryotic cell was found to be in picomolar range^{7, 11}. Excess of zinc is compartmentalized into the storage granules, where zinc concentration can reach up to millimolar concentration¹².

1.3 Zinc biochemical properties

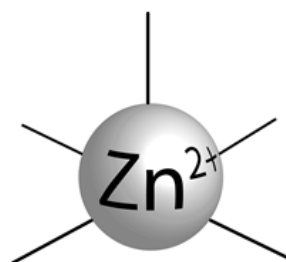
Zinc interacts with many cellular proteins and its functional importance has been associated with but not limited to the structural stability and catalytic activity of proteins. A proteomic study designed to identify Zn²⁺-binding human proteins suggested that about 10% of the human proteome could be Zn²⁺ interacting proteins¹³. More than 300 metalloenzymes, which are essential for cellular metabolic activities have been associated with zinc¹⁴. In fact, zinc is the only transition metal which can interact with all the six classes of enzymes: oxidoreductase, transferase, hydrolase, lyase, isomerase and ligase^{15, 16}. Zinc has a unique electron distribution in the outer most orbital, which allows it to interact with ligands in a multiple coordination geometry arrangement (Figure 1). A detailed study of zinc coordination geometry in proteins shows that zinc prefers a tetrahedral geometry (82%) over trigonal (14%) or octahedral (4%) geometry when zinc is important for the stability of protein structure¹⁷. However, when zinc plays a catalytic role, the relative preference for tetrahedral geometry (58%) decreases whereas the preference for a trigonal (31%) and octahedral geometries (11%) increase¹⁷.

Zinc has very high redox potential, which makes it inert in biological systems. The lack of redox properties separates zinc from other transition metals such as iron and copper, as zinc is less likely to cause oxidative damage *in vivo*¹³. Because of the unique redox properties, zinc can play a protective role against oxidative damage to the cell. For example, the Copper-Zinc superoxide dismutase is the first line of cellular defense mechanism to counter the increase of free radicals^{18, 19}. As a high sulfhydryl interacting metal ion, zinc also protects the antioxidant proteins²⁰. Zinc competes with other redox sensitive metal ions such as iron and copper to displace or reduce their intracellular concentrations²⁰. Zinc provides the structural stability to DNA transcription factors⁸. Furthermore, zinc helps to increase the metallothionein concentration, which scavenges free radicals²¹.

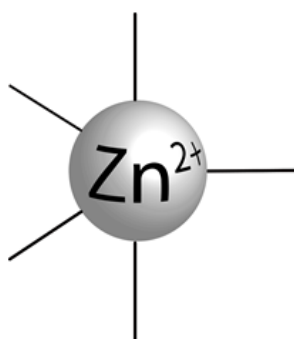
Figure 1. Zn^{2+} coordination geometries



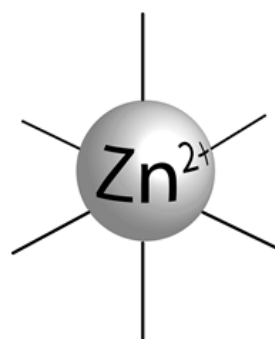
Tetrahedral



Square Pyramidal



Trigonal Bipyramidal



Octahedral

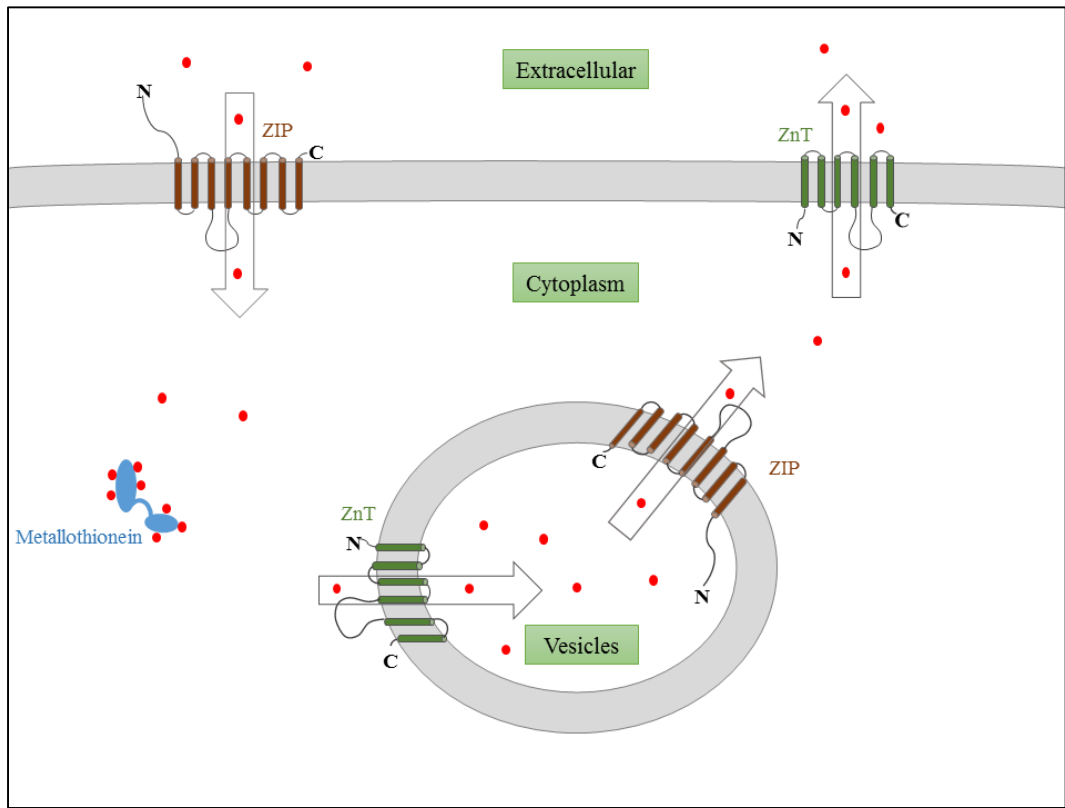
1.4 Proteins important for zinc cellular distribution

Of the total two grams of zinc in an adult human body, only 0.1% zinc is present in the plasma and the rest is stored at the cellular level²². The mechanism of cellular zinc uptake, trafficking and export is a complex field which is largely unexplored²³. Zinc transport was initially hypothesized to be mediated by co-transport with either cysteine or histidine, as zinc binds these amino acid residues with high affinity²⁴. An alternate theory of zinc transport by zinc specific membrane transport proteins was introduced later, which gained more support upon the identification of the first mammalian zinc transporter gene^{25, 26}. Subsequent studies have identified two classes of zinc transporters; those which mediate a net increase (ZIP; Zrt- and Irt-like proteins; SLC39A) or a net decrease (Znt; solute-linked carrier 30; SLC30A) in cytosolic zinc levels (Figure 2)^{23, 27}. Other than zinc transport proteins, metallothionein proteins are important for intracellular zinc trafficking²⁸.

1.4.1. Metallothionein

Metallothionein proteins regulate the zinc trafficking and distribution in the cell whereas zinc transport proteins change the zinc concentration by importing or exporting zinc to the various cellular or extracellular compartments^{21, 28, 29}. The role of metallothionein in physiology has been studied extensively and strong correlations with cellular protective mechanism against oxidative stress was found²⁸. It has also been suggested that the zinc protected thiol groups of metallothionein reacts with oxygen and nitrogen reactive species and in the process releases zinc^{28, 30}. The cells respond to the increased cellular zinc concentration with increased metallothionein concentration as well as a change in the expression of other protective metalloproteins including ZIP and ZnT proteins³¹.

Figure 2. Cellular Zn²⁺ homeostasis



The structural studies of metallothionein protein have suggested that the protein has two domains named α -domain and β -domain³². The α -domain of the metallothionein protein binds to four zinc ions through eleven cysteines, whereas the β -domain coordinates three zinc ions through nine cysteine residues³². The binding affinity of metallothionein proteins to zinc can be up to 10^{-13} M. Further, it has been hypothesized that the α -domain is relevant to zinc transfer across various cellular compartments, while the β -domain has other physiological role such as metal transfer to other metalloproteins.

1.4.2 ZnT proteins

ZnT proteins are grouped under a larger cation diffusion facilitator family of proteins³³. In humans, ZnT family of proteins consist of ten member proteins, which are designated as ZnT1-ZnT10²⁷. The zinc transporter proteins are located in the plasma membrane of various cellular compartments, and they function to reduce the free cytosolic zinc concentration by exporting Zn^{2+} to the extracellular milieu or into the storage vesicles²⁷. Based on hydropathy analysis, it was suggested that ZnT proteins have 6 transmembrane (TM) domains and cytosolic N- and C-termini with the exception of ZnT5³⁴. The ZnT5 protein has a long N-terminus, which has nine transmembrane domains fused together³⁴. The ZnT proteins have a long histidine rich intracellular loop between TM4 and TM5^{35, 36}. It has been suggested that the large intracellular loop acts as a zinc sensing domain and it is important for zinc transport activity³⁴. More recently, elucidation of the crystal structure of the bacterial efflux zinc transporter YiiP which has 25-30% sequence homology with mammalian ZnT zinc transporters has provided important insight into this class of proteins³⁷. The bacterial zinc transporter YiiP functions as a homodimer³⁷. Additionally, an extensive study in MCF-7 cells using bimolecular fluorescence complementation technique revealed that ZnT1, ZnT2, ZnT3, ZnT4, ZnT5 and ZnT7 form homodimers, whereas a heterodimer between ZnT5-ZnT6 was also observed³⁸. Also, an analysis of hZnT4 expression in human breast epithelial cells showed small dimer population under non-reducing denaturing condition³⁹.

ZnT proteins are Zn²⁺/H⁺ exchangers^{40, 41}. Further, based on the study of YiiP protein in proteoliposomes, the stoichiometry analysis suggested that ZnT exchanges proton and zinc in 1:1 ratio⁴⁰. Inspection of the YiiP crystal structure has revealed that D45, D49 of TM2 and H153, D157 of TM5 forms binuclear zinc binding site within the TM region³⁷. Therefore, based on sequence homology it was hypothesized that the YiiP corresponding conserved aspartic acid and/or histidine residues in hZnT of TM2 and TM5 are important for zinc transport. Later, it was also shown that mutation of these residues in mammalian ZnT results in the elimination of Zn²⁺ transport activity⁴¹. Consequently, aspartic acid and histidine residues of TM2 and TM5 are also important for the metal selectivity in ZnT proteins. More recently, ZnT10 has been shown to transport manganese as well⁴². The sequence homology suggested that the conserved histidine position of TM2 is replaced with an aspartic acid residue which may have contributed to the change in metal selectivity of ZnT10⁴².

1.4.3 ZIP proteins

Similar to ZnT proteins, the ZIP proteins are also members of the cation diffusion facilitator family of proteins. However unlike ZnT proteins, ZIP proteins increase the cytosolic zinc concentration by importing zinc from extracellularly or zinc storage vesicles. The ZIP family of proteins has 14 member proteins in humans that are further classified into four major classes based on sequence similarity³⁶. The four subclasses of ZIP family of proteins are ZUPI, ZUPII, *gufA* and LIV-1 (Table 1)³⁶. The subfamily ZUPI consists mainly of plant genes, yeast and protozoan whereas ZUPII subfamily consists of mainly nematodes and mammalian genes⁴³. The *gufA* and LIV-1 subfamilies were introduced later where the *gufA* subfamily is based on sequence similarity with the *gufA* gene in *Myxococcus xanthus* and the LIV-1 subfamily is related to the oestrogen-regulated gene⁴⁴. Amongst all the four subgroups, the LIV-1 group is found only in eukaryotes and is the largest subclass comprising of ZIP4, ZIP5, ZIP6, ZIP7, ZIP8, ZIP10, ZIP12, ZIP13 and ZIP14³⁶.

Table 1. ZIP protein distribution in human body

	ZIP Protein	Tissue Distribution	Cellular Localization
LIV	ZIP4	Small intestine, stomach, colon, kidney, pancreas ⁴⁵	Plasma membrane ⁴⁵
	ZIP12	Brain ⁴⁶	
	ZIP6	Breast, prostate, kidney ⁴⁷	Plasma membrane ⁴⁷
	ZIP8	Pancreas, placenta, lung, liver, testis, thymus ^{48, 49}	Plasma membrane, lysosome, endosomes ⁴⁹
	ZIP14	Liver, heart, pancreas, thyroid gland ⁵⁰	Plasma membrane, mitochondria, endosome, lysosome ^{50, 51}
	ZIP5	Liver, kidney, intestine, pancreas ⁵²	Plasma membrane ⁵²
	ZIP10	Testis, breast ^{53, 54}	
	ZIP7	Brain, prostate, liver ^{53, 55, 56}	Golgi, endoplasmic reticulum ⁵⁶
	ZIP13		Golgi ⁵⁷
	ZIP1	GI tract, liver, heart, spleen, prostate ⁵⁸	Plasma membrane, endoplasmic reticulum ^{58, 59}
	ZIP3	Prostate ⁶⁰	Plasma membrane ⁶⁰
ZIP II	ZIP2	Prostate, uterine ⁶¹	Plasma membrane ⁶¹
	ZIP9	Prostate ⁵³	Golgi ⁶²
ZIP I	ZIP11		
gufA			

The organ distribution of human ZIP proteins is listed in Table 1. Based on hydropathy analysis, ZIP proteins have been predicted to have eight TM domains with both N- and C-terminus are extracellular⁶³. Additionally, ZIP proteins have a large histidine rich intracellular loop between TM3 and TM4 and a highly variable N-terminus. It has been suggested that the histidine rich intracellular domain may act as a zinc sensor. Similar to ZnT, it was predicted that ZIP protein may function as dimer. Later, it was reported that the LIV-1 member protein hZIP13 formed a homodimer⁵⁷. Similarly, dimer hZIP2 was observed when it was over expressed in HEK293 cells⁶⁴. Further, the specificity and selectivity of ZIP proteins varies (Table 2).

ZIP protein mediated Zn^{2+} transport is ATP independent. Multiple attempts have been made to elucidate the driving force for Zn^{2+} transport by ZIP proteins. For example, hZIP1 mediated Zn^{2+} transport was hypothesized to be pH dependent as Zn^{2+} transport is inhibited at lower pH⁶⁵. However, the K_m for Zn^{2+} transport under reduced pH conditions for hZIP1 has not been studied which may help to elucidate more detailed hZIP1 mediated Zn^{2+} transport mechanism. Similarly, hZIP2 mediated Zn^{2+} transport was stimulated by the presence of bicarbonate⁶¹. It was suggested that phosphorylation of some of the residues in hZIP7 drives Zn^{2+} transport⁶⁶. In contrast, hZIP8 and hZIP14 were proposed to be Zn^{2+}/HCO_3^- symporters as bicarbonate transport was inhibited by 4,4'-diisothiocyanatostilbene-2,2'-disulfonic acid (DIDS)⁶⁷. However, the driving force for other ZIP proteins remain unknown.

Table 2. The specificity and selectivity of ZIP proteins

Protein	Heterologous system	Specificity study of Zn ²⁺ transport
hZIP1	K562 Erythroleukemia cells	Zn ²⁺ transport inhibited by six fold Ni ²⁺ ⁵⁹
mZIP1	HEK293 cell	Zn ²⁺ transport was modestly inhibited by 50 fold excess of Cu ²⁺ , Cd ²⁺ , Mn ²⁺ , Co ²⁺ , Ag ¹⁺ , Mg ²⁺ , Ni ²⁺ and Fe ²⁺ ⁶⁸
hZIP2	K562 Erythroleukemia cells	Zn ²⁺ transport inhibited by six fold Cd ²⁺ , Cu ²⁺ and Mn ²⁺ ⁵⁹
mZIP2	HEK293 cell	Zn ²⁺ transport was modestly inhibited by 50 fold excess of Cu ²⁺ , Cd ²⁺ , Mn ²⁺ , Co ²⁺ , Ag ¹⁺ , Mg ²⁺ , Ni ²⁺ and Fe ²⁺ ⁶⁸
mZIP3	HEK293 cell	Zn ²⁺ transport inhibited by tenfold Cu ²⁺ , Cd ²⁺ , Mn ²⁺ , Co ²⁺ , Ag ¹⁺ , Mg ²⁺ and Ni ²⁺ ⁶⁸
mZIP4	HEK293 cell	Zn ²⁺ transport was not inhibited by 50 fold excess of Cu ²⁺ , Cd ²⁺ , Mn ²⁺ , Co ²⁺ , Ag ¹⁺ , Mg ²⁺ , Ni ²⁺ and Fe ²⁺ ⁶⁹
mZIP5	HEK293 cell	Zn ²⁺ transport was not inhibited by 50 fold excess of Cu ²⁺ , Cd ²⁺ , Mn ²⁺ , Co ²⁺ , Ag ¹⁺ , Mg ²⁺ , Ni ²⁺ and Fe ²⁺ ⁵²
mZIP7	Yeast	Transports Zn ²⁺ ⁵⁶
mZIP8	MFF cells	Transports Zn ²⁺ , Cd ²⁺ and Mn ²⁺ ⁷⁰
	<i>X.laevis</i> oocytes	Transports Zn ²⁺ and Cd ²⁺ ⁷¹ Cd ²⁺ transport was inhibited by three fold excess of Hg ²⁺ , 10 fold Cu ²⁺ and 30 fold Pb ²⁺ ⁷¹
rZIP10	LLC-PK ₁ cells	Zn ²⁺ transport was inhibited by Cd ²⁺ ⁷²
mZIP11	MDCK cells	Transports Zn ²⁺ and Cu ²⁺ ⁷³
mZIP12	N2a cells	Transports Zn ²⁺ ⁴⁶
hZIP13	293T cells	Transports Zn ²⁺ ⁵⁷
mZIP14	<i>X.laevis</i> oocytes	Transports Cd ²⁺ , Fe ²⁺ , Mn ²⁺ and Zn ²⁺ ⁷⁴ Fe ²⁺ transport inhibited by 10 fold excess of Cd ²⁺ , Co ²⁺ , Mn ²⁺ , Ni ²⁺ , Pb ²⁺ , or Zn ²⁺ ⁷⁴ Zn ²⁺ transport was inhibited by 10 fold excess of Cd ²⁺ ⁷⁴ Mn ²⁺ was inhibited by 10-fold excess of Cd ²⁺ , Co ²⁺ , Fe ²⁺ , Ni ²⁺ , Pb ²⁺ and Zn ²⁺ ⁷⁴

1.5 hZIP4 protein

The hZIP4 protein is a member of the LIV-1 subfamily and has two major isoforms. Among the two known isomers of the hZIP4 protein, the most abundant isoform has 647-amino acids whereas the second less abundant isoform has 622-amino acids⁷⁵. Similar to other ZIP proteins, hZIP4 has been predicted to have eight transmembrane domains with both N- and C-terminus facing the extracellular side (Figure 3)⁶³. hZIP4 also has a characteristic long histidine rich intracellular loop between TM3 and TM4 (M3M4)^{45, 75}. The highly variable N-terminus amongst ZIP proteins, is predicted to be comprised of 327 amino acids in hZIP4. Similar to the M3M4 domain, the N-terminus of hZIP4 is also rich in histidine and cysteine, which suggests that these residues may have an important role in zinc transport. Further, hZIP4 protein has a highly conserved sequence (HSVFEGGLAVGIQ) in TM4 that is believed to be important for zinc selectivity and transport⁶⁸.

hZIP4, a member of the LIV-1 subfamily, plays an important role in Zn²⁺ homeostasis. hZIP4 was first identified due to its involvement in the lethal, childhood Zn²⁺ deficiency disease *acrodermatitis enteropathica (AE)*⁴⁵. So far, there have been 32 mutations reported in hZIP4 that were responsible for *AE*, of which 13 mutations were missense mutations (Table 3)^{76, 77}. hZIP4 is the primary Zn²⁺ transporter expressed in the stomach, small intestine, colon and kidney^{45, 69}. *AE* is an autosomal recessive genetic disorder whose symptoms include skin lesions, diarrhea, growth retardation, neurological disorders, severe infections and, if left untreated, death⁷⁸. The symptoms of *AE* can be reversed with increased dietary Zn²⁺ supplementation^{78, 79}. In addition to its normal tissue distribution, the surface expression of hZIP4 is increased in pancreatic, liver and brain cancer cells, where hZIP4 surface expression has been correlated with metastatic stage and survival times⁸⁰⁻⁸³. In cancer cells, hZIP4 overexpression was shown to increase the expression of growth factors as well as matrix metalloproteinases, which activates factors implicated in cancer cell proliferation such as the interleukin 6 (IL-6), signaltransducer and activator of transcription 3 (STAT3) pathways⁸⁴. An analysis of the COSMIC human genome database showed 31 missense

Figure 3. Predicted schematic diagram of the human ZIP4 protein. The full-length protein is displayed where histidine residues are shown as orange circles and cysteine residues as blue circles. The first and last residues of the transmembrane domains, as predicted by hydropathy analysis, are shown.

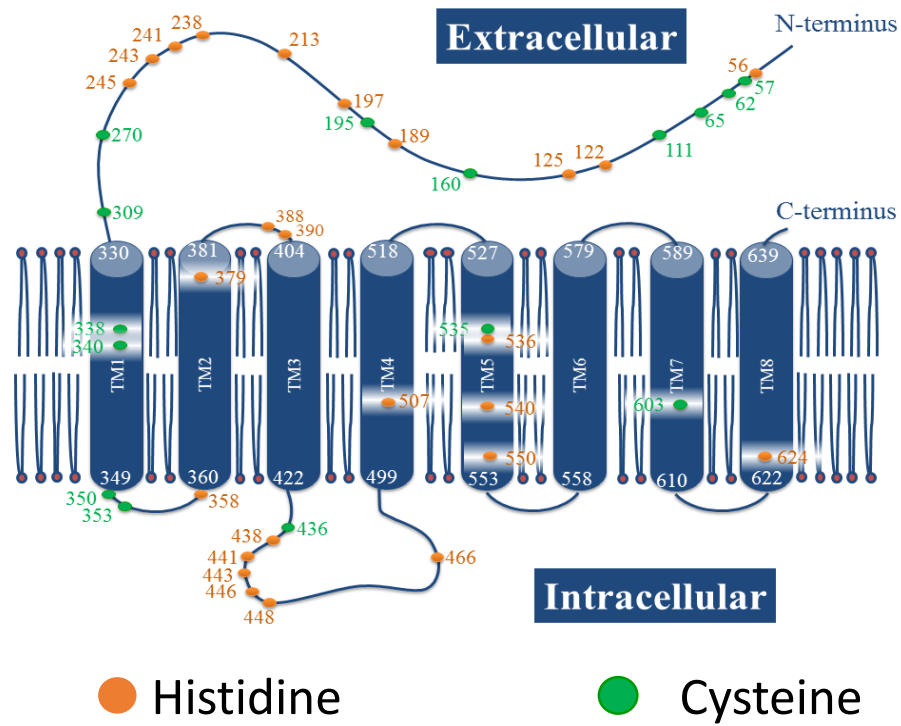


Table 3. Reported missense hZIP4 mutations in cancer and *AE* patients

Location in protein	Mutations reported in cancer patient (COSMIC database)		Mutations reported in <i>Acrodermatitis enteropathica</i> patients	
	Missense mutation	Location	Missense mutation	Impact to protein function
N termini	L28M	Lung	C62R ⁸⁵	
	L32V	Large intestine	R95C ⁸⁶	
	P107L	Skin	N106L ⁴⁵	
	P133L	Skin	P200L ⁷⁵	Reduced V _{max} ⁷⁵
	T268M	Large intestine, pancreas	Q303H ⁸⁶	
	P290L	Haematopoietic and lymphoid	C309Y ⁴⁵	
TM1			G330D ⁴⁵	Cellular mislocalization ⁴⁵
TM2	S366R	Lung	L372P ⁴⁵	Reduced protein expression ⁴⁵
			G374R ⁷⁵	Reduced protein expression ⁷⁵
TM3	F420L	Skin		
TM4	G516C	Large intestine	G512W ⁷⁶	
M4M5			G526R ⁷⁵	Reduced V _{max} ⁷⁵
TM5	F570L	Liver		
	F578T	Liver		
M6M7	S585I	Large intestine		
TM7	L590P	Large intestine	G595V ⁸⁷	
	Y599C	Thyroid		
	D604N	Lung		
	A608T	Pancreas		
M7M8	P617L	Stomach		
TM8	G627A	Endometrium	G630R ⁴⁵	Reduced protein expression ⁴⁵
	L637P	Oesophagus		

substitution mutations to date in N-termini of hZIP4, some of which are listed in Table 3. More recently, it was proposed that ZIP4 mediated Zn^{2+} transport can stimulate glucose dependent insulin secretion in pancreas⁸⁸. Similarly, hZIP6 and hZIP7 have been shown to be important for maintaining insulin level in pancreas⁸⁹.

The most studied ZIP4 protein is derived from mouse (mZIP4). hZIP4 has about 70% sequence homology with mZIP4. The transmembrane domains of hZIP4 and mZIP4 are highly conserved⁶⁹. However, there are some key differences between these two proteins. First, the N-terminal domains of mZIP4 and hZIP4 are only 68% identical and the histidine-rich, putative extracellular zinc binding domain is not conserved. Second, the histidine-rich, putative intracellular zinc binding domain is not conserved between mZIP4 and hZIP4. From a functional standpoint, it has been suggested that mZIP4 is a zinc-selective transporter, because zinc transport is not substantially inhibited by the addition of fifty-fold excess of other transition metals⁶⁹. Also, both mZIP4 and hZIP4 undergo post-translational modifications. Predicted phosphorylation sites for mZIP4 and hZIP4 indicated that mZIP4 undergoes phosphorylation at T367, Y369 and R503 whereas hZIP4 undergoes phosphorylation at T357, Y359 and S490⁹⁰. Earlier it was observed that phosphorylation of another LIV-1 member protein, hZIP7, resulted in hZIP7 mediated Zn^{2+} transport⁹¹. However, a similar study on hZIP4 or mZIP4 has not been conducted and the role of phosphorylation in hZIP4 needs further study.

The N-terminus of hZIP4 is rich in cysteine and histidine residues. Further, the N-terminus has three HxxH and one CxxC motifs, which are similar to conserved zinc binding motifs in zinc finger proteins⁹². Earlier, it was proposed that the N-terminus may have an important role in Zn^{2+} transport because of its ability to increase the local Zn^{2+} concentration. Interestingly, multiple mutations have been reported on the N-terminus of *AE* patients. It has also been suggested that the N-terminus of hZIP4 acts as a Zn^{2+} sensing domain⁹³. However, both the mZIP4 and hZIP4 have been reported to

undergo ectodomain cleavage near its “PALV” signature sequence when cells are starved of Zn^{2+} ⁹³. The “PALV” sequence is believed to be a metalloproteinase cleavage site, and it is highly conserved across the LIV-1 family of proteins. Interestingly, mutations at G340D, G384R, and G643R results in reduced ectodomain cleavage processing; the mechanism of which is not exactly known. Therefore, it is possible that the N-terminus of hZIP4 has other important roles which may or may not be relevant to the Zn^{2+} transport. More recently, the N-terminus of hZIP4 has been suggested to have a prion like structure⁹⁴. It has been predicted that there are at least three potential glycosylation sites on the N-terminus of hZIP4 which are N192, N219 and N272⁹⁵. The detection of hZIP4 in HEK293 cells indicating two distinct hZIP4 populations and treatment of cells with N-Glycosidase F resulted in a singular population of hZIP4 indicating expression of two differently glycosylated hZIP4 protein population⁹⁶. However, the effect of glycosylation on hZIP4 mediated Zn^{2+} transport has not been shown. LIV-1 proteins have also been predicted to have a metalloprotease motif (HEXPHEXGD) located in TM5 suggesting that ZIP proteins may also participate in proteolytic activities²⁷.

Similar to the N-terminal ectodomain of hZIP4, the intracellular characteristic long loop between TM3 and TM4 also has two HxxH motifs. Studies with hZIP4 and its mouse homologue have shown that surface expression of the transporter is regulated by the cytosolic concentration of Zn^{2+} ^{96, 97}. At high cytosolic Zn^{2+} concentrations, ZIP4 undergoes Zn^{2+} -dependent endocytosis, thereby reducing ZIP4 levels in the plasma membrane^{96, 97}. At even higher Zn^{2+} concentrations, hZIP4 is ubiquitinated, presumably at a highly conserved lysine residue within a large intracellular loop between TM3 and TM4 and is further subjected to proteasomal degradation⁹⁶. Earlier, it has been observed that when the cellular concentration of zinc is high, hZIP4 undergoes protein ubiquitination and subsequent degradation. The mutagenesis of all the histidine residues (H438, H441, H443, H446 and H448) within the loop between TM3 and TM4 eliminates hZIP4 ubiquitination⁹⁶. The Zn^{2+} -dependent ubiquitination and degradation required the presence of a

histidine-rich domain located on the large cytosolic loop, leading to the hypothesis that the intracellular domain acts as a Zn^{2+} sensor that is involved in regulating hZIP4 levels in the plasma membrane. Interestingly, the Zn^{2+} sensing intracellular domain also responds to Cd^{2+} by initiating proteolytic degradation of ZIP4 protein but not Cu^{2+} , Mg^{2+} , Ni^{2+} , Co^{2+} and Fe^{2+} ⁹⁶.

2 The Human ZIP4 Transporter Has Two Distinct Binding Affinities and Mediates Transport of Multiple Transition Metals

2.1 Introduction

hZIP4 plays key roles in human zinc homeostasis as well as in the initiation and progression of pancreatic cancer. Also, earlier experiments have suggested that the ZIP family of proteins differ in cation selectivity. Therefore, our objective was to elucidate the cation specificity of hZIP4 uptake. We expressed hZIP4 in *Xenopus laevis* oocytes and developed a radioisotope uptake assay to test the functionality of the protein. We have also investigated which extracellular-accessible residues are important for zinc uptake. The results from these experiments provide a novel insight into the function of hZIP4, while introducing a series of unresolved questions in regards to the mechanism of cation transport.

Lastly, elucidating the function of free or loosely bound Zn^{2+} in the cytosol as well as in intracellular compartments remains important; however, the ability to modulate Zn^{2+} levels *in vivo* in a time-resolved manner remains elusive⁹⁸. Free Zn^{2+} has long been implicated in various signaling pathways⁹⁹, and recently fertilization of oocytes has been shown to trigger “zinc sparks” that serve to initiate meiosis at the beginning stages of embryotic development¹⁰⁰. In this study, we have developed new methodologies to simulate fluctuations in Zn^{2+} concentrations, which facilitates the understanding of complex signaling processes.

2.2 Materials and method

2.2.1 Reagents

The SLC39A4 (hZIP4) gene and the mMessage mMachine SP6 kit were purchased from Invitrogen (Carlsbad, CA). Restriction endonucleases were purchased from New England Biolabs, Inc. (Ipswich, MA). The radioisotopes $^{65}\text{ZnCl}_2$, $^{63}\text{NiCl}_2$, and $^{64}\text{CuCl}_2$, were obtained from Perkin Elmer (Waltham, MA), Oak Ridge National Labs (Oak Ridge, TN) and Washington University of St. Louis (St. Louis, MO), respectively. Maleimide was purchased from Alfa Aesar, Inc (Ward Hill, MA).

2.2.2 Plasmid construct

The hZIP4 gene, containing 647 residues, was subcloned, with a Strep tag (WSHPQPEK) at the C-terminus, into the *Xenopus laevis* oocyte pTLN vector¹⁰¹. Two unique restriction sites *NcoI* at the N-terminus and *BglII* at the C-terminus were used for unidirectional insert incorporation. The entire hZIP4-Strep tag sequence was verified by DNA sequencing.

2.2.3 Preparation of *Xenopus laevis* oocytes for *in situ* expression of hZIP4

Oocytes were surgically removed and isolated from *Xenopus laevis* following a protocol approved by the Worcester Polytechnic Institute Animal Care and Use Committee. Female *Xenopus laevis* were anesthetized with tricaine (1.5 g per liter for 1 hour). Oocytes were extracted by partial ovariectomy and were digested with 2 mg/ml collagenase in ORI buffer (90 mM NaCl, 2 mM KCl, 2 mM CaCl_2 , 5 mM MOPS, pH 7.4) for 4-5 hours at 18° C on an orbital shaker¹⁰². After digestion, oocytes were incubated with Ca^{2+} -free ORI buffer (90 mM NaCl, 2 mM KCl, 5 mM MOPS, pH 7.4) for 10 minutes. Following this step, the oocytes were washed exhaustively; first, with Ca^{2+} -free ORI buffer and second, with ORI buffer. Oocytes were stored at 18° C in ORI buffer with 20 µg/ml gentamycin until needed.

2.2.4 *In vitro* expression of hZIP4

The pTLN plasmid containing the full-length hZIP4 gene with the strep tag was linearized with *Mlu*I and purified using the High Pure PCR Product Purification Kit (Roche Applied Science). mRNA was prepared and purified using the SP6 mMessage mMachine kit according to manufacturer's instructions. Purified mRNA was quantified on a NanoDrop™ ND-2000c Spectrophotometer (Thermo Scientific Co.). A 25 ng aliquot of mRNA in 50 nL DEPC-treated H₂O was injected into each oocyte and was incubated at 18° C in ORI buffer with 20 µg/ml gentamycin for three days prior to measurements. For negative controls, 50 nL DEPC H₂O was injected into oocytes.

2.2.5 Immunofluorescence microscopy

Three days post hZIP4 mRNA injections, oocytes were preincubated with 0 or 10 µM ZnCl₂ for 1 hour in uptake assay buffer, washed and fixed in 4% (w/v) paraformaldehyde solution for 20 minutes at room temperature. DEPC H₂O injected oocytes were used as a negative control. Oocytes were washed with phosphate-buffered saline (PBS) two times and cryoprotected in 30% (w/v) sucrose in PBS overnight at 4° C. The oocytes were frozen in OCT medium (Tissue-Tek) and cut into 25 µm sections. The sections were mounted on positively charged slides (VWR Micro Slides) and blocked in 5% BSA solution in PBS for 1 hour at room temperature. The oocytes sections were washed with PBS two times and incubated with Strep-tactin antibody (IBA GmbH) conjugated with Chromeo-488 dye for 1 hour at 37° C. The sections were washed with PBS two times and then mounted in fluorescence protective mounting medium (KPL Mounting Medium). Fluorescence images were taken using a Leica DM LB-2 microscope with a 20X objective.

2.2.6 Uptake assay

Uptake experiments were loosely based on established protocols¹⁰³. Oocytes, injected with either hZIP4 mRNA or DEPC H₂O, were washed and pre-incubated in 750 µL uptake buffer (90 mM NaCl, 10 mM HEPES and 1 mM ascorbic acid at pH 7.4) for 30 min. The uptake assay was initiated upon addition of radioisotope (⁶³NiCl₂, ⁶⁴CuCl₂, or ⁶⁵ZnCl₂) and was quenched by removal of five to eight oocytes into cold uptake buffer followed by extensive washes. All ⁶⁴CuCl₂ uptake assays were performed in the absence of ascorbic acid. Under these experimental conditions, copper is predominantly in the +2 oxidation state as determined using the copper-bathocuproinedisulfonic acid standard absorbance assay. Each oocyte was solubilized by vigorous vortexing in 1% (w/v) sodium dodecylsulfate (SDS). Total radioactivity was measured using a Beckman LS6500 Multi-Purpose Scintillation Counter with Scintisafe-30% liquid scintillation cocktail (Fisher Scientific). Counts from DEPC H₂O-injected oocytes were subtracted from hZIP4 mRNA-injected oocytes unless otherwise indicated. Counts per minute were converted to picograms (pg) or femtograms (fg) using the following equation:

$$Amount (pg \text{ or } fg) = \frac{CPM \times \text{dilution factor} \times \text{half - life correction factor}}{\text{Specific Activity} \left(\frac{DPM}{pg \text{ or } fg} \right) \times \text{efficiency}}$$

where CPM (counts per minute) were the raw data obtained from each oocyte, dilution factor is the total concentration of radioactive and non-radioactive metal ion divided by the concentration of radioactive cation, half-life correction factor is the half-life of radioisotope divided by the half-life of radioisotope minus time elapsed and the specific activity [in disintegrations per minute (dpm)/pg or fg] as provided by the manufacturer. The half- life for ⁶³Ni⁺², ⁶⁴Cu⁺², and ⁶⁵Zn⁺² are 100 years, 12.7 hours and 244 days, respectively. For a more accurate conversion of cpm to dpm, it was experimentally determined that the efficiency of our scintillation fluid/counter for ⁶³Ni⁺² was 74.3% while the efficiency for ⁶⁴Cu⁺² and ⁶⁵Zn⁺² was 68.4%.

Data was fit to the equation:

$$y = \frac{V_{max} \times [X^{2+}]^n}{K_m^n + [X^{2+}]^n}$$

where V_{max} is the maximal velocity, $[X^{2+}]$ is the concentration of divalent metal ion, K_m is the concentration of divalent metal at one-half V_{max} and n is the Hill co-efficient.

2.2.7 Maleimide and DEPC labeling of hZIP4

Oocytes were pre-incubated for thirty minutes in varying concentrations of either DEPC or maleimide. Prior to initiation of the uptake assay with $3\mu\text{M } ^{65}\text{ZnCl}_2$, half of the oocytes were washed with cold uptake buffer. Reaction initiation, quenching and radioisotope quantification was performed as described earlier (2.2.6). In order to determine whether exposure to DEPC is toxic to the oocytes, the resting membrane potential was determined using a TEC 03X Standard System two electrode voltage clamp set-up (NPI Electronics).

2.2.8 Driving force for hZIP4 mediated $^{65}\text{Zn}^{2+}$ transport

In order to elucidate the driving force for hZIP4 mediated Zn^{2+} transport, the uptake buffer was modified and Zn^{2+} transport was tested as described below.

2.2.8.1 Proton as a driving force

The uptake buffer was prepared with varying pH from 5.5 to 8.5. We observed that oocytes tend to be leaky at a pH lower than 5.5 and higher than 8.5. The uptake assay was performed as described before.

2.2.8.2 Sodium Chloride as a driving force

NMDG was used to test whether sodium contributes to Zn^{2+} transport mediated by hZIP4. The equimolar concentration of sodium chloride was replaced with NMDG. The pH was set to 7.4 using acetic acid and potassium hydroxide.

2.2.8.3 Sodium as a driving force in the presence / absence of chloride

Equimolar concentrations of sodium chloride were replaced with potassium chloride to test the role of sodium in hZIP4 transport activity in the presence of chloride ions. The pH was brought to 7.4 using potassium hydroxide and hydrochloric acid. On the other hand, equimolar concentrations of sodium acetate were replaced with NMDG to test the role of sodium in hZIP4 transport activity in the absence of chloride. The pH was brought to 7.4 using acetic acid and sodium hydroxide.

2.2.8.4 Multiple anion and cation as a driving force

Multiple conditions were tested to define the driving force parameters. The conditions are listed in Table 4. The uptake experiment was performed at pH 7.4.

2.2.9 Zn-Cage compounds and Zn^{2+} transport in *X. laevis* oocytes

$^{65}Zn^{2+}$ (Perkin Elmer) was incubated with a 1000x Zn-Cage compound, nitrilotriacetic acid (NTA) and iminodiacetic acid (IDA) for 15 minutes. The oocytes injected with hZIP4 RNA or DEPC treated water were washed three times with overnight chelex-100 treated uptake buffer and were suspended into the uptake buffer having 250nM final concentration of $^{65}Zn^{2+}$. The oocytes in $^{65}Zn^{2+}$ solution, $^{65}Zn^{2+}$ -NTAde Cage ($^{65}Zn^{2+}$ -NTA decarboxylation photoCage), $^{65}Zn^{2+}$ -NTA and $^{65}Zn^{2+}$ -IDA were irradiated with UV-LED for three minutes followed by 57 minutes incubation at room

temperature in the dark. A batch of oocytes in $^{65}\text{Zn}^{2+}$ -Cage solution was incubated in dark for 60 minutes without irradiation with UV-LED light. After 60 minutes, each oocyte was washed four times with uptake buffer and solubilized in 200 μl of 1 % (w/v) sodium dodecyl sulfate solution. The solubilized oocyte was supplemented with scintillation fluid (Scintisafe-30%, Fisher Scientific) and the radioactivity was measured using a Beckman LS6500 Multi-Purpose Scintillation Counter.

Table 4. Conditions tried to elucidate the driving force for hZIP4 mediated Zn²⁺ transport

	NaCl (mM)	NMDG- Cl (mM)	NaCl : HCO ₃ ⁻ (mM)	NaCl : HCO ₃ ⁻ (mM)	NaGlu (mM)	NaGlu: HCO ₃ ⁻ (mM)	NaGlu: HCO ₃ ⁻ (mM)	NaCit (mM)	KGlu (mM)
Sodium Chloride (NaCl)	90	-	80	70	-	-	-	-	-
NMDG-Cl	-	90	-	-	-	-	-	-	-
Sodium Bicarbonate	-	-	10	20	-	10	20	-	-
Sodium Gluconate (NaGlu)	-	-	-	-	90	80	70	-	-
Sodium Citrate (NaCit)	-	-	-	-	-	-	-	90	-
Potassium Gluconate (KGlu)	-	-	-	-	-	-	-	-	90
HEPES	10	10	10	10	10	10	10	10	10
Ascorbic Acid	1	1	1	1	1	1	1	1	1

2.3 Results

2.3.1 hZIP4 localizes on *Xenopus laevis* oocytes membrane surface

To establish the localization of the heterologously expressed hZIP4 in *Xenopus laevis* oocytes, expression of hZIP4 was detected in sections of paraformaldehyde-fixed oocytes using a Chromeo488-labeled anti-Strep antibody. Immunofluorescence was observed in mRNA injected oocytes before and after exposure to 10 μM ZnCl_2 , but was not visible in DEPC- H_2O injected controls, demonstrating localization at the plasma membrane (Figure 4).

2.3.2 hZIP4 transports zinc in *X. laevis* oocytes

Following insertion of the full-length hZIP4 gene with the strep tag added onto the C-terminus into the pTLN vector and mRNA synthesis, our initial objective was to generate a zinc uptake assay with high specificity and robust signal to noise ratio. The longer, 647 amino acid protein was investigated throughout the course of these experiments as it has been shown that the homologous longer protein is the predominant species in mouse⁶⁹. *Xenopus* oocytes were injected with varying amounts of hZIP4-Strep mRNA and the radioactive $^{65}\text{Zn}^{2+}$ uptake was measured three to six days post-injection. During the course of all assays, DEPC H_2O was injected for negative controls. Optimal radioisotope uptake was observed following injection of 50 ng mRNA of hZIP4 where the assay was initiated three days post-mRNA injection (Figure 5). It was observed during the course of these experiments that injection of a larger amount of hZIP4 mRNA resulted in a decreased viability of oocytes after 3 days of incubation period.

Following optimization of the amount of hZIP4-Strep mRNA to inject in oocytes and identification of the best time to measure radioisotope uptake in mRNA injected oocytes, we were interested in determining the range of zinc which would result in a linear amount of radioisotope uptake over time. Therefore, we initiated the uptake assay using a final concentration of ZnCl_2

Figure 4. Representative images of three oocytes injected with hZIP4 mRNA tagged with Strep tag on the C-terminus and probed with Chromeo488-conjugated anti-Strep antibody. Anti-Strep specific staining is present in oocytes injected with hZIP4 mRNA before (left) and after (right) exposure to 100 μ M ZnCl₂. No staining is observed in DEPC-H₂O injected oocytes (center). The arrow indicates the surface of the oocyte.

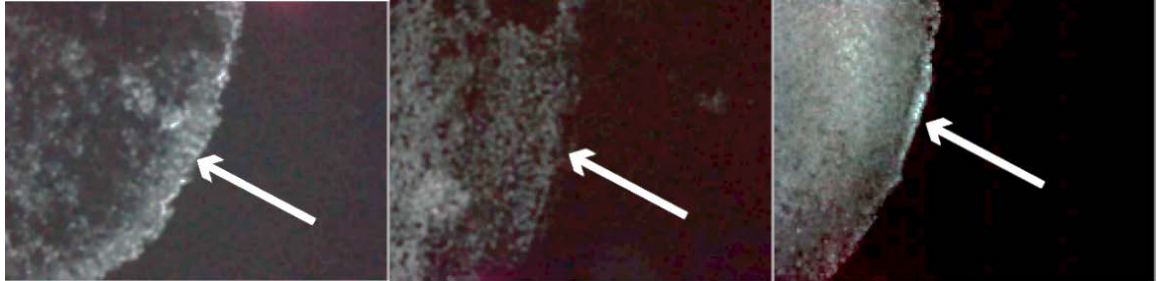
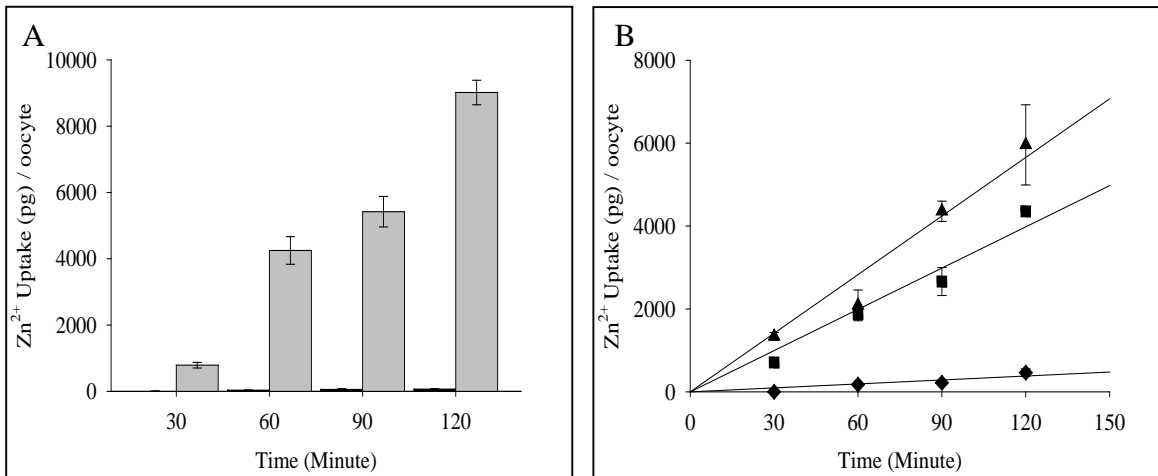


Figure 5. Evaluation of $^{65}\text{Zn}^{2+}$ radioisotope uptake assay in hZIP4 expressing oocytes. (A) Oocytes were injected with either 50 ng of mRNA of hZIP4-Strep in 50 nl of DEPC H₂O or 50 nl of DEPC H₂O. Three days postinjection, $^{65}\text{Zn}^{2+}$ uptake was measured as described in Experimental Procedures over the course of 2 h. Oocytes were removed every 30 min for a total of four time points. A final $^{65}\text{Zn}^{2+}$ concentration of 21.75 μM was used for this experiment. Radioisotope uptake is shown for DEPC H₂O-injected (black) and hZIP4-Strep mRNA-injected (gray) oocytes. Counts per minute were converted to picograms of $^{65}\text{Zn}^{2+}$. Data originated from five to eight oocytes; values are means \pm SEM. (B) Oocytes, injected with 25 ng of hZIP4-Strep mRNA, were incubated with varying amounts of ZnCl_2 [(\blacklozenge) 0.49 μM Zn^{2+} , (\blacksquare) 44.7 μM Zn^{2+} , and (\blacktriangle) 105.1 μM Zn^{2+}]. The assay was quenched every 30 min up to 120 min, and data originated from five to eight oocytes; values are means \pm SEM.



from 0.49-105.1 μM (Figure 5). Analysis of the results from these experiments demonstrated that zinc uptake is roughly linear over two hours over this range of zinc concentration and that zinc uptake is proportional to the amount of Zn^{2+} in the uptake assay.

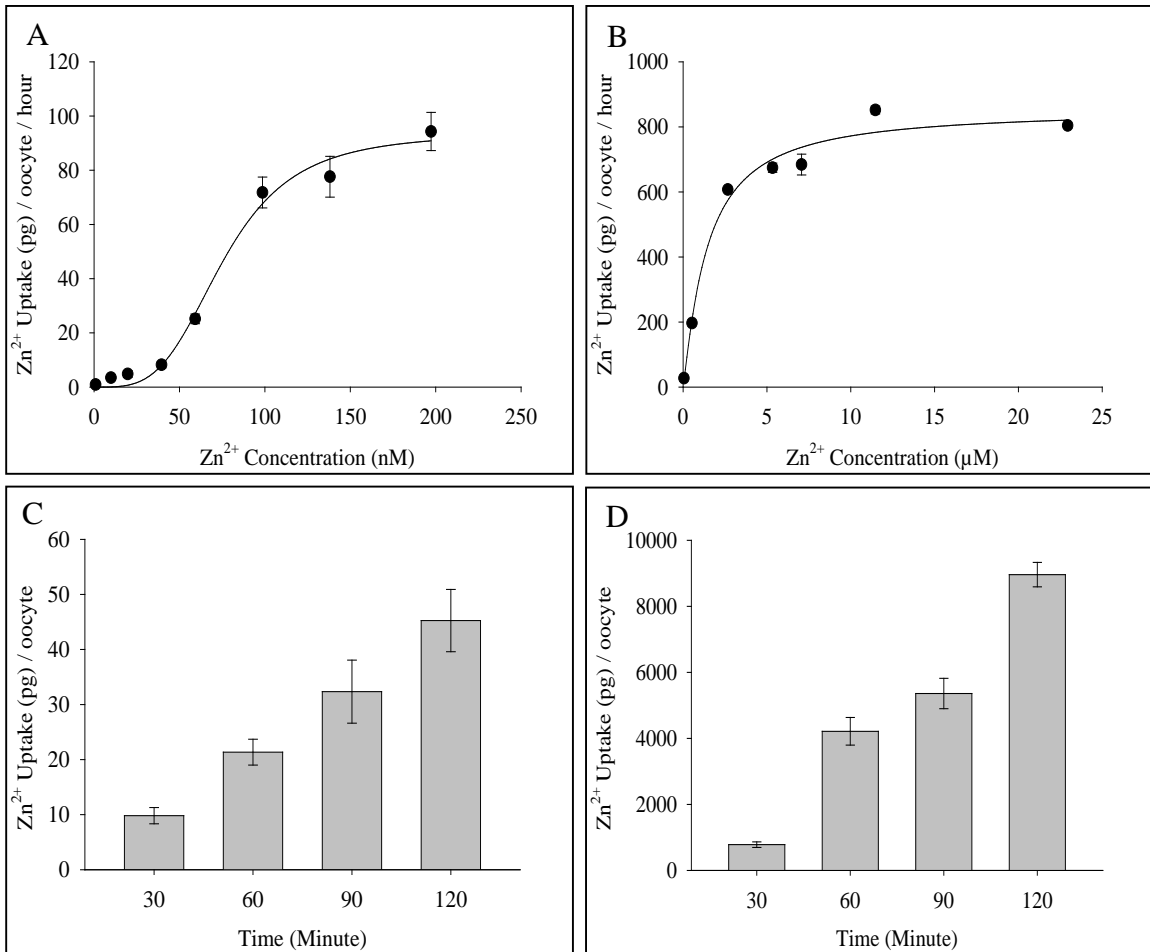
2.3.3 Determination of K_m and V_{\max} for hZIP4-mediated zinc uptake

Our next objective was to determine the K_m for zinc transport by hZIP4. Therefore, we measured Zn^{2+} uptake with varying concentrations of radioisotope in the uptake assay buffer for 60 minutes. Under our experimental conditions, two distinct K_m values for zinc could be elucidated. In both cases, zinc uptake was plotted as a function of the concentration of zinc in the assay buffer (Figure 6A and 6B).

An analysis of the results from our experiments demonstrated that at low zinc concentrations, the K_m was 76 ± 5 nM, where $n = 3.6 \pm 0.6$ and $V_{\max} = 94 \pm 6$ pg/oocyte/hour. A second K_m for zinc was calculated in the micromolar range at 1.4 ± 0.3 μM , where n is 1.2 ± 0.3 and $V_{\max} = 850 \pm 60$ pg/oocyte/hour (Figure 6B). Our results demonstrated that V_{\max} varied for each experiment. This is directly attributable to changes in surface expression of hZIP4 in oocytes. However, the values for K_m and n were consistent over a series of repeated experiments at both micromolar and nanomolar concentrations of zinc. The representative data for measuring transport affinity were conducted on same batch of oocytes.

To elucidate the rate of hZIP4-mediated zinc uptake in the range of both K_m values, zinc uptake was measured as a function of time in the nanomolar and micromolar range (Figure 6C and 6D, 82 nM and 21.75 μM Zn^{2+} , respectively). Under both of these conditions, we observed an approximately linear increase in zinc uptake over the course of the two hour experiment. In addition, the difference in radioactivity when zinc uptake was measured in the nanomolar concentration was at least four times higher in the mRNA injected vs. DEPC H_2O injected oocytes.

Figure 6. Zinc affinity and transport by hZIP4. The transport parameters, K_m and V_{max} , for hZIP4 was elucidated at low (A) and high (B) concentrations of zinc by measuring amount of Zn^{2+} uptake into oocytes injected with hZIP4-Strep mRNA over one hour in assay buffer which contained varying amounts of $ZnCl_2$. At low concentration the K_m and n were calculated to be 76 ± 5 nM and 3.6 ± 0.6 respectively, whereas at high concentration K_m and n were calculated to be 1.4 ± 0.3 μ M and 1.2 ± 0.3 respectively. The rate of Zn^{2+} uptake into oocytes was measured as a function of time at 82 nM (C) and 21.75 μ M (D) over the course of two hours.



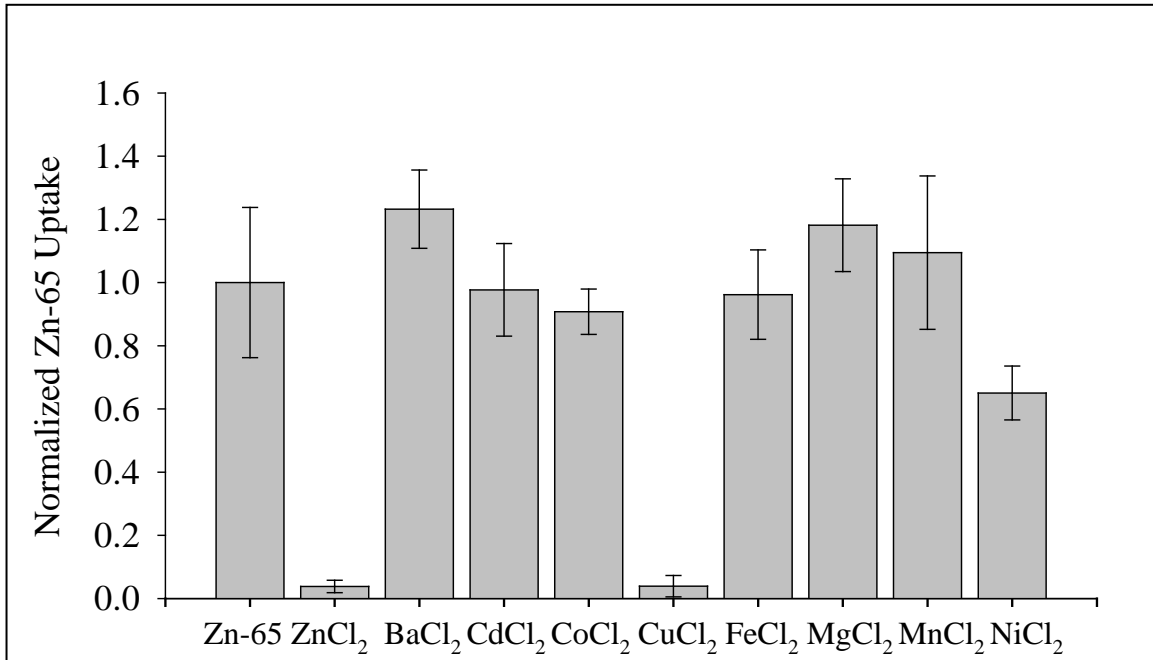
It is noteworthy that the Zn^{2+} transport in hZIP4 injected oocytes varies with different batch of oocytes and mRNA preparation. The time course experiment for Zn^{2+} transport experiment was conducted on different batch of oocytes than the oocytes used for measuring transport affinity.

2.3.4 hZIP4 may transport multiple transition metals

The cation specificity of three of the fourteen human ZIP proteins has been examined^{61, 67, 70}. These proteins have unique transport properties despite the fact that their primary sequences are highly homologous. Therefore, we hypothesized that hZIP4 might transport cations other than zinc. In order to test this hypothesis, our first objective was to determine whether any divalent cations would inhibit hZIP4 mediated $^{65}\text{Zn}^{2+}$ uptake. While this is not a direct measurement of cation transport, this experiment would provide insight into which cations should be tested for hZIP4-mediated cation uptake. For this experiment, oocytes expressing hZIP4 were pre-incubated with 600 μM of various transition metals for one hour. As a positive inhibition control, 600 μM cold Zn^{2+} was pre-incubated with oocytes expressing hZIP4. The zinc uptake assay was initiated upon addition of 3 μM $^{65}\text{Zn}^{2+}$ and the length of time for the uptake assay was one hour. Uptake of $^{65}\text{Zn}^{2+}$ was measured. All of the data was normalized to $^{65}\text{Zn}^{2+}$ uptake in the absence of any competing metal. It was expected that cation(s) which inhibited or competed with zinc uptake would decrease $^{65}\text{Zn}^{2+}$ uptake. In contrast, cations which did not inhibit or compete with hZIP4-mediated $^{65}\text{Zn}^{2+}$ uptake, would demonstrate no change in $^{65}\text{Zn}^{2+}$ uptake.

The results from our experiments demonstrated that addition of 600 μM cold Zn^{2+} inhibited 96 ± 1 % of $^{65}\text{Zn}^{2+}$ uptake (Figure 7). Addition of 600 μM of the divalent cations Ba^{2+} , Cd^{2+} , Co^{2+} , Fe^{2+} , Mg^{2+} , and Mn^{2+} had no significant effect on $^{65}\text{Zn}^{2+}$ uptake. In contrast, addition of 600 μM Cu^{2+} and Ni^{2+} decreased hZIP4-mediated $^{65}\text{Zn}^{2+}$ uptake. The addition of 600 μM Ni^{2+} inhibited 35 ± 8 % of $^{65}\text{Zn}^{2+}$ uptake while the addition of 600 μM Cu^{2+} inhibited 96 ± 1 % of $^{65}\text{Zn}^{2+}$ uptake.

Figure 7. Competition of $^{65}\text{Zn}^{2+}$ uptake with a series of divalent cations in WT hZIP4 expressing oocytes. To determine which divalent cations inhibited hZIP4-mediated $^{65}\text{Zn}^{2+}$ uptake, oocytes expressing hZIP4 were pre-incubated in 600 μM cold ZnCl_2 , BaCl_2 , CdCl_2 , CoCl_2 , CuCl_2 , FeCl_2 , MgCl_2 , MnCl_2 , or NiCl_2 in the uptake assay buffer. The uptake assay was initiated by adding 3.0 μM $^{65}\text{ZnCl}_2$.



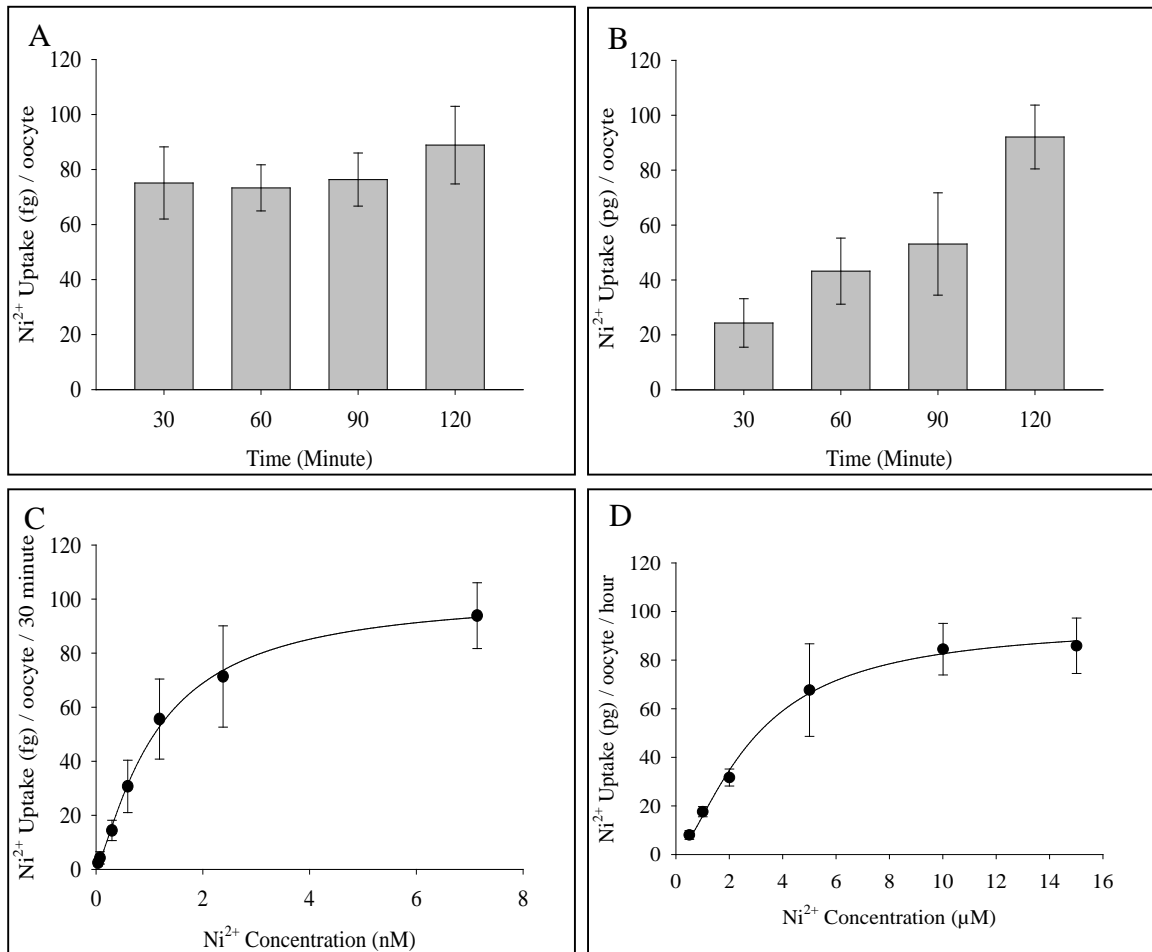
It is noteworthy that ascorbic acid was absent in Zn^{2+} transport assay when Cu^{2+} was used as a competing divalent metal. The uptake assay in the presence of Cu^{2+} and ascorbic acid resulted in non-viable and leaky oocytes. The presence of ascorbic acid reduces Cu^{2+} to Cu^{1+} . Our colorimetric assay measuring the amount of Cu^{1+} generated from an excess of Cu^{2+} (600 mM) in the presence of 1 mM ascorbic acid and 1 mM copper-bathocuproinedisulfonic acid confirmed that ascorbic acid undergoes oxidation to generate almost 1 mM of Cu^{1+} . The Cu^{1+} generated in the presence of ascorbic acid damages the oocyte membrane possibly by lipid peroxidation reaction.

2.3.5 hZIP4 can transport nickel

Considering that our competition experiment does not directly test for cation uptake other than zinc, our next objective was to directly measure whether Cu^{2+} or Ni^{2+} could be transported by hZIP4. Therefore, $^{63}\text{Ni}^{2+}$ uptake was measured using our established uptake assay except that $^{65}\text{Zn}^{2+}$ was replaced with $^{63}\text{Ni}^{2+}$.

As a first step, we examined whether nickel uptake was linear over time. At low concentrations (4.76 nM $^{63}\text{Ni}^{2+}$), there is a measurable amount of nickel which accumulates with the hZIP4-injected oocytes which does not increase over the two hour uptake assay (Figure 8A). In contrast, when the concentration of Ni^{2+} is increased in the uptake assay (5.25 μM), nickel uptake is approximately linear over two hours (Figure 8B). After obtaining these results, our next experiments were performed with the goal to determine the K_m of Ni^{2+} at both nanomolar and micromolar concentrations. When our uptake assay contained low amounts of $^{63}\text{Ni}^{2+}$, an analysis of our experiments determined that nickel uptake follows Michaelis-Menten kinetics, where the K_m is 1.1 ± 0.1 nM and $n = 1.3 \pm 0.1$ where V_{\max} is 102 ± 4 fg/oocyte/hour (Figure 8C). At the micromolar range of Ni^{2+} , an analysis of our experiments revealed that the K_m is 2.9 ± 0.3 μM and $n = 1.5 \pm 0.2$ where V_{\max} is 95 ± 5 pg/oocyte/hour (Figure 8D). In addition, the difference in

Figure 8. Nickel affinity and transport by hZIP4. A. $^{63}\text{Ni}^{2+}$ uptake for oocytes injected with either 25 ng mRNA of hZIP4-Strep in 50 nL DEPC H₂O or 50 nL DEPC H₂O was measured as described in the Materials and Methods section over the course of two hours using a final concentration of 4.76 nM $^{63}\text{NiCl}_2$. B. In a similar manner, Ni^{2+} uptake was measured using a final concentration of 5.25 μM NiCl_2 . C. The K_m and V_{\max} of $^{63}\text{Ni}^{2+}$ was elucidated at nanomolar concentrations of $^{63}\text{Ni}^{2+}$. The K_m and n were calculated to be 1.1 ± 0.1 nM and 1.3 ± 0.1 respectively. D. The K_m and V_{\max} of Ni^{2+} was elucidated at micromolar concentrations of Ni^{2+} . The K_m and n were calculated to be 2.9 ± 0.3 μM and 1.5 ± 0.2 respectively.



radioactivity when the nickel uptake was measured in the nanomolar concentration was at least four times higher in the mRNA injected vs. DEPC H₂O injected oocytes.

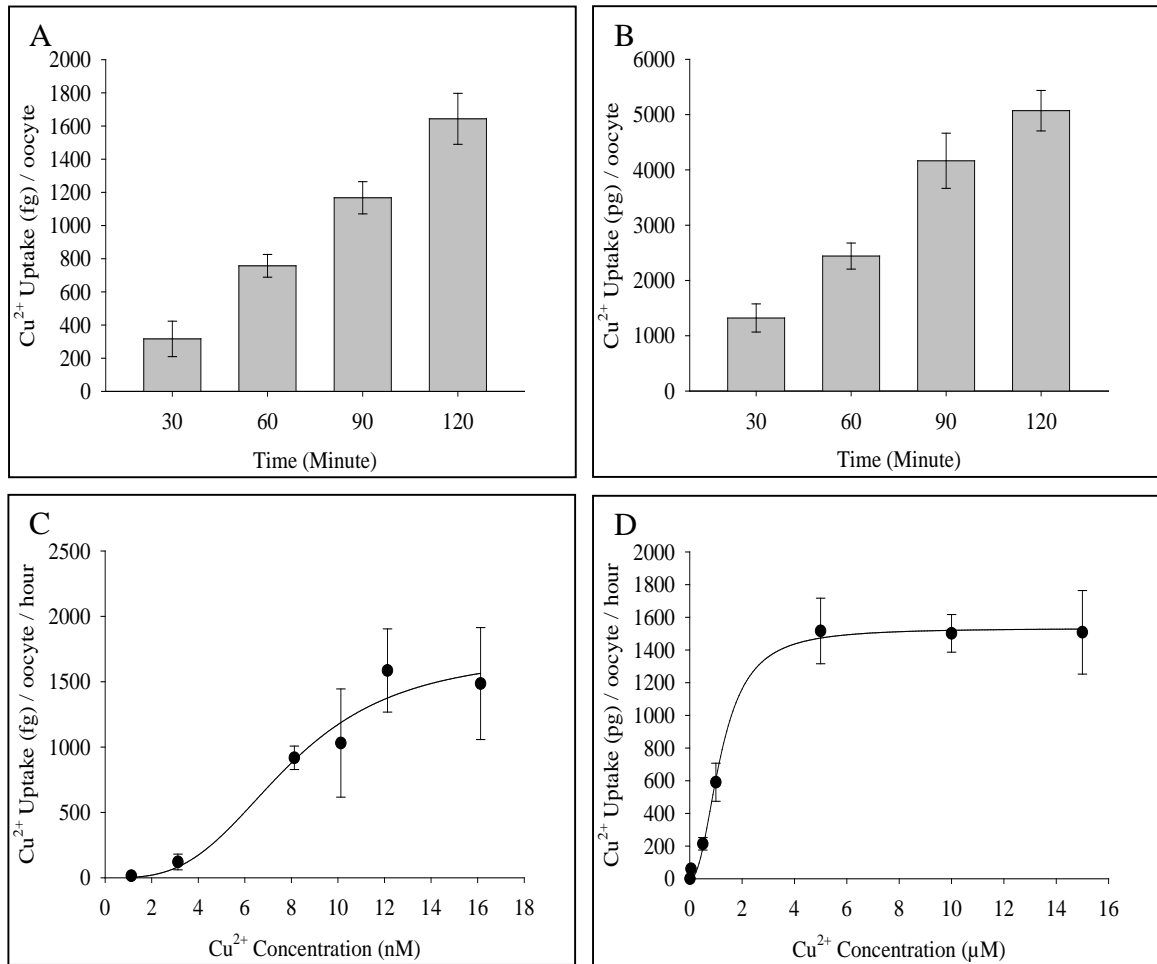
2.3.6 hZIP4 transports copper (II) in oocytes

Considering our experimental result that a 200-fold excess of Cu²⁺ inhibits more than 95% of ⁶⁵Zn²⁺ uptake, our goal was to directly examine Cu²⁺ uptake. In a similar manner as the previous experiments, the first step for these experiments was to measure the rate of Cu²⁺ uptake at low (6.6 nM) and high (10 μM) concentrations (Figures 9A and 9B). Under each of these conditions, the amount of Cu²⁺ uptake increased at an approximately linear rate during the two hour experiment. Therefore, our next experiment was to calculate the K_m for Cu²⁺ uptake. Similar to both zinc and nickel, we could elucidate two distinct K_m values for copper uptake when the uptake was plotted as a function of Cu²⁺ concentration. Furthermore, the difference in radioactivity when copper (II) uptake was measured for a nanomolar concentration was at least four times higher in the mRNA injected vs. DEPC H₂O injected oocytes. We were able to calculate a K_m of 7.9 ± 1.3 nM where n = 3.2 ± 1.9 and V_{max} is 1721 ± 373 fg/oocyte/hour when Cu²⁺ was added to the uptake assay in nanomolar amounts (Figure 9C). Using a higher concentration of Cu²⁺, the K_m was calculated to be 1.20 ± 0.09 μM where n = 2.2 ± 0.3 V_{max} is 1530 ± 30 pg/oocyte/hour (Figure 9D).

2.3.7 Extracellular histidine residues are important for hZIP4 mediated ⁶⁵Zn²⁺ transport

It was initially hypothesized that zinc transport into cells was mediated by co-transport with either histidine or cysteine residues as zinc binds with high affinity to these residues. This theory became mutually unexclusive when the first mammalian zinc transporter gene was identified in 1995¹⁰⁴. Based on this initial hypothesis and the fact that zinc coordinates tightly to both cysteine and histidine, we hypothesized that covalent labeling of extracellular-accessible cysteine and/or histidine residues would disrupt ⁶⁵Zn²⁺ uptake.

Figure 9. Time course and kinetics of hZIP4-mediated Cu^{2+} uptake. A. Cu^{2+} uptake was measured over two hours at a final concentration of 6.6 nM in femtograms. B. Cu^{2+} uptake was measured at a final concentration of 10 μM over two hours in picograms. C. Cu^{2+} uptake was measured after one hour at varying concentrations of Cu^{2+} to quantify the transport properties of this cation. The K_m and n were determined to be 7.9 ± 1.3 nM and 3.22 ± 1.9 respectively. D. $^{64}\text{Cu}^{2+}$ uptake was measured after one hour at micromolar concentrations of $^{64}\text{Cu}^{2+}$ to quantify the transport properties. At these concentrations, the K_m and n were calculated to be 1.2 ± 0.1 μM and 2.2 ± 0.3 respectively.

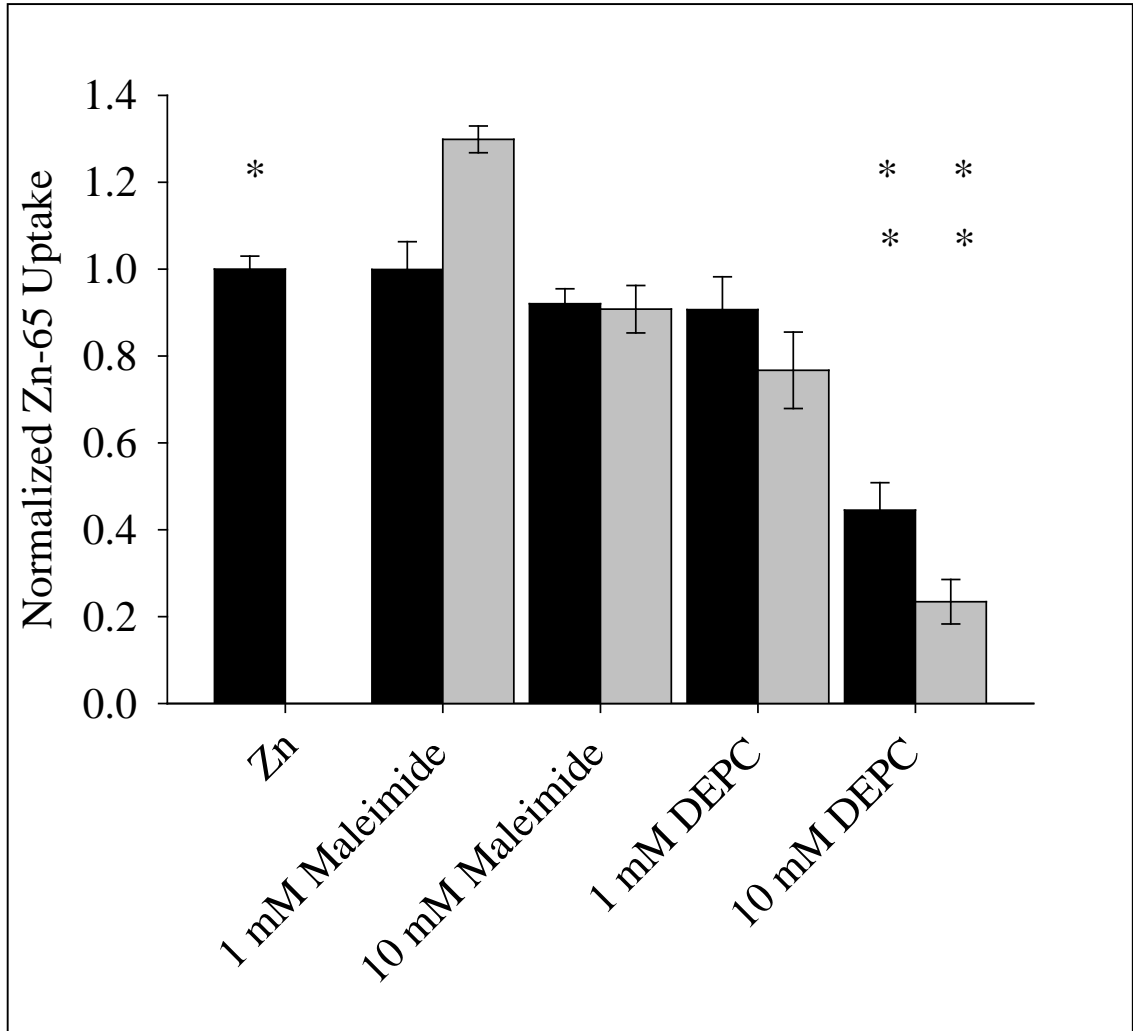


Maleimide and DEPC have been used previously to examine the role of extracellular-accessible cysteine and histidine residues, respectively, following heterologous expression in *Xenopus laevis* oocytes^{105, 106}. Oocytes, injected with either hZIP4 mRNA or DEPC H₂O, were pre-incubated with maleimide and DEPC H₂O for 30 minutes. The oocytes were then washed exhaustively with uptake assay buffer and the uptake assay was initiated upon addition of ⁶⁵Zn²⁺. Under these experimental conditions, no free maleimide or DEPC is present in the uptake assay. No change in zinc uptake was observed following labeling with 1 mM or 10 mM maleimide (Figure 10). In contrast, while no change was observed in ⁶⁵Zn²⁺ uptake with 1 mM DEPC, a significant decrease of zinc uptake was observed following labeling of oocytes expressing hZIP4 with 10 mM DEPC.

In order to further explore the relationship between zinc uptake and labeling of free cysteine and histidine residues, maleimide and DEPC were not washed out prior to the uptake assay. Therefore, maleimide or DEPC is available to react with residues in hZIP4 which may move from an inaccessible to accessible state during the conformational change of hZIP4 which is correlated with zinc transport.

Under these conditions, there was an increase in zinc uptake when 1 mM maleimide was present in the uptake assay during zinc transport. This increase in zinc uptake in the presence of maleimide was abolished when the concentration of maleimide was increased to 10 mM. No significant change in zinc uptake was observed when 1 mM DEPC was present in the uptake assay. In contrast, there was a significant decrease in zinc uptake when 10 mM DEPC was included in the uptake assay when compared to having the 10 mM DEPC washed out prior to the radioisotope uptake assay. In order to assess whether the addition of 10 mM DEPC had a toxic effect on oocytes, the resting membrane potential of oocytes pre-incubated in 0 or 10 mM DEPC for 60 minutes was determined using a two-electrode voltage clamp set-up. No significant difference in membrane potential was observed between these two experimental conditions. It has already been

Figure 10. Extracellular histidines are involved in zinc translocation. The uptake data for DEPC or Maleimide treated hZIP4 expressing oocytes was normalized to non-treated oocytes. Black bars represent zinc uptake after labeling reagents were removed prior to uptake assay. Grey bars are the results when the labeling reagents were present during the uptake assay. At least one asterisk indicates that there is a statistically significant difference in uptake values between the experimental and control experiments by t test. Two asterisks indicate a statistically significant difference (ANOVA p value <0.05) in uptake values between two experimental conditions.



demonstrated that exposure of 10 mM DEPC to oocytes overnight has no effect on the resting membrane potential of oocytes¹⁰⁷.

2.3.8 Multiple factors were tested to define the driving force for hZIP4 mediated $^{65}\text{Zn}^{2+}$ transport

In order to elucidate the driving force of hZIP4 mediated zinc transport, we performed a series of pH and ion replacement experiments. Analysis of the results show that hZIP4 activity is pH independent (Figure 11A). Our ion replacement assay shows that zinc transport is inversely proportional to sodium chloride and sodium acetate concentration (Figure 11B, 11C). In the event of replacing sodium chloride with potassium chloride, the uptake experiment results were inconclusive (Figure 11D). Replacement of sodium chloride with sodium gluconate or potassium gluconate was also inconclusive. Finally, replacement with sodium citrate significantly reduces the hZIP4 mediated transport (Figure 12). It is also noteworthy, that equimolar replacement of sodium chloride with sodium citrate makes the intracellular pH acidic. This is also true with sodium acetate. With the possible effect on intracellular pH for sodium citrate and sodium acetate, we can't rule out the possibility of change in uptake conditions are actually due to the change in ion gradient and not because of change in intracellular pH.

2.3.9 hZIP4 expressing *X.laevis* oocytes can be used for Zn^{2+} photocage compound in evaluating their application in biological system

The feasibility of using photocaged Zn^{2+} in biological systems was demonstrated by measuring Zn^{2+} transport following the heterologous expression of the human zinc transporter ZIP4 in *X. laevis* oocytes. In this experiment (Figure 13), we incubated oocytes expressing hZIP4 or water-injected controls with 250 nM $^{65}\text{ZnCl}_2$, $^{65}\text{Zn}(\text{NTAdeCage})^{1-}$ in the absence of light, $^{65}\text{Zn}(\text{NTAdeCage})^{1-}$ exposed to light, $^{65}\text{Zn}(\text{NTA})^{1-}$ exposed to light or $^{65}\text{Zn}(\text{IDA})^{1-}$ exposed to light. Future

Figure 11. Effect of pH, salt concentration on hZIP4 mediated Zn^{2+} transport. The uptake assay was carried out with $3\mu M$ Zn concentration for 1 hour. A) Oocytes were incubated in uptake buffer with varying pH from 5.5 to 8.5. B) Oocytes were incubated with varying sodium chloride concentration. Sodium Chloride was replaced with equimolar concentration of NMDG, C) Oocytes were incubated with varying concentration of sodium acetate. Equimolar concentration of sodium acetate was replaced with NMDG. D) To test the possibility of sodium being driving force NaCl was replaced with equimolar concentration of Potassium Chloride.

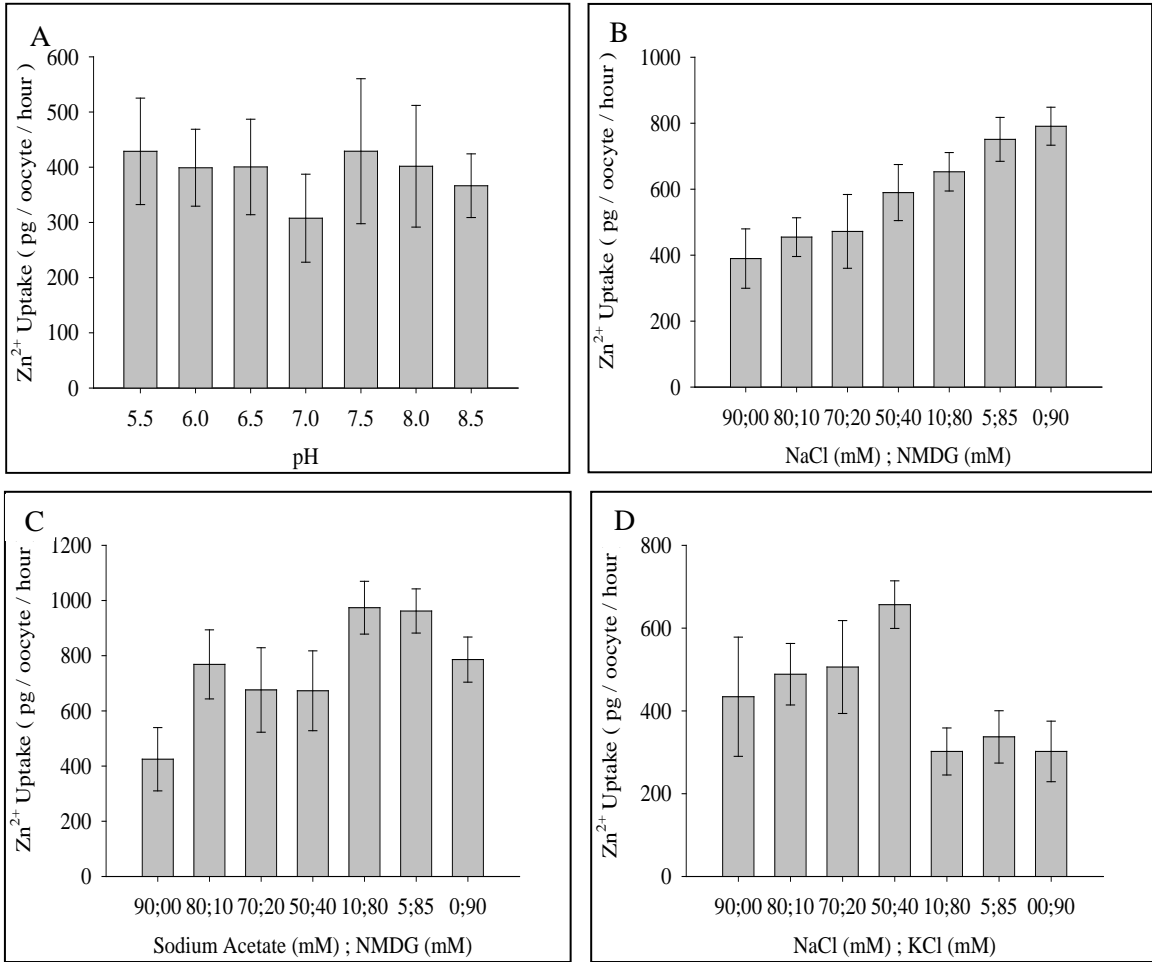


Figure 12. Effect of different buffers on hZIP4 mediated Zn^{2+} transport. The uptake assay was carried out with $6\mu M$ Zn concentration for 1 hour. Oocytes were incubated in uptake buffer with varying conditions at pH 7.4.

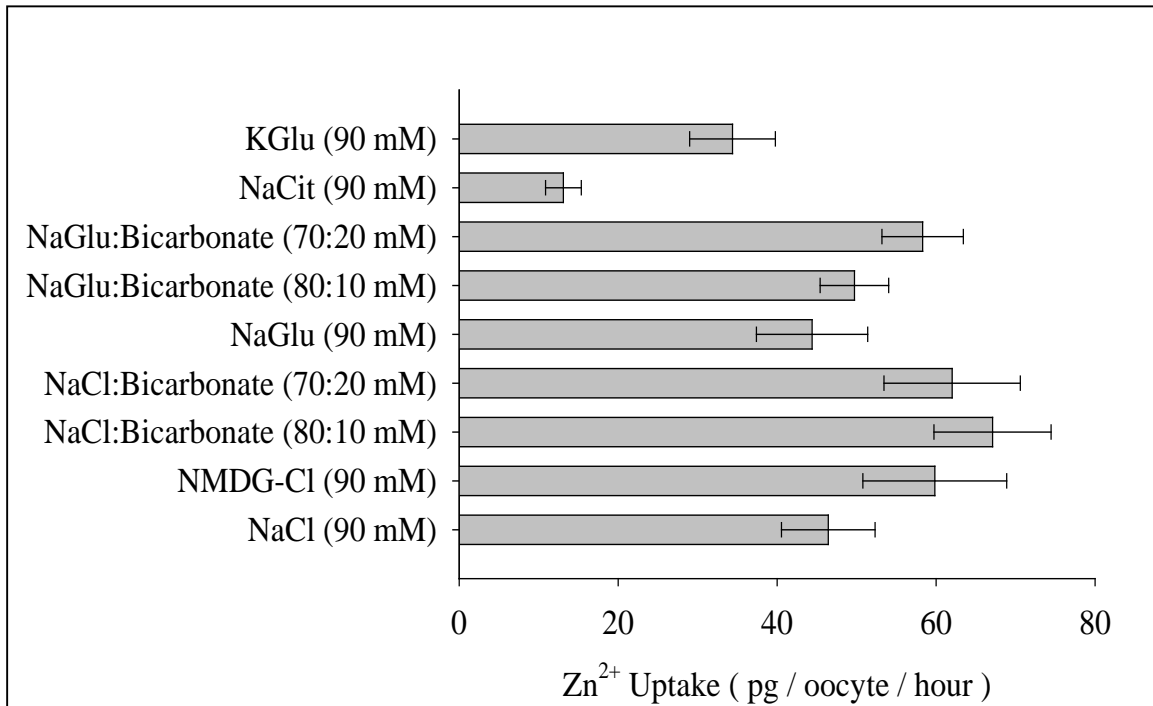
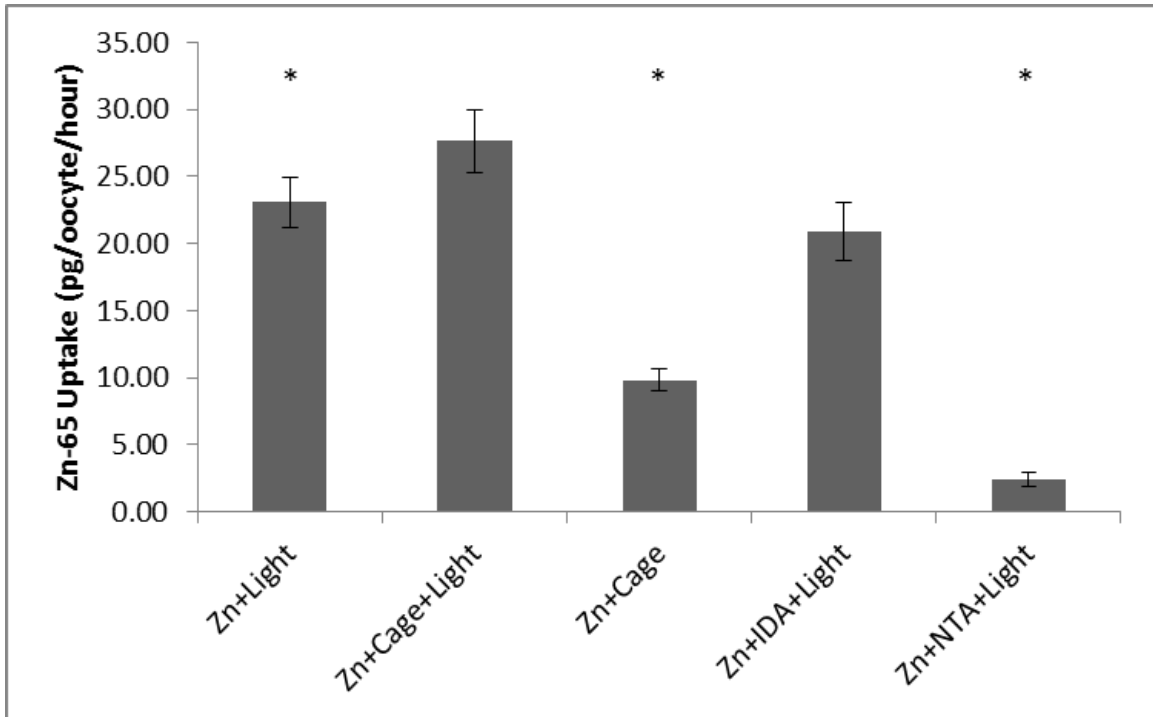


Figure 13. Evaluation of hZIP4 expressing oocytes as a model system to test photocaged Zn^{2+} in biological system. Oocytes were subjected to $^{65}Zn^{2+}$ by incubating them with 250 nM $^{65}ZnCl_2$ or 250 nM $^{65}ZnCl_2$ in the presence of 250 μ M of NTAdCage, NTA or IDA. The assay was performed as described previously. Each bar represents the data from the analysis of 9 to 12 oocytes. The uptake values shown are the mean values with standard error



experiments will address the kinetics of metal ion release from $[\text{Zn}(\text{NTAdeCage})]^{1-}$ since the rate of uptake in this assay depends both on the uncaging kinetics and the kinetics of the transport protein. For these experiments, water-injected oocytes were subtracted from mRNA injected oocytes. Under these experimental conditions, free $^{65}\text{Zn}^{2+}$, uncaged $^{65}\text{Zn}^{2+}$ (by light) or $^{65}\text{Zn}^{2+}$ in the presence of the photocage product (IDA) had transport rates which were similar. In contrast, $^{65}\text{Zn}^{2+}$ coordinated to NTA or $^{65}\text{Zn}^{2+}$ coordinated to the photocaged complex in the absence of light were transported by hZIP4 at a lower rate. The results suggest that both tetradentate chelators bind $^{65}\text{Zn}^{2+}$ tightly, which inhibits transport by hZIP4. Upon photolysis of $[\text{Zn}(\text{NTAdeCage})]^{1-}$, $^{65}\text{Zn}^{2+}$ becomes available for uptake by the oocytes.

2.4 Discussion

To investigate the specificity and kinetic parameters of hZIP4, we used *Xenopus laevis* oocytes as a platform to express this protein. While oocytes do have an endogenous zinc efflux mechanism, it has previously been shown that zinc efflux is independent of the extracellular zinc concentration which may contribute to our experimentally determined kinetic parameters¹⁰³. We have directly demonstrated that hZIP4 can transport Zn²⁺. Furthermore, Cu²⁺ and Ni²⁺ inhibit hZIP4-mediated zinc uptake when these cations are present in 200 fold excess amounts. In contrast, the divalent cations Ba²⁺, Cd²⁺, Co²⁺, Fe²⁺, Mg²⁺, and Mn²⁺ had no significant effect on ⁶⁵Zn²⁺ uptake. While this data is inconsistent with previous data which suggested that the mZIP4 protein is a Zn²⁺ cation transporter, it has been recently suggested that the ZIP family of proteins may have broader substrate translocation capability since hZIP14 can transport a variety of divalent cations^{69, 74}. Furthermore, it is important to note that from our experiments we can only conclude that Ba²⁺, Cd²⁺, Co²⁺, Fe²⁺, Mg²⁺, and Mn²⁺ do not inhibit hZIP4-mediated ⁶⁵Zn²⁺ uptake. We cannot make any conclusions on whether these cations can be transported by hZIP4. It has been shown that Fe²⁺ does not inhibit hZIP14-mediated ¹⁰⁹Cd²⁺ uptake, but that Fe²⁺ can be transported by hZIP14⁷⁴. Therefore, it is possible that hZIP4 could mediate the transport of one or more of the above named cations which do not inhibit ⁶⁵Zn²⁺ transport. For example, if there is more than one mechanism for cation translocation which do not compete with each other, we would expect similar results as in Figure 7 for the cations which do not inhibit ⁶⁵Zn²⁺ uptake. Alternatively, if the rate of transport for one of these cations is sufficiently fast, that it would not inhibit ⁶⁵Zn²⁺ uptake, we would also observe no change in ⁶⁵Zn²⁺ uptake upon addition of this cation in our cation competition experiment. Our subsequent experiments have demonstrated that both Cu²⁺ and Ni²⁺ can be transported by hZIP4 when these cations are present in micromolar quantities. The apparent affinities for each of these cations are in the low micromolar range.

A careful analysis of our experimental results has also uncovered a second binding affinity for $^{65}\text{Zn}^{2+}$, $^{63}\text{Ni}^{2+}$, and $^{64}\text{Cu}^{2+}$. At this concentration, $^{65}\text{Zn}^{2+}$ and $^{64}\text{Cu}^{2+}$ are transported by hZIP4 as shown by the increase in radioisotope uptake over time. In contrast, $^{63}\text{Ni}^{2+}$ has a nanomolar binding affinity, but does not appear to be transported as there is no increase in radioisotope uptake over time. Combined, this data suggests that there are at least two distinct coordination sites within hZIP4. The simplest explanation is that the high affinity for each cation is for one site while the low affinity value is for a second cation coordinating site. However, our data cannot directly resolve whether this is the case. More importantly, a variety of groups have determined that the free concentration of zinc in cells is somewhere between 5 pM and 1 nM, while the free zinc concentration in plasma is estimated to be between ~0.1-1 nM^{108, 109}. Therefore, considering the high affinity site, this could have physiological relevance. This is an unresolved question which would require further experiments both *in vivo* and *in vitro*. Alternatively, it could be possible that our observed increase in radioactivity over time at low concentrations of Cu^{2+} and Zn^{2+} is due to a long time course of cation binding to hZIP4. We consider this unlikely as this would likely be observed in our nickel uptake assay in the nanomolar concentration range. Therefore, based on our experimental results, it appears that zinc and Cu^{2+} can be transported at low concentrations, while the coordination of Ni^{2+} does not result in transport, hence there is no increase in Ni^{2+} uptake over time (Figure 8A).

It is interesting to further examine the observation that low concentrations of $^{63}\text{Ni}^{2+}$ bind but are not transported by hZIP4. In contrast to either Zn^{2+} or Cu^{2+} , there is no cooperativity for Ni^{2+} in the nanomolar range. We propose that there is a coordination geometry where the binding of nickel does not lead to translocation, but where both copper and zinc can be released for transport. Ni^{2+} prefers an octahedral coordination geometry while Zn^{2+} and Cu^{2+} prefer tetrahedral and tetragonal coordination geometries, respectively¹¹⁰. Perhaps the transport of Ni^{2+} in the nanomolar concentration range is blocked due to differences in coordination geometry¹¹⁰.

It is important to note that an analysis of our data cannot exclude other possibilities. One possibility is that nickel coordinates to a regulatory site and not a putative transport site as this would result in no nickel transport. Alternatively, the nanomolar affinity site might require a conformational change for subsequent cation translocation. If both Cu^{2+} and Zn^{2+} coordination induces a sufficient conformational change to promote translocation, whereas coordination of nickel does not induce a sufficient conformational change for cation translocation, a similar experimental result would be observed.

Finally, considering that zinc was originally hypothesized to be co-transported by histidine or cysteine residues, our objective during the course of our next set of experiments was to determine whether covalent labeling of either of these residues would inhibit $^{65}\text{Zn}^{2+}$ uptake. Our data suggests that freely accessible cysteine residues, which are on the extracellular side of the membrane are not a rate-limiting step in $^{65}\text{Zn}^{2+}$ uptake as transport is not inhibited upon addition of high concentrations of maleimide (Figure 10). In contrast, addition of DEPC prior to the uptake assay has a significant effect on $^{65}\text{Zn}^{2+}$ uptake. This suggests that histidine residues on the extracellular side of the protein contribute to zinc transport across the plasma membrane. It is important to note here that DEPC may also label histidine residues which are water accessible, but are located within the transmembrane domains. When DEPC is incubated with hZIP4-injected oocytes, both before and during the uptake assay when compared to washing out DEPC prior to the uptake assay, there is an added decrease in zinc uptake. We speculate that this added decrease in zinc uptake is due to a conformational change of hZIP4 which exposes one or more previously inaccessible histidine residues for labeling. Alternatively, labeling of histidine residues may “lock” hZIP4 in a conformation where further zinc uptake is not possible. A hydropathy analysis of the hZIP4 gene sequence shows that there are seven extracellular histidine residues, while the transmembrane domains encode an additional four histidine residues (Figure 3). Although, DEPC mostly modifies histidine residues, it is possible that it can also label lysine, tyrosine, cysteine, arginine, serine and

threonine residues¹¹¹. DEPC labeling of one or more of these residues contribute to the decline in zinc uptake in our experimental conditions.

It is worthwhile to use the results from these experiments to speculate on the mechanism of cation selectivity of hZIP4. The ionic radii of Ni²⁺, Cu²⁺, and Zn²⁺ are 83, 87 and 88 pm, respectively. Each of the other cations tested are either smaller (Fe²⁺: 75 pm, Co²⁺: 79 pm, Mn²⁺: 81 pm) or larger (Cd²⁺: 109 pm, Ba²⁺: 149 pm) than the three cations which are transported by hZIP4 with the notable exception of Mg²⁺ (86 pm). However, whereas the preferred donor atom for Mg²⁺ is oxygen, the preferred donor atoms for Ni²⁺, Cu²⁺, and Zn²⁺ are either sulfur or nitrogen. Our covalent modification experiments with DEPC support our proposal that histidine residues contribute to coordinating these cations and could be involved in cation translocation. This speculation should be used cautiously as the ionic radii described above are for de-hydrated ions. Hydration of these transition metals during translocation would change an analysis of our results.

In order to identify the driving force conditions, we tested a series of conditions. It is now evident from the experimental results (Figure 10) that extracellular accessible histidine residues are important for zinc transport activity. Furthermore the pK_a of histidine under physiological condition is 7.8. Both of these factors lead us to hypothesize that a change in extracellular pH would lead to a change in uptake. Although, an analysis of result (Figure 11A) shows that change in pH is not affecting zinc transport, one needs to be careful in extrapolating these results. To measure the pH contribution in Zn²⁺ transport, we used HEPES buffer, which has buffer capacity of 6.8-8.2. On the other hand, replacing sodium chloride with different ions did not help us to identify the driving force; replacement with sodium acetate and sodium citrate showed significant decreases in uptake. Since sodium acetate and sodium citrate are known to decrease the intracellular pH, the change in uptake could be due to a change in intracellular composition.

In conclusion, our study reveals that hZIP4 is a metal ion transporter which can transport Zn^{2+} , Ni^{2+} , and Cu^{2+} . Transport is either directly or indirectly mediated by accessible extracellular histidine residues. Our results, combined with those from other laboratories, suggest that the ZIP family of proteins have a more diverse set of substrates than originally postulated and that in order to understand the functional significance of each of these proteins, it may be useful to directly measure transport for each member of the ZIP family of proteins. However, it is important to acknowledge that our experiments have not been performed in the native environment of hZIP4 and thus one must be careful in translating our results to physiological function. *In vivo* it is worth noting that mutations in hZIP4 result in a zinc deficiency disease and mutations in the copper transport protein (CTR) family result in copper deficiency diseases¹¹². Therefore, while hZIP4 is unlikely to be a main avenue of cellular copper uptake, hZIP4 is essential for maintaining cellular homeostasis of zinc.

Lastly, we have tested *in situ* application of a new strategy to release metal ions from a chelating ligand using a photodecarboxylation reaction. NTAdCage binds Zn^{2+} with sub-pM affinity and exhibits a reduction in metal binding affinity after efficient uncaging with 365 nm light. We have applied NTAdCage to a Zn^{2+} uptake assay with hZIP4, which demonstrates this photocage can be used to study the zinc induced complex cellular signaling mechanisms.

3. Computational modeling and functional studies provide a structural scaffold for the zinc transporter hZIP4

Note: Computational modeling studies were done in collaboration with David Baker's lab at the University of Washington, Seattle, WA 98195. I thank Sergey Ovchinnikov, Dr. Hetunandan Kamisetty and Dr. David Baker for the computational model experiments and results.

3.1 Introduction

ZIP member proteins have been shown to transport a variety of transition metals including Fe^{2+} , Zn^{2+} , Cu^{2+} , and Cd^{2+} ⁷⁴. Also, complementation studies have provided some evidence of residues of mechanistic importance ^{113, 114}. However, direct examination of residues of functional importance or cation selectivity has not been shown. In chapter 2, we demonstrated that an excess of Ni^{2+} and Cu^{2+} could inhibit Zn^{2+} transport mediated by hZIP4. Furthermore, both Ni^{2+} and Cu^{2+} could be transported by hZIP4 in addition to Zn^{2+} . To further explore the residues of functional importance for hZIP4, we determined that covalent labeling of extracellular water accessible histidine residues (DEPC) but not free cysteine residues (maleimide) inhibited Zn^{2+} translocation. Based on our earlier results, we set out to explore the role of transmembrane histidine residues in transition metal transport. We mutated each of the TM histidine residues into alanine residues and conducted kinetic studies for each mutant. Analysis of our experimental results demonstrate that although conserved histidine residues are not required for hZIP4 function, mutation of these residues can affect the zinc transport kinetics of hZIP4 protein. Additionally, our results also suggested that a highly variable residue contributes to cation translocation. Based on our results, we hypothesized that transmembrane histidine residues can influence the zinc translocation pathway.

To further explore the zinc translocation pathway in hZIP4 protein, we also took the advantage of recent progress in predicting residue pair contacts in a protein structure using co-evolution data to generate a first molecular model of hZIP4 using Rosetta in combination with co-evolution data ^{115, 116}. The model protein structure generated by Rosetta *ab initio* structure method uses constraint database generated by the combinations of various computational tools, which are explained below.

- 1) Generation of a multiple sequence alignment (MSA) database is the first and one of the most important steps for making a model protein structure using the Rosetta *ab initio* method ¹¹⁷. The higher the sensitivity and accuracy of the MSA database, the higher the

accuracy of co-evolution based protein structure prediction¹¹⁷. MSA is a technique to visualize the relationship between residues of two or more protein sequences. In general, most techniques used in generating the MSA database are based on the conservation of 20 amino acids along with known secondary and tertiary protein structures, catalytic sites, active motifs, post-translational modifications and other properties of proteins. However, each algorithm technique has a different sensitivity, speed and precision. For example, MUSCLE and MAFFT are two of the most popular tools to generate MSA databases that also uses conservation and coevolution as a parameter^{118, 119}. One problem with these tools is that when sequence identity falls below threshold, the sequence is excluded from the database. The exclusion of this sequence all together results in reduced sensitivity as well as precision. To overcome this problem, a more sensitive probabilistic technique based models have been developed, which are based on the likelihood for insertion, deletion, and mutation of an amino acid residues in a given protein sequence and aligned sequences¹²⁰. One of the most popular probabilistic bases models is the hidden Markov model (HMM). The HMM based models are position specific and they calculate the probability of an amino acid at a particular position¹²¹. The result of this analysis is used as initial constraints in predicting the residue-residue contacts.

- 2) HMM-based models are of great value in predicting the topology of protein. However, HMM based models use very simple topologies. HMM based MSA learning models limit the estimations of interactions to the neighboring amino acid residues, which results in overemphasis of the distribution of amino acids rather than the sequence of the protein. Therefore, a HMM model identified MSA database is further optimized to derive a more global relationship between a particular amino acid residue with the rest of protein. Generative REGularized ModelS of proteINs (GREMLIN) is one of the algorithms that used HMM model identified MSA database to generate global statistical model that

simultaneously captures the conservation and co-evolution patterns in the input alignment¹¹⁶. Strongly co-evolving residue pairs as identified by this approach are highly likely to be in contact with each other in the three dimensional structure¹¹⁶. The predicted co-evolved residues are used to generate the contact map. The contact map is a three dimensional representation method for predicted residue-residue interactions of a protein.

- 3) Finally, the Rosetta *ab initio* structure prediction program is used to generate a three dimensional protein structure. The program identifies local sequences that are similar to other solved protein structures and uses them to generate a three dimensional structure. To reduce the sampling space in protein model prediction, the energy function constraint along with predicted residue-residue contacts and transmembrane helices are used. The Rosetta *ab initio* protocol consists of two stages: in the initial stage (“centroid”) side-chains are represented by fixed center-of-mass atoms allowing for rapid generation and evaluation of various protein-like topologies; the second stage (“full-atom”) places all-atom sidechains into a starting topology and iteratively refines the model until a low energy structure is found^{115, 122}. For every predicted structure, an energy function is defined using Bayesian probability theory and in conjunction with Monte Carlo sampling the possible protein structures are identified that are energetically stable and compact.

In this study, the hZIP4 model generated by the Rosetta *ab initio* method was compared with mutagenesis studies that probed residues important for transition metal translocation and specificity. The model also has a similarity to the central transition metal coordination site of the Znt exporter, YiiP^{37, 123}. Comparison of these structures suggests that the Znt and ZIP families may share a common zinc coordination geometry.

3.2 Materials and Methods

3.2.1 Reagents

The radio-isotopes $^{59}\text{FeCl}_3$ were purchased from Perkin-Elmer (Waltham, MA). All transition metal chloride salts were purchased from Alfa Aesar, Inc. (Ward Hill, MA). Additional chemicals were purchased from Sigma-Aldrich Corp. (St. Louis, MO) unless otherwise indicated.

3.2.2 Expression of hZIP4 in *Xenopus laevis* oocytes

Preparation of plasmid constructs and mRNA were performed as previously described in Chapter 2. Site-directed mutagenesis was performed using QuikChange according to the manufacturer's instruction (Agilent Technologies). Following mutagenesis, the entire gene was sequenced using a commercial service (Eton Bioscience Inc.). mRNA was prepared for each mutant and was used to express hZIP4 protein in oocytes as described in chapter 2.

3.2.3 Radio-isotope uptake assay

Radio-isotope uptake assays were performed as described in chapter 2. To identify the zinc competing divalent metal, we performed competition experiments similar to WT hZIP4 (see Chapter 2) by incubating mutant hZIP4 protein expressing oocytes with $3\ \mu\text{M}$ $^{65}\text{ZnCl}_2$ and $600\ \mu\text{M}$ of various transition metals similar to WT hZIP4 competition experiments. Similar to WT hZIP4 protein, we studied the transport kinetics for each of the mutated hZIP4 protein using the zinc radio-isotope uptake assay as described in chapter 2. To study the iron uptake assays, we first incubated $^{59}\text{FeCl}_3$ with 100 fold excess of ascorbic acid to reduce iron to Fe^{2+} . We performed iron uptake assay by incubating hZIP4 protein expressing oocytes with $5\ \mu\text{M}$ and $10\ \mu\text{M}$ of radio-isotope iron for 1 hour in reducing condition.

3.2.4 Detection of hZIP4 surface expression in oocytes

hZIP4 surface expression was detected using EZ-Link Sulfo-NHS-SS-Biotin and Biotinylation Kit (Thermo Scientific Co.) according to the manufacturer's instructions. In brief, 35 oocytes 72 hours post-injection were washed three times with ice-cold PBS (0.1 M sodium phosphate, 0.15 M NaCl, pH 7.2) before incubating them with 2 ml of biotinylation buffer. Sulfo-NHS-SS-Biotin was dissolved in PBS to a final concentration of 0.11 mg/ml and oocytes were incubated with biotinylation buffer for 90 minutes at 4° C with gentle shaking. The reaction was stopped upon addition of 200 µl of quenching solution. Biotin-labelled oocytes were washed 4 times with TBS (0.025 M Tris, 0.15 M NaCl, pH 7.2). Finally, oocytes were re-suspended in 500 µl of solubilization buffer [TBS buffer containing 1 % (w/v) n-dodecyl-beta D-maltoside (DDM) and 1 mM phenylmethanesulfonyl fluoride (PMSF)]. Oocytes were homogenized by passing them through a 25 gauge needle. The lysate was centrifuged at 14000g for 20 minutes at 4°C. The supernatant was collected into microcentrifuge tubes. The pellet was re-suspended in solubilization buffer and centrifuged at 14000g for 20 minutes at 4°C. The supernatants were mixed and incubated with 50 µl of NeutrAvidin resin at room temperature for 60 min with gentle shaking. The resin was washed four times with solubilization buffer. Finally, biotinylated proteins were eluted by boiling resin with Laemli buffer for 20 minutes. The eluted biotinylated proteins were separated on SDS-PAGE. hZIP4 was detected by Western blot with a rabbit polyclonal antibody raised against the N-terminus of hZIP4 (Aviva System Biology Corp.).

3.2.5 Computational modelling of the hZIP4 protein (In collaboration with the David Baker lab, University of Washington and Howard Hughes Medical Institute)

3.2.5.1 Prediction of contact residues in hZIP4 protein

In this experiment, the input sequence of hZIP4 was trimmed to only include the following residues: 328-427,487-642. This trimmed sequence excludes the extracellular N-terminal domain and the

only significant intracellular domain between TM3 and TM4. Both of these domains have substantial variation between species. A multiple sequence alignment was generated using HMM-HMM Based Lightning-fast Iterative sequence Search (HHblits)¹²⁴ with the following options: -n 8 -e 1E-20 -maxfilt ∞ -neffmax 20 -nodiff -realign_max ∞ . HHblits is a statistical model that uses HMM to generate an MSA. It has been proposed that when MSA generated using the HHblits model, it has higher sensitivity and accuracy that increases the accuracy of co-evolution based protein structure prediction. The resulting alignment was then filtered to exclude any sequence that did not cover at least 50 percent of the query and to reduce the sequence redundancy to 90 percent. The MSA data generated using HHblits was run with GREMLIN default parameters.

3.2.5.2 Rosetta Membrane ab initio modeling for hZIP4

In this experiment, the standard Rosetta *ab initio* was used to model the three-dimensional structure of hZIP4 trimmed to only include residues 328-648. The default Rosetta energy function was modified to enable membrane specific terms with the following weights: fa_sol - 0.0, fa_mbenv - 0.3, fa_mbsolv - 0.35 and Menv_smooth - 0.5^{125, 126}. Transmembrane spans (residues 2-23, 33-53, 74-95, 167-191, 197-222, 228-252, 259-282, and 290-314) were defined using the consensus output of the MEta Sever for Sequence Analysis (MESSA server)¹²⁷. MESSA server is a computational sequence analytical tool that can be used to predict the local sequence properties, spatial structure and function together. To reduce the sampling space in hZIP4 model prediction, sigmoidal restraints that modified the energy function were introduced. The shape of the sigmoid is defined using a distance cutoff, the slope, the intercept and the strength of the weight parameter using an equation described below.

$$\text{sigmoid}(d) = \frac{\text{weight}}{1 + \exp(-\text{slope}(d - \text{cutoff}))} + \text{intercept}$$

To favor sampling of topologies consistent with GREMLIN predictions, sigmoidal distance restraints (Figure 14) were introduced between residue-pairs predicted to be in contact by GREMLIN (Figure 15). When used in the centroid stage of Rosetta, these restraints were introduced between carbon-beta atoms (carbon-alpha in the case of glycine), at amino acid pair specific C β -C β cutoff and slopes, as described in SI Table III within¹¹⁶; in the full-atom stage, these were replaced with ambiguous distance restraints between side-chain heavy atoms (cutoff of 5.5 and slope of 4)¹²⁸. The relative weight of each restraint was based on the GREMLIN score. The total atom-pair restraint score was scaled to be roughly ½ the total Rosetta score.

In addition to these restraints, additional strong repulsive distance restraints (weight -100, cutoff 35, slope 2 and intercept of 100) were added between extracellular regions (defined by residues 329,391,522,582,648) and intracellular regions (defined by residues 353,425,490,553,615), and strong attractive restraints (weight 100, cutoff 35, slope 2 and intercept of 0) within intracellular regions and extracellular regions, effectively constructing a membrane-like sampling space (Figure 14). These restraints were introduced between pairs of C α atoms.

The top 1010 models ranked by distance restraints score, with z-score ≥ 2 (Figure 16) were clustered based on structural similarity as calculated by TMscore¹²⁹ after excluding the regions (positions 428-486 and 643-648). Clusters were defined as connected components of a network, where each edge is between models with TMscore ≥ 0.7 . The selected model was then further energy minimized with Rosetta to remove clashes, while respecting structural symmetry and GREMLIN restraints¹³⁰.

Figure 14. Sigmoidal distance restraint function. “d” is the distance between given distance evaluated

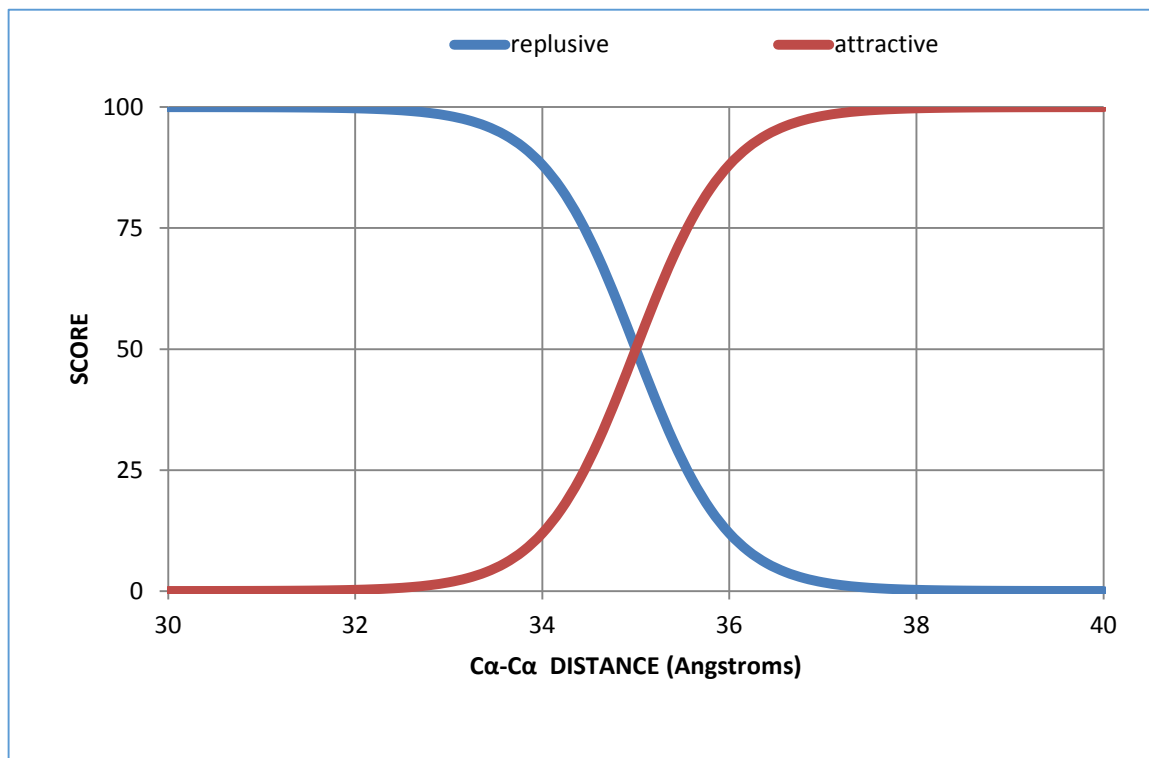


Figure 15. Contact map showing top co-evolved TM residues in hZIP4. A) Contact map, left to right, top to bottom (N to C-terminus) showing the top 384 co-evolving residues between transmembrane helices represented as a contact map. The darker and larger the blue dots, the higher strength in covariance. B) Table of inter-helical residue pairs, within the top 64 predictions. The matching labels are shown in bottom-left portion of the contact map (A)

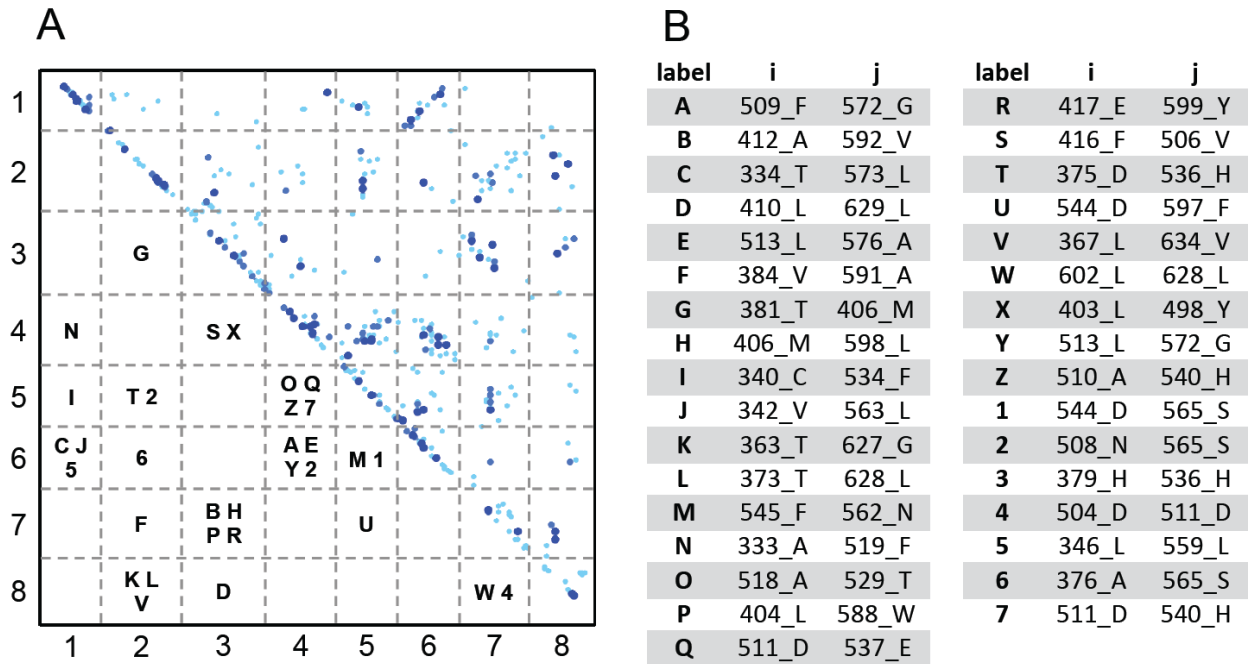
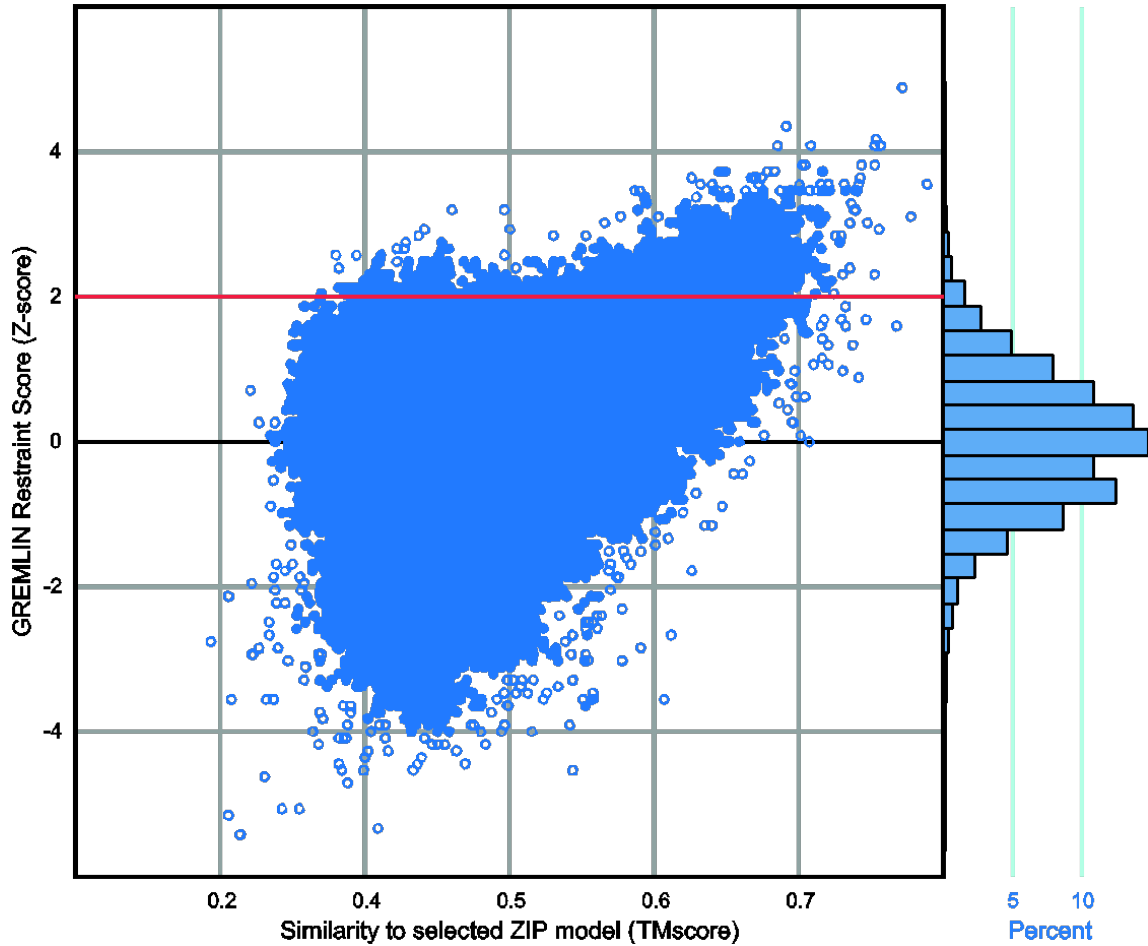


Figure 16. Distribution of GREMLIN restraint scores for Rosetta Ab initio models. Models above the red line (with z-score ≥ 2) were selected for the clustering analysis. The selected model is the refined model from cluster A (See Figure 21A). The Ab initio models closer to the selected model tend to have a higher GREMLIN restraint score.



3.2.6 Oligomeric state of hZIP4

Adapting the protocol from Dürr et al, 50 oocytes were added to breaking buffer [20 mM HEPES, pH 7.4, 150 mM NaCl and 1 mM phenylmethanesulfonyl fluoride (PMSF)] and passed through a 25 gauge needle followed by one minute low speed centrifugation (100g and 4° C)¹³¹. The supernatant was collected in a separate micro-centrifuge tube and centrifuged (1 minute at 100g and 4° C). The procedure was repeated until no pellet was observed upon centrifugation. The supernatant was then spun down at 14000g for 30 minutes at 4° C. The membrane pellet was re-suspended in solubilizing buffer (20 mM HEPES, pH 7.4, 150 mM NaCl, 1% w/v DDM and 1 mM PMSF) and incubated at room temperature for 5 minutes. The insoluble fraction was separated by high speed centrifugation (14000g for 30 minutes at 4° C). The supernatant was added into Laemmli buffer in the absence of reducing agent. The solubilized total membrane proteins were separated on SDS-PAGE. The Western blot was developed using rabbit polyclonal antibody raised against N-terminus of hZIP4 (Aviva System Biology Corp.).

3.2.7 Glycosylation of hZIP4

Fifty oocytes were either injected with either 500 ng of hZIP4 mRNA or co-injected with 500 ng of hZIP4 mRNA and 10 ng of tunicamycin. The oocytes were incubated in ORI⁺ buffer for three days. Post hZIP4 expression, the hZIP4 surface expression was measured using the protocol described earlier in 3.2.4.

3.3 Results

3.3.1 The effect of histidine to alanine mutations on hZIP4 zinc transport

Based on our earlier finding that covalent modification of histidine, but not cysteine residues, dramatically decreases zinc translocation mediated by hZIP4, we designed experiments to examine the functional role of each histidine residue within the transmembrane domains of this protein for transition metal translocation. hZIP4 encodes six transmembrane histidine residues: 379 (TM2), 507 (TM4), 536, 540 and 550 (TM5) as well as 624 (TM8). We individually replaced each TM histidine residue with alanine. Zinc transport kinetics were determined for each of the mutant transporters using our established uptake assay. Previously, we have demonstrated that the wild type hZIP4 has two distinct K_m 's: 76 ± 5 nM and 1.4 ± 0.3 μ M. Alanine substitution at the TM histidine residues altered the nM K_m for three mutant proteins: H379A, H507A and H536A (Table 5). In addition, alanine replacement abolished the μ M K_m for one mutant protein (H379A). Equally, no zinc translocation was observed for the H624A mutant (data not shown).

Representative data for one of these mutants (H540A) is shown in Figure 17. Furthermore, to directly compare V_{max} between the wild type and mutant constructs, oocytes expressing each construct were incubated with 3 μ M $^{65}\text{ZnCl}_2$. When normalizing the data to surface expression, the V_{max} was significantly lower for the H379A, H507A, H536A, H540A and H624Q mutants (but not H550A) when compared to the WT protein (Figure 18). Analysis of transport data for some constructs revealed Hill coefficients with non-Michaelis-Menten behavior (Table 5). This could be due to one or more factors including a flip-flop model where a dimeric transporter has reciprocal conformations, a ping pong mechanism or random substrate binding if more than one zinc atom is transported per transport cycle^{132, 133}. It was also determined that zinc transport was roughly linear over the time of the assay (60 min) upon addition of 21.75 μ M $^{65}\text{ZnCl}_2$ (Figure 19). We have previously demonstrated that under these conditions, $^{65}\text{Zn}^{2+}$ uptake is linear for WT-hZIP4 over 2 hours as shown in Chapter 2.

Figure 17. The Zn^{2+} transport parameters, K_m and V_{max} , of the H540A mutant. The kinetic parameters for hZIP4 mutant was elucidated at low (A) and high (B) concentrations of zinc by measuring amount of $^{65}Zn^{2+}$ uptake into oocytes injected with hZIP4-Strep (with H540A mutant) mRNA over one hour in assay buffer which contained varying amounts of $^{65}ZnCl_2$. The data was fit to the Michaelis-Menten equation described in the text; data originated from 5-8 oocytes; values are means \pm SEM.

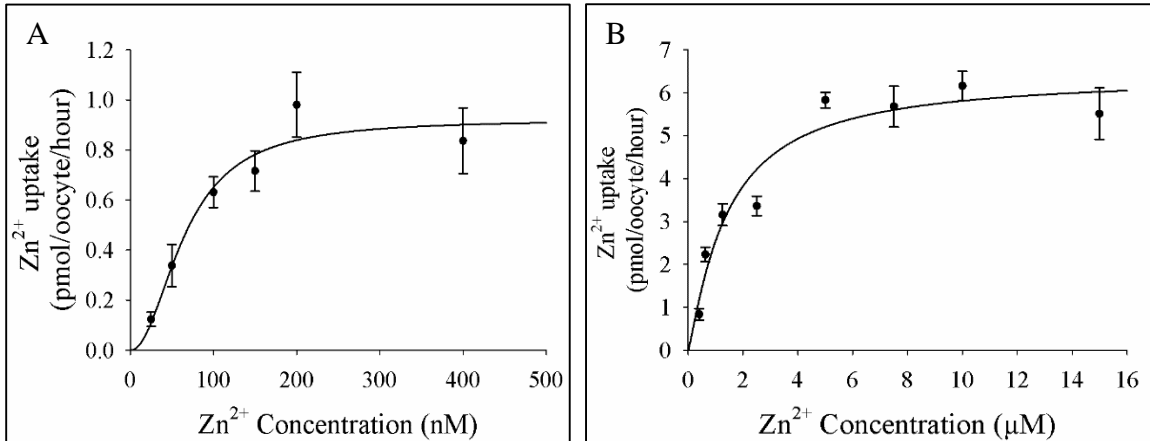


Figure 18. Relative velocity of WT hZIP4 and mutant transporters. (A) Oocytes were injected with 25 ng of WT hZIP4 or mutant hZIP4 mRNA. After 3 days of incubation at 16° C, oocytes were subjected to radioisotope uptake experiment. Oocytes were incubated with 3 μ M $^{65}\text{Zn}^{2+}$ and zinc uptake was measured after 60 min. Transport data was normalized to surface expressed protein (Figure 8B). * indicates a statistically significant difference in zinc uptake between mutant hZIP4 and WT after uptake was normalized to level of protein surface expression ($p < 0.05$). (B) Western blot of surface expressed WT and mutant hZIP4 proteins isolated as described in Materials and Methods. The relative expression of hZIP4 was quantified using Quantity One software (Bio-Rad Laboratories, Inc.). (C) Western blot of biotinylated WT and mutant hZIP4 proteins isolated as described in Materials and Methods.

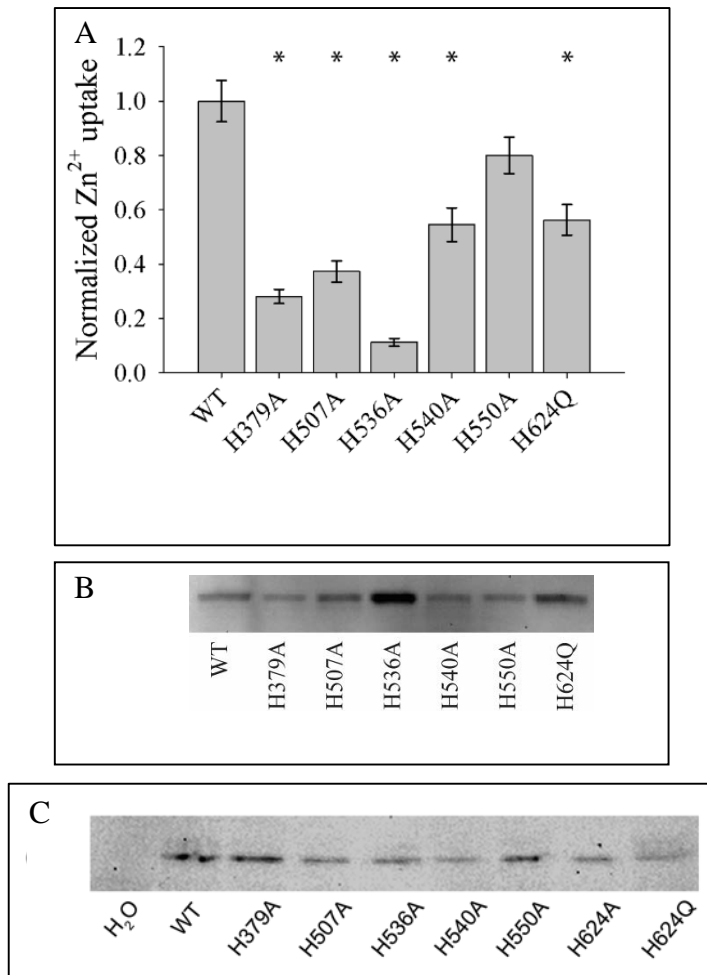
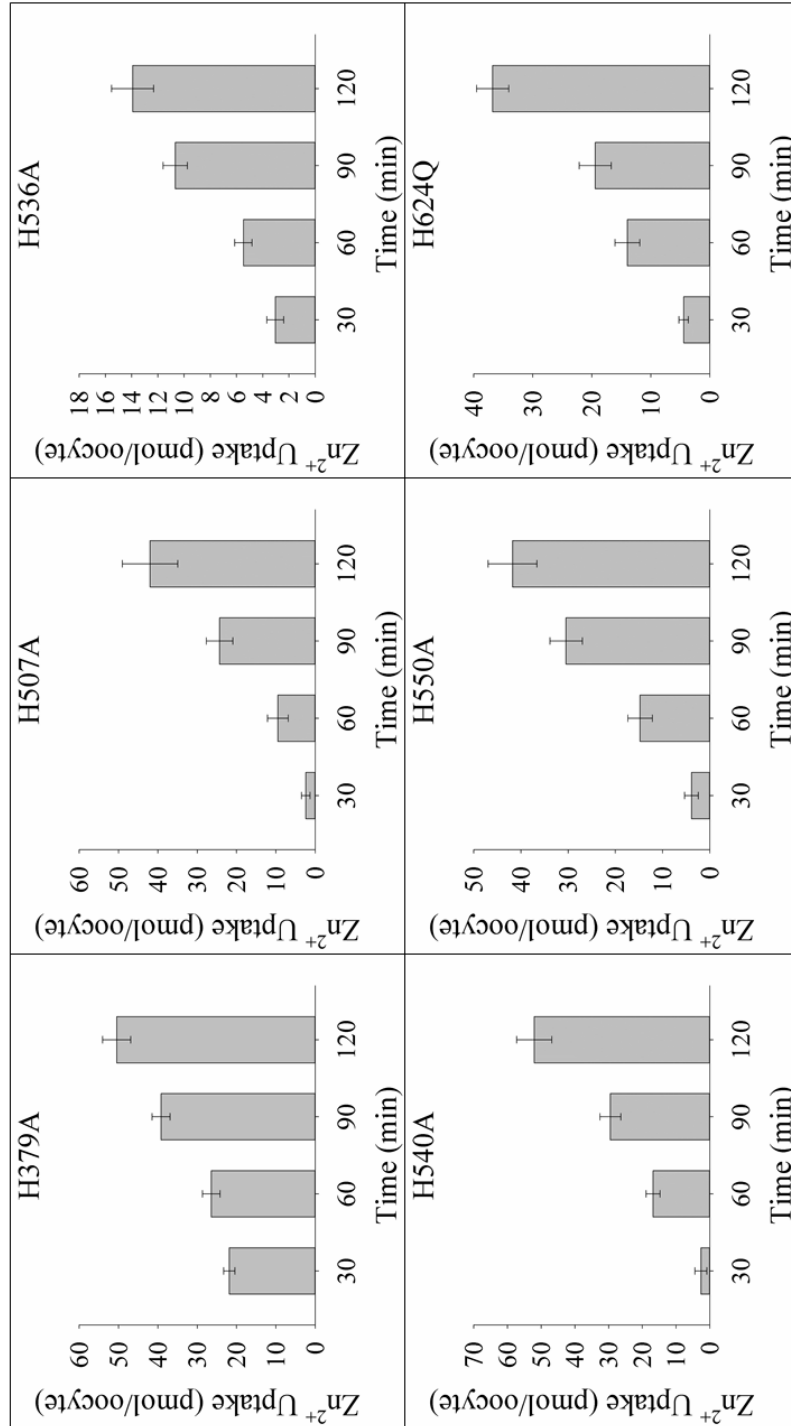


Table 5. Zinc Transport Kinetic Parameters for WT and mutant hZIP4 transporters. Kinetic parameters were determined by measuring amount of zinc taken up with hZIP4-Strep mRNA as described in the methods and materials. The data were fit to the Michealis-Menten equation as described in the materials and methods. Data originated from five to eleven oocytes, values are means \pm SEM. Km values statistically different ($p < 0.05$) from wt hZIP4 are in bold. No statistical tests were performed on Vmax as assays were performed on separate days and surface expression was variable between days. N.D. = none detected.

	V_{max}(1) (pmol/oocyte/ hour)	n₁	K_m1 (nM)	V_{max}(2) (pmol/oocyte/ hour)	n₂	K_m2 (μM)
WT	1.4 \pm 0.1	3.6 \pm 0.6	76 \pm 5	13 \pm 1	1.2 \pm 0.3	1.4 \pm 0.3
H379A	0.8 \pm 0.01	4.2 \pm 0.7	370 \pm 10	N.D.	N.D.	N.D.
H507A	0.6 \pm 0.1	6.1 \pm 2.9	220 \pm 20	2.3 \pm 0.2	0.9 \pm 0.1	1.8 \pm 0.4
H536A	0.7 \pm 0.1	2.4 \pm 1.1	210 \pm 50	3.1 \pm 0.3	1.3 \pm 0.3	1.9 \pm 0.5
H540A	0.9 \pm 0.1	2.1 \pm 0.8	70 \pm 20	6.5 \pm 0.9	1.2 \pm 0.4	1.4 \pm 0.6
H550A	0.4 \pm 0.1	1.2 \pm 0.7	60 \pm 30	0.8 \pm 0.01	1.8 \pm 0.3	0.5 \pm 0.1
H624A	N.D.	N.D.	N.D.	N.D.	N.D.	N.D.
H624Q	1.1 \pm 0.1	1.8 \pm 0.9	60 \pm 17	3.3 \pm 0.1	2.9 \pm 0.9	0.8 \pm 0.1

Figure 19. Time course of zinc uptake for mutant constructs. Oocytes, injected with 25 ng of hZIP4 mutant constructs were incubated with 21.75 μM $^{65}\text{ZnCl}_2$. The assay was quenched every 30 min up to 120 min, and data originated from five to eight oocytes; values are means \pm SEM. Fitting the data to the equation to a standard linear equation ($y = mx + b$) resulted in the following R2 values: H379A (0.9685), H507A (0.9683), H536A (0.9824), H540A (0.9816), H550A (0.9949) and H624Q (0.9493).



3.3.2 Histidine 624 is essential for biometal translocation

Hydropathy analysis predicts that H624 is located on the cytoplasmic end of TM8 and is not conserved among ZIP family proteins. Considering that ZIP member proteins which function as iron transporters (ZIP8 and ZIP14) encode glutamine at this position, we replaced histidine with glutamine at this position to further elucidate the role of this residue in transition metal permeation. The H624Q mutation retained zinc translocation function, while having a tighter μM K_m (Table 5). To further explore the functional role of H624 in biometal translocation, we performed a competition experiment where 200 fold excess of various divalent cations were added to our uptake assay in the presence of $3 \mu\text{M}$ $^{65}\text{Zn}^{2+}$. Previously, we have shown that in the wild type transporter, zinc transport is inhibited by 200-fold excess Cu^{2+} , Ni^{2+} , and Zn^{2+} . In addition, Zn^{2+} , Cu^{2+} and Ni^{2+} are transported by hZIP4. In contrast to the wild type transporter, $^{65}\text{Zn}^{2+}$ transport was significantly inhibited by Cu^{2+} , Ba^{2+} , Co^{2+} , Fe^{2+} , Mn^{2+} , Ni^{2+} and Zn^{2+} for the H624Q mutant transporter (Figure 20).

3.3.3 Residues contribute to cation selectivity of ZIP transporters

To explore the role of the transmembrane histidine residues in cation specificity for hZIP4, we examined the relative velocity of Fe^{2+} and Zn^{2+} uptake for wt and each mutant construct (Table 6). The rationale for this experiment was the observation that zinc transport was inhibited for the H624Q mutant construct by high levels of iron in our competition assay. Therefore, we hypothesized that the H624Q mutant hZIP4 transporter would translocate Fe^{2+} . Analysis of our experiments demonstrated that wild type hZIP4 transports Fe^{2+} , but that the H624Q mutant transporter is a poor iron transporter. Equally, replacement of three histidine residues with alanine significantly altered the velocity ratio of Fe^{2+} and Zn^{2+} transport (H379A, H507A and H536A) (Table 6).

Figure 20. Competition of $^{65}\text{Zn}^{2+}$ uptake in H624Q expressing oocytes with a series of divalent cations. To determine which divalent cations inhibited hZIP4-mediated $^{65}\text{Zn}^{2+}$ uptake, oocytes expressing hZIP4 were pre-incubated in 600 μM cold ZnCl_2 , BaCl_2 , CdCl_2 , CoCl_2 , CuCl_2 , FeCl_2 , MgCl_2 , MnCl_2 , or NiCl_2 in the uptake assay buffer. The uptake assay was initiated by adding 3.0 μM $^{65}\text{ZnCl}_2$. The assay was quenched after one hour as described in the Materials and Methods section; data were normalized to the amount of $^{65}\text{Zn}^{2+}$ uptake in the absence of competing cation; data originated from 14-17 oocytes; values are means \pm SEM. Data marked with * represents statistically significant different from wt ($p < 0.05$).

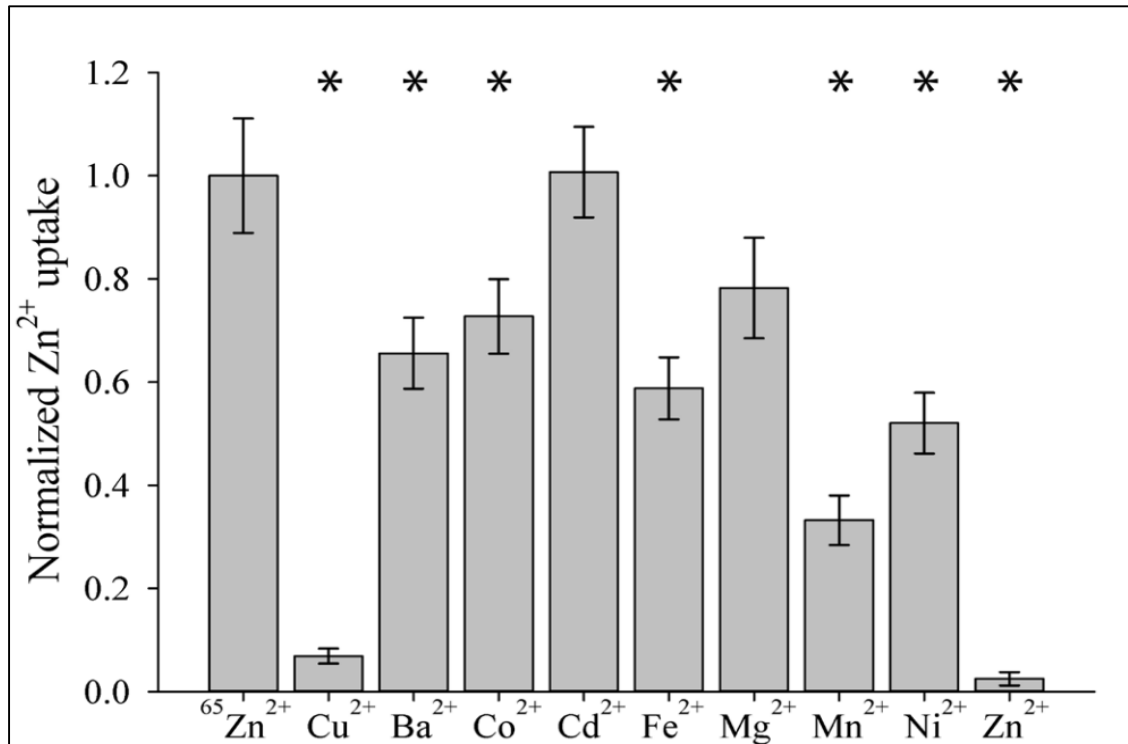


Table 6. Relative Specificity for Zn²⁺ and Fe²⁺ for WT and mutant hZIP4 transporters. A final concentration of 5 μM of indicated metal was applied to oocytes expressing wt or mutant hZIP4 protein. Data originated from eight to eleven oocytes, values are means ± SEM. Zn²⁺/Fe²⁺ uptake values for mutant proteins statistically different (p > 0.05) from wt hZIP4 are in bold. Similar results were obtained upon application of 10 μM of indicated metal. N.D. = none detected.

	Zn ²⁺ Uptake (pmol/oocyte/hour)	Fe ²⁺ Uptake (pmol/oocyte/hour)	Zn ²⁺ /Fe ²⁺ Uptake
WT	2.2 ± 0.2	0.61 ± 0.07	3.6 ± 0.7
H379A	1.3 ± 0.3	0.64 ± 0.04	2.0 ± 0.6
H507A	2.7 ± 0.3	0.38 ± 0.07	7 ± 2
H536A	1.4 ± 0.2	2.1 ± 0.1	0.7 ± 0.1
H540A	3.5 ± 0.5	0.65 ± 0.04	5 ± 3
H550A	1.9 ± 0.2	0.46 ± 0.07	4.1 ± 0.8
H624A	N.D.	0.24 ± 0.05	undefined
H624Q	2.4 ± 0.2	0.26 ± 0.06	9 ± 2

3.3.4 Residue-residue contacts predicted from co-evolution (in collaboration with the David Baker lab)

We built a model of this protein using predicted contact residues and the Rosetta Membrane models and compared the results with non-redundant PDB membrane protein structures^{116, 134, 135}. Membrane structures have been modeled using contact predictions based on co-evolutionary patterns in large MSAs of homologous proteins^{136, 137}. To see if such an analysis was possible for hZIP4, we constructed an alignment over the conserved transmembrane region by querying the UniProt database with HHblits^{124, 138}. The resulting non-redundant alignment contained 1731 homologous sequences, 6.8 sequences per length of 255, which is more than the minimum sequences (5 sequences per length) required to predict residue pairs in contact in the three dimensional structure of hZIP4 using GREMLIN, a co-evolution based contact prediction approach that is more accurate than other extant approaches¹¹⁶. These predictions were then used as distance restraints in the Rosetta *ab initio* protocol along with other membrane-specific terms to generate over 100,000 structural models of hZIP4 using a distributed computing network, Rosetta@home. Of these, the top 1010 models based on restraint score were extracted and the contact map was generated for each predicted protein. An analysis of contact maps of selected co-evolution based top models suggested that they formed three large clusters (Figure 21) of which one cluster agreed with GREMLIN predictions and formed physically realistic structures.

Despite this extensive sampling, we observed one set of predicted contacts that were consistently not made by the structural models (Figure 21A). Further inspection revealed that it was physically impossible to make all these contacts in regions between TM2-3 and TM7-8, without breaking contacts between other helices in a monomeric state. The top 384 (1.5 x length of query) co-evolving pairs of residues that were at least three residues apart (Figure 15) in the protein sequence were then selected to be used in subsequent structural modeling in Rosetta. Using these top co-evolving pairs, an oligomeric interface could be readily made (Figure 22B-C and 23). Notable for

Figure 21. Contact maps showing contacts made within each cluster, below that are cartoons of the top three models colored blue to red (n to c terminus) for each cluster. The intensity of the blue (in the contact map) is indicative of the percent of models within the cluster that make those contacts. Ranging from light blue: 10% to blue 100%. Red boxes indicate helices predicted to be in contact but are not in the given cluster. A) Cluster A makes contacts between all the top co-evolving helices, but there is a disagreement between models in the regions boxed in green. Further analysis reveals that variation within cluster A is explained within the context of dimer helix swapping (Figure 23). Both clusters B and C, have missing helical contacts in regions with strong co-evolution signal. Additionally, they both expose histidines into the membrane, which is highly improbable for membrane proteins.

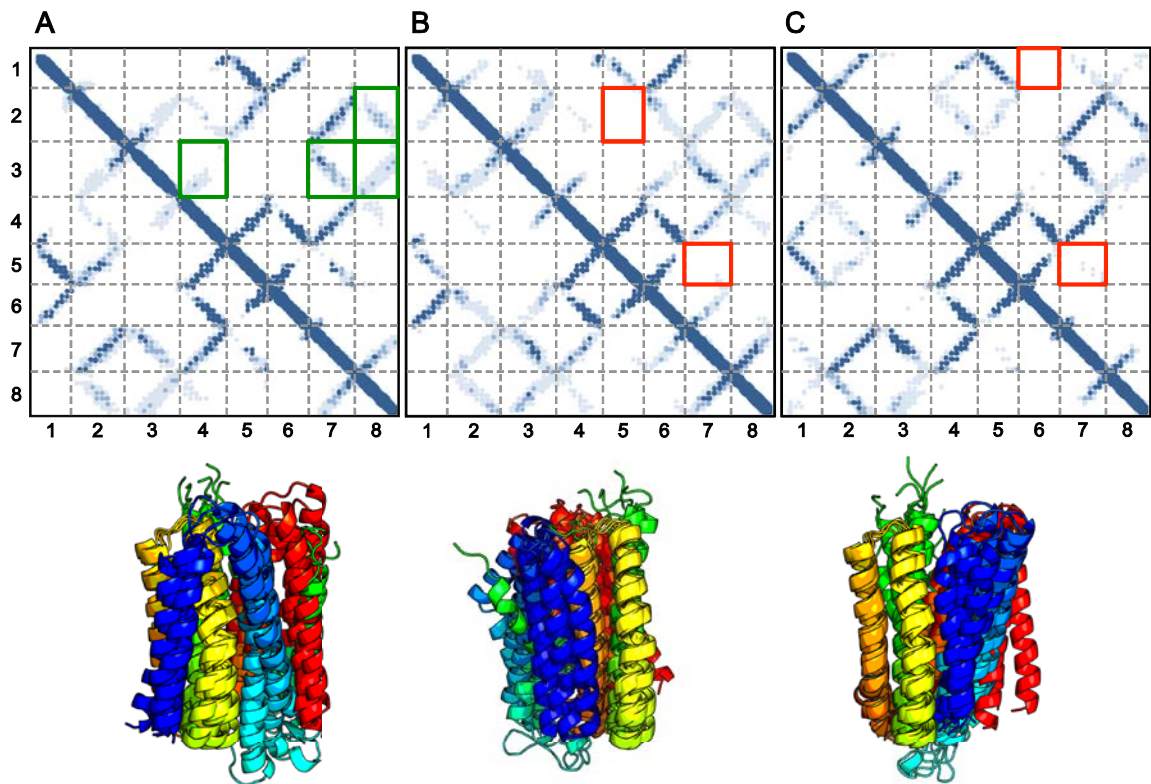
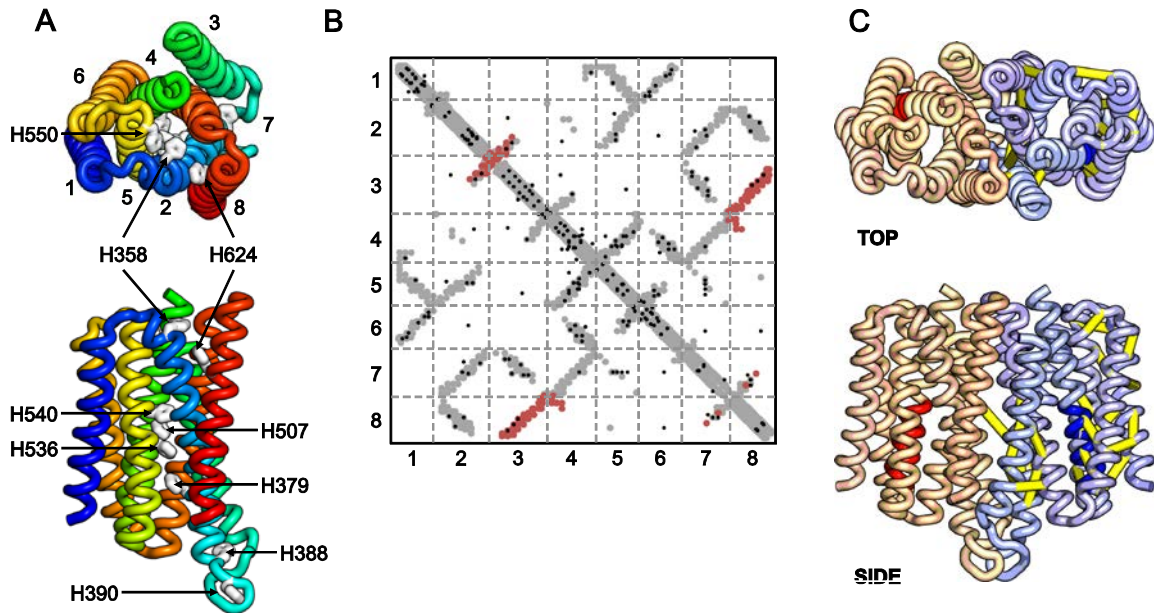


Figure 22. Models of hZIP4 were generated using Rosetta structure prediction guided by coevolution based contacts, as described in the text. A) Ribbon diagram of the monomer structure colored blue to red (n to c terminus), shows the predicted location of the trans membrane histidines in white. For clarity, the loop between residues 428 to 486 is omitted. B) Consistency of coevolution predicted contacts with hZIP4 structural model. Black dots, predicted contacts; grey, contacts in the Rosetta model monomer; red, contacts across dimer interface. The top coevolving residues are made within the context of the dimer. C) Dimer view of the Rosetta structure model of hZIP4. The top 25 contacts are shown as yellow dashes. The highlighted regions (red and dark blue) indicate the conserved LIV-1 sequence in the fourth transmembrane helix.



these results is that each of the variants in cluster within Figure 21A can make the dimer interface as shown in Figure 23. Equally, these models have histidine residues lining the transmembrane core forming a potential permeating pathway (Figure 22A).

3.3.5 Structural Alignment of hZIP4 with membrane protein structures (in collaboration with the David Baker lab)

To examine whether the model of hZIP4 was similar in structure to more distal membrane proteins, we performed structural alignments between the model and all known crystal structures of membrane proteins, in the Protein Data Bank of Transmembrane Proteins (date: 2013-12-27), using TMalign^{134, 135, 139}. The hZIP4 dimeric model is closest in structure to MFS transporters (Figure 24). The highest ranked MFS transporter is PiPT, a eukaryotic phosphate transporter (Figure 25). The MFS and CDF proteins are separate families within the SLC group of proteins¹⁴⁰. PiPT encodes twelve TM domains in a twofold axis of symmetry where phosphate translocation occurs at the two fold axis.

3.3.6 Oligomeric State of hZIP4

TM7 from each monomeric unit are adjacent helices in each of the top ranked models (Figure 23). Therefore, to elucidate whether the oligomeric state of hZIP4 could be disrupted using our model as a template, we replaced residues within TM7 with tryptophan. Oocytes were injected with wt or mutant hZIP4 mRNA. Total membrane proteins were isolated after 72 hours. Following Western blot analysis, it was observed that wt hZIP4 is comprised of both monomeric and dimeric complexes (Figure 26A). Replacement of some, but not all, residues along TM7 with tryptophan resulted in mutant proteins which favor a monomeric state. In our Western blot analysis, we observed three distinct bands, where the higher band indicates dimer and the lower

Figure 23. Variations within cluster A are consistent within context of a dimer. When we examine variation within cluster A, we find that the models are capable of making the remainder of the top co-evolving residues in the context of a dimer. For example, if we reconnect the loop regions between helices 2 and 3, swapping helix 3 between the homo-dimer (A->B), this preserves all predicted helical contacts. Another example would be to reconnect the loop between helices 7 and 8, swapping helix 8 (A->C), or a combination of both (A->D). These swaps are represented in the variation of the top cluster (Figure 21A).

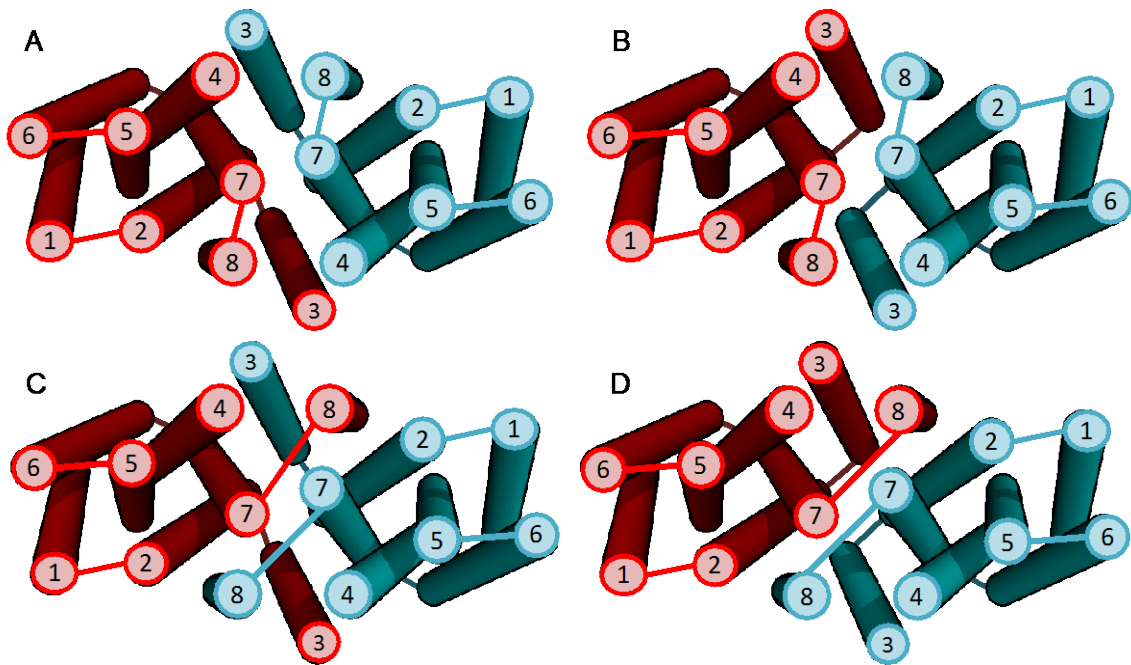


Figure 24. Structural homology of hZIP4 dimer to other membrane proteins. The red filled circles are MFS proteins. EmrE and YiiP are the efflux multidrug transporter and Znt zinc exporter, respectively.

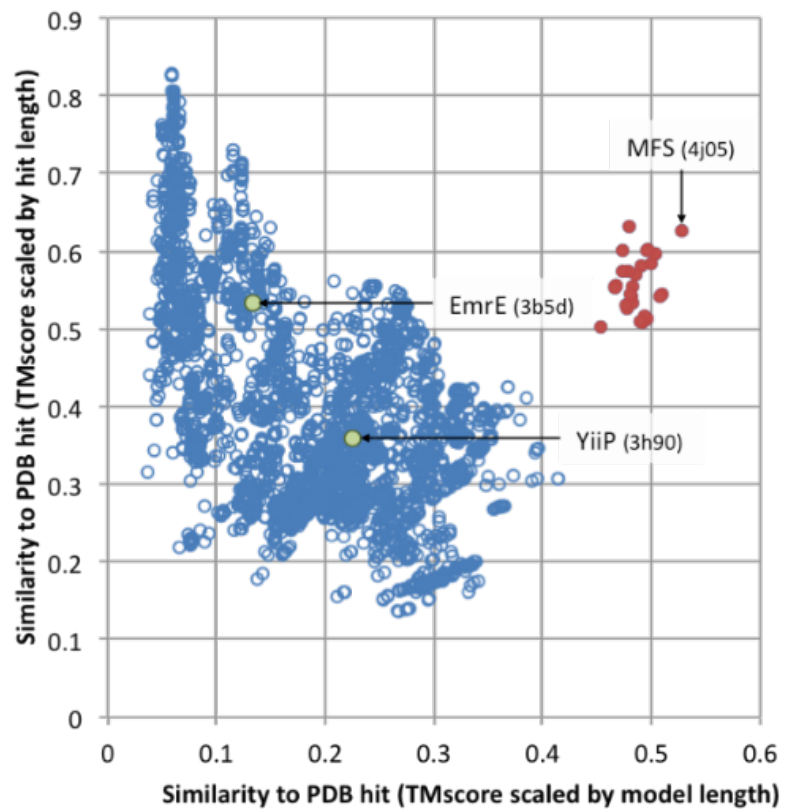


Figure 25. Comparison of hZIP4 model and MFS Transporter structure. A) Similarity of the Rosetta model of hZIP4 with the structure of the Major Facilitator Superfamily (MFS) Transporter (PDB: 4j05). Loop regions and helices 1 and 6 of hZIP4 are not shown for clarity. TM-score 0.66 (3.53 RMSD over aligned region). B) Alignment of trans-membrane helices in sequential space. The matching colors of hZIP4 and MFS indicate structural alignment. The grey regions did not align and were not shown in (A).

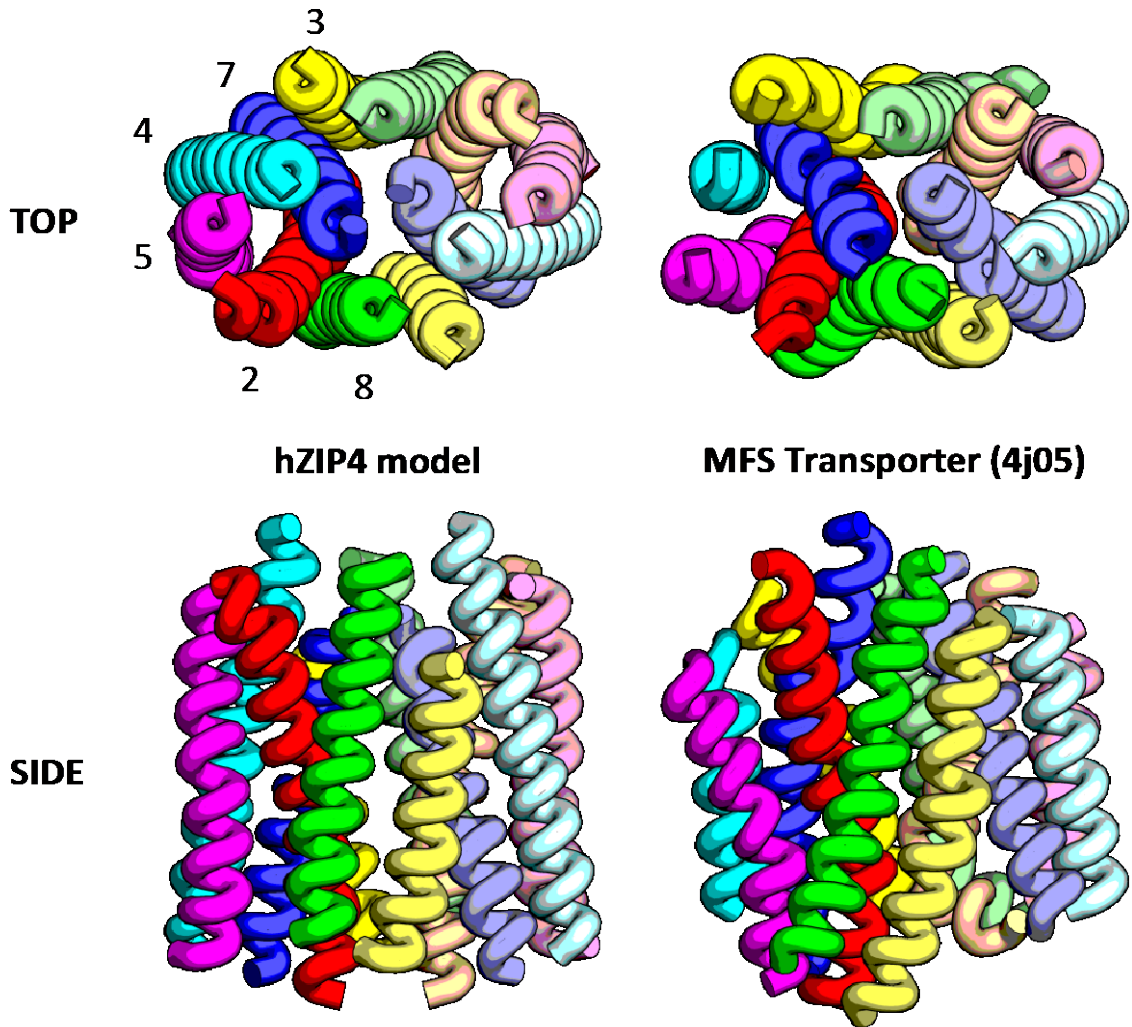
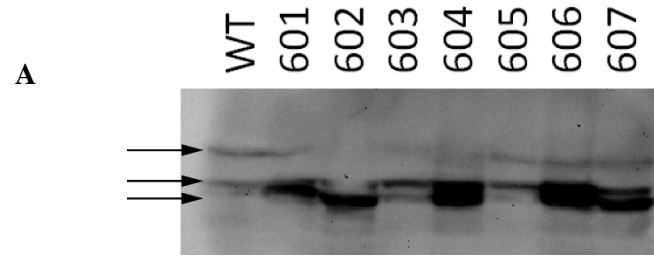
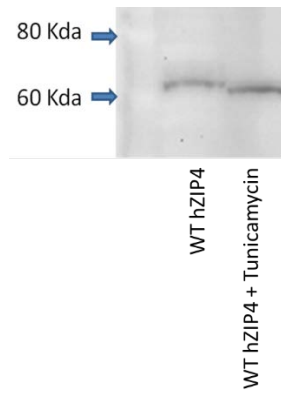


Figure 26. Western blot analysis of tryptophan scanning mutagenesis studies along TM7. A) Residues replaced with tryptophan are indicated above blot. Arrows represent (from top to bottom) dimer, glycosylated monomer-1 and nonglycosylated monomer-2. B) WT hZIP4 injected oocytes, when co-injected with tunicamycin showed a lower molecular weight of surface expressed hZIP4 suggesting that glycosylation may not be vital to membrane localization.



B



bands indicate two different populations of monomer. Between the two different monomer populations, it is possible that one (monomer-1) is glycosylated and the other (monomer-2) is either non-glycosylated or a differently glycosylated form. Additionally, when oocytes were co-injected with wt-hZIP4 mRNA and tunicamycin, the resulting surface expressed hZIP4 protein had lower molecular weight than when injected with wt-hZIP4 mRNA alone. The result of our tunicamycin injected hZIP4 protein surface expression suggests that glycosylation may not be important for hZIP4 membrane localization. However, we have not measured the Zn^{2+} transport in non-glycosylated hZIP4 protein expressing oocytes. Others have observed a similar pattern of two monomeric states⁹⁷. Notably, the L602W mutation resulted in nearly all of hZIP4 in the monomer-1 state. Equally the D604W mutation greatly diminished the dimer population, however overall distribution of monomers is not affected for this mutant protein. Finally, the M605W mutation did not affect the relative distribution of hZIP4 oligomeric states.

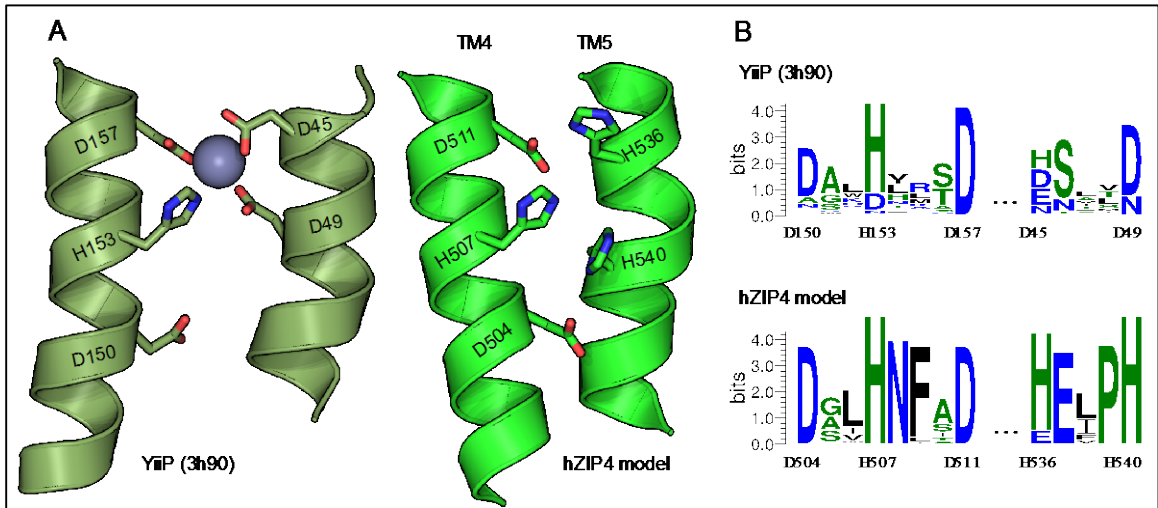
3.4 Discussion

In this study, we designed experiments to investigate the zinc permeation pathway in hZIP4 protein. Our earlier experiments suggested that extracellular water accessible histidine residues are important for hZIP4 mediated zinc transport. To further investigate the role of TM histidine residues, we mutated each of the six histidine residues predicted based on hydrophathy analysis to alanine. Our zinc uptake assay for each of the alanine mutants showed that the mutation affects either K_m (Table 5) or the rate of transport (Figure 18), which suggests that these residues are either part of the zinc permeation pathway or are important for maintaining structural integrity of the permeation pathway. It is worth noting that our V_{max} results have certain caveats. For example, we did not measure the labelling efficiencies of the biotinylating reagents, optimize avidin bead/total membrane protein ratio or determine the avidin bead bed volume to bind all the labelled protein¹⁴¹. We understand that the interpretation of our V_{max} results may change, if they were to be reanalyzed with more detailed surface biotinylation experimental conditions. It is plausible that overexpression of hZIP4 may result in protein misfolding which may lead to distinct protein populations with altered transport kinetics or metal specificity. While K_m or normalized V_{max} values between differing expression systems may differ, it is likely that trends, such as mutations which result in higher/lower affinities or changes in normalized V_{max} , will be consistent between overexpression systems. Furthermore, considering that both micromolar and nanomolar K_m values have been observed upon heterologous expression in mammalian cells as well as *X. laevis* oocytes, this suggests that either both affinities are present *in vivo* or that overexpression in both cell types gives equivalent artifacts^{64, 74}. Therefore, analysis of hZIP4 transport experiments performed in *X. laevis* oocytes is a viable and valuable method to examine transport properties for this class of proteins. Equally, the non-Michaelis-Menten Hill coefficients could be due to one or more factors including a flip-flop model where a dimeric transporter has reciprocal conformations, a ping pong mechanism or random substrate binding if more than one zinc molecule is transported per transport cycle.

We were surprised to learn that the mutation of histidine to alanine at position 624 resulted in an inactive protein even though H624 is the least conserved residue amongst human LIV-1 subfamily proteins. The loss of activity in H624A mutant could be a result of no protein expressing in plasma membrane. However, our biotin labelling experiment showed that H624A is expressed (Figure 18C) in the plasma membrane. Therefore, we believe that the 624 residue is important for maintaining the structural integrity of the hZIP4 protein. Additionally, mutation of H624 to the second most conserved glutamine residue in human LIV-1 subfamily proteins resulted in rescuing of the zinc transport activity in hZIP4 protein although with a different pattern of substrate specificity (Figure 20) than WT hZIP4 protein.

Seeking to further explain our results and to explore the zinc permeation pathway in hZIP4 protein, we decided to use the GREMLIN contact prediction using the pseudo likelihood approach with Rosetta membrane protein structure prediction method to model the transmembrane (TM) domains of hZIP4. The 327 residue N-terminal domain was excluded because there were not enough homologous sequences to perform a coevolution analysis. The 76 residue cytosolic domain between TM3 and TM4 was included in the structural modeling, but was removed during clustering and analysis, since it did not converge to a low number of structures. The eight transmembrane domains encode a core structure comprised of TMs 2, 4, 5, and 7 with additional transmembrane domains (TMs 1, 3, 6 and 8) peripheral to this core structure. Mechanistically, the hZIP4 model encodes a central transition metal coordination site similar to the YiiP crystal structure (Figure 27). Mutagenesis of residues within the YiiP metal coordination site alters the transition metal specificity of YiiP¹⁴². Among ZIP member proteins, residues which comprise this putative metal coordination site are variable and amino acid differences within this coordination site likely contribute to a differing cation specificity among ZIP transporters¹⁴³. An unresolved question is elucidating the permeation pathway or pathways which comprise the nM and μ M K_m 's. Inspection

Figure 27. Comparison of hZIP4 with YIIP. A) Expanded view of putative YiiP and hZIP4 transition metal coordination sites. B) Weblogo showing the conservation at each position.



of our experimental results demonstrate that alanine replacement of residues H379, H507 and H536, residues which form a cation coordination site similar to the zinc exporter YiiP, significantly alters the nM K_m at each residue (Tables 5 and 6). In addition, alanine replacement of H624, which is located at a potential exit-point for transition metals is also significantly changed in the nM K_m . Therefore, our *in situ* data supports the conclusion that the nM permeation pathway is comprised, at least in part, of the transmembrane domains which comprise the pore structure of hZIP4. In contrast, the μ M K_m is altered or abolished upon alanine replacement residues H379, H550 and H624. Residues H550 and H624 are located in close proximity at the exit of the putative pore, on the intracellular side of hZIP4, while H379 is located at the top of the pore and within the putative coordination site.

The results of our computational modeling also suggested that the model structure of the hZIP4 protein could satisfy the predicted contacts and retain membrane-like topologies (Figure 23) in multiple oligomeric states. In our proposed oligomeric structure of the hZIP4 protein, the interface for each dimer model is comprised of TMs 3, 4, 7 and 8. It is important to note that while our approach can define residue pairs which are co-evolving, co-evolution between residues does not always mean contact for all conformational states of the protein. Some contacts may only be made in one conformational state, while other contacts may comprise higher order oligomeric assemblies. Furthermore, models with a z-score greater than or equal to two were selected for the clustering analysis (Figure 16). Published experimental support for the dimeric model is derived from two sets of experiments. First, direct analysis of size exclusion HPLC suggested that the oligomeric state of ZIPB in detergent micelles was consistent with a dimer¹⁴⁴. More recently, it was observed that hZIP13 is dimeric following chemical cross-linking⁵⁷. Analysis of our tryptophan scanning mutagenesis experiments suggests that dimer formation can be disrupted upon mutagenesis along TM7.

Analysis of TM scoring demonstrates that the hZIP4 dimer model retains the same fold as MFS proteins. The closest MFS homolog is the twelve transmembrane monomeric eukaryotic phosphate transporter, PiPT¹⁴⁰. Recently, it has been proposed that MFS transporters evolved either from three TM unit rearrangements or a common ancestor without three TM unit rearrangements¹⁴⁵⁻¹⁴⁸. While analysis of our data provides further insight into the evolutionary relationship between SLC proteins, it is important to note that there are caveats to this analysis. First, analysis of our modeling experiments identified four possible dimeric interfaces. Some of the lower scoring models have slightly lower TM-scores when compared with the PiPT transporter. If the lower scoring models prove to be more accurate, then the comparison between the PiPT structure and the hZIP4 model should be re-analyzed. Second, the transport pathway for PiPT is along the homologous dimer interface of the hZIP4 model. This could suggest a different mechanism of transport for these two families of transporters. Alternatively, it could also be true that the proposed three TM unit rearrangements described above resulted in proteins with new functionalities which is exhibited in hZIP4.

In summary, by employing Rosetta with co-evolution and membrane terms in tandem with functional experiments, we have developed the first molecular model for ZIP proteins. This model can be used to examine the location of residues which contribute to specificity (H379, H507, H536 and H624) as well as the velocity of metal transport (H379, H607, H536, H540 and H624). We expect that this model will open new avenues and experimental approaches to identify more nuanced mechanistic questions such as residues which contribute to transition metal docking within the ZIP family of proteins.

4. The large intracellular loop of hZIP4 is an intrinsically disordered zinc binding domain

Note: I thank Dr. Timothy L. Stemmler and Stephen P. Dzul for X-ray absorption spectroscopy experiments and results. I thank Dr. Elizabeth M. Bafaro for her help with atomic absorption spectroscopy. I thank Tuong-Vi Nguyen and Brian Doyon for their contribution during various stages of project development.

4.1 Introduction

The total zinc cellular concentration is in the micromolar range⁷. However, the free cytosolic zinc concentration in eukaryotic cells is in the picomolar range^{7, 11}, while the zinc concentration within zinc storage granules can be as high as millimolar concentration¹². To control the zinc concentration in various cellular compartments, cells have evolved to have highly specialized systems. The metallothionein and zinc transporter proteins are the most important protein families, which regulate zinc concentrations within various cellular compartments. Metallothionein proteins and their zinc-binding properties have been studied in great detail³², however such information regarding the zinc transport proteins remains elusive.

In the previous chapter, we took advantage of co-evolution data and the Rosetta algorithm to predict the hZIP4 membrane domain structure. Our functional studies of mutant hZIP4 proteins using *X.laevis* eggs was also in agreement with the predicted hZIP4 model structure. However, we could not converge the cytosolic loop M3M4 into a small number of structures, and therefore the M3M4 domain was excluded from the clustering and structural analysis. In this study, we used bioinformatics analysis and experimental evidence to show that the M3M4 protein domain is a disordered region of the hZIP4 protein. Recently, intrinsically disordered proteins (IDPs) and intrinsically disordered protein regions (IDPRs) have become recognized as having important biological functions in cell signaling, regulation and control, although they lack secondary and tertiary structural elements¹⁴⁹. IDPRs are estimated to be present in over 35% of human proteins¹⁵⁰. In the case of membrane proteins, a survey of the Protein Data Bank identified disordered regions, as determined by missing electron density in crystal structures, in more than half of deposited membrane protein structures¹⁵¹. Moreover, an analysis of human plasma membrane proteins found that over 40% contained disordered regions of more than 30 amino acids in length, and these disordered regions were three times more likely to occur on the cytoplasmic side than on the extracellular side of the membrane¹⁵². Inside cells, IDPs and IDPRs participate in molecular

recognition functions by binding to target molecules such as nucleic acid, proteins or small ligands¹⁵³. Among their molecular recognition functions, IDPs and IDPRs act as scavengers for ions or small molecules and provide display sites for post-translational modifications such as phosphorylation and ubiquitination¹⁵³.

Functional studies have shown that the zinc transport proteins regulate cytosolic zinc concentrations by importing or exporting zinc to and from cellular compartments¹⁵⁴. Cells also regulate cytosolic zinc concentrations by altering the expression levels of zinc transport proteins. For example, the expression of zinc exporting proteins such as ZnT1, ZnT2, ZnT4, ZnT5 and ZnT6 have been observed to be down-regulated under a zinc deficient diet, whereas the diet supplemented with an excess of zinc resulted in up-regulation of ZnT protein expression¹⁵⁴. In conjunction with the up-regulation of ZnT proteins, an excess of dietary zinc was shown to down-regulate the zinc importer ZIP3 protein expression¹⁵⁴. Similarly, ZIP4 and ZIP10 proteins are down-regulated in zinc replete conditions¹⁵⁴. More detailed studies on the hZIP4 protein has revealed that at high cytosolic Zn²⁺ concentrations, ZIP4 undergoes Zn²⁺-dependent endocytosis, thereby reducing ZIP4 levels in the plasma membrane⁹⁷. At even higher zinc concentrations, hZIP4 is ubiquitinated, presumably at a highly conserved lysine residue within a large intracellular loop between transmembrane domains III and IV (M3M4) and is further subjected to proteasomal degradation⁹⁶. Furthermore, zinc dependent ubiquitination and degradation requires the presence of a histidine-rich domain located on the large cytosolic loop. Taken together, these observations led to the hypothesis that the M3M4 domain acts as a zinc sensor to regulate hZIP4 expression in the plasma membrane⁹⁶. In this study, we describe the metal binding properties of the significant intracellular loop located between transmembrane domains III and IV (M3M4) of hZIP4. We provide the first direct evidence that this domain coordinates two Zn²⁺ ions. Moreover, Zn²⁺ coordination occurs in a sequential manner with the first Zn²⁺ binding with nanomolar affinity to a CysHis₃ site and the second Zn²⁺ binding

with a lower affinity to a His₄ site. Finally, we show that the intracellular M3M4 loop is an intrinsically disordered region.

4.2 Materials and Methods

4.2.1 Materials

D-Desthiobiotin and *Strep*-Tactin Superflow resin were purchased from IBA Life Sciences. Zinc chloride, isopropyl- β -D-thiogalactopyranoside (IPTG), ethylenediaminetetraacetic acid (EDTA), ethylene glycol tetraacetic acid (EGTA) and N-ethylmaleimide (NEM) were purchased from Sigma-Aldrich. Glycerol, tris(2-chloroethyl) phosphate (TCEP), 4-(2-Hydroxyethyl)piperazine-1-ethanesulfonic acid (HEPES), diethyl pyrocarbonate (DEPC), and *N,N'*-dicyclohexyl carbodiimide (DCCD) were purchased from Amresco. 4-morpholinepropanesulfonic acid (MOPS) was purchased from BDH Chemicals.

4.2.2 Bioinformatics

Disorder predictions were performed using FoldIndex (<http://bip.weizmann.ac.il/fldbin/findex>)¹⁵⁵. The FoldIndex is an algorithm that predicts whether the given protein sequence is disordered based on the average hydrophobicity of the residues and net charge of the sequence¹⁵⁵.

4.2.3 Molecular cloning

The gene sequence corresponding to the predicted intracellular domain (M3M4) between residues 424 and 498 of the hZIP4 protein was amplified by PCR from the hZIP4 gene. The resulting PCR product was cloned into the overexpression vector pPR-IBA1 (IBA Life Sciences) to generate pPRIBA-M3M4 using the unique restrictions sites *KpnI* and *NcoI*. The pPR-IBA1 vector introduced a C-terminal Strep tag for affinity purification. Site-directed mutagenesis to generate single cysteine or histidine mutant proteins was performed according to the manufacturer's instructions (Agilent Technologies). Gene synthesis (GenScript) was used to generate triple mutants. All plasmid constructs were verified by DNA sequencing.

4.2.4 Protein expression, purification and labeling

The pPRIBA-M3M4 plasmid was transformed into *E. coli* BL21(DE3) pLysS cells carrying the pSJS1240 plasmid coding for rare tRNAs¹⁵⁶. Transformed *E. coli* cells were grown at 37° C in TB medium (0.012% (w/v) trypton, 0.024% (w/v) yeast extract, 0.004% (v/v) glycerol, 1.7M potassium dihydrogen phosphate and 0.72M potassium hydrogen phosphate) containing 100 µg/ml ampicillin, 34 µg/ml chloramphenicol and 50 µg/ml spectinomycin. Protein expression was induced by adding 100 µM IPTG to a culture of OD₆₀₀ 0.6-0.8, and expression was carried out at 18° C for 20 hours. The cells were harvested and washed with wash buffer (20 mM HEPES, 150 mM NaCl, pH 8). The protein was purified using a boiling lysis method previously reported for the purification of IDPs^{157, 158}. The cell pellet from a 1 L culture was resuspended in 20 ml wash buffer containing 2 mM EDTA and 1 mM dithiothreitol. The cells were lysed by boiling for 20 minutes, followed by incubation in an ice-salt bath for 5 min. All remaining purification steps were performed at 4° C. The lysed cells were sonicated for 30 s to shear the DNA and the cell lysate was clarified by ultracentrifugation for 30 minutes at 100,000 x g. The resulting soluble fraction was loaded onto a *Strep*-Tactin Superflow (IBA Life Sciences) gravity column. The column was washed first with wash buffer containing 0.2 mM EDTA and 0.1 mM TCEP, followed by buffer exchange with chelex-100 treated elution buffer (20 mM HEPES, 150 mM NaCl, 20% (v/v) glycerol, 0.1 mM TCEP, pH 7). The protein was eluted in chelex-100 treated elution buffer containing 2.5 mM D-desthiobiotin. Protein was quantified using the Reducing Agent Compatible Pierce™ Microplate BCA Protein Assay Kit (Thermo Scientific Co.). For labeling, the purified protein was incubated with 0.5 mM DCCD, 10 mM DEPC, or 1 mM NEM for 30 minutes at 4° C followed by extensive dialysis against chelex-100 treated elution buffer.

4.2.5 Circular dichroism spectroscopy

All CD spectra were recorded using a Jasco J-1500 CD spectrometer in 1-mm quartz cuvettes. Protein samples were prepared in 20 mM TRIS (pH 7), 20% (v/v) glycerol and 1 mM TCEP.

Sample and baseline spectra were acquired at 5° C using 20 consecutive scans collected in 0.5 nm increments with a 1-nm bandwidth, a scanning speed of 50 nm/min, and a 4 s data integration time. The temperature dependence of the CD signal was measured between 5 and 90° C at 5° C intervals. Samples were heated at a rate of 2° C/min before three scans were recorded at each temperature. The spectra were averaged, baseline-corrected and smoothed using a Savitzky-Golay filter in the Spectra Manager software (Jasco).

4.2.6 Binding affinity (K_d) determination of M3M4

The Zn^{2+} stock solution was prepared in chelex-100 treated elution buffer and the concentration of Zn^{2+} was quantified using a terpyridine- Zn^{2+} titration¹⁵⁹. The dissociation constant (K_d) for Zn^{2+} to FluoZin-3 was calculated as per the manufacturer's instructions (Invitrogen). Briefly, 1.1 mM EGTA and 1.1 mM Zn^{2+} solutions were mixed to yield free Zn^{2+} concentrations from 0 to 100 nM, and these Zn^{2+} solutions were incubated with 1 μ M FluoZin-3 in black 96-well plates (Thermo Scientific). Fluorescence was recorded on a Perkin Elmer VICTOR 1420 multilabel counter using a 485/14 excitation filter and a 535/25 emission filter. For competition assays with the purified M3M4 proteins, 1 μ M FluoZin-3 and 1 μ M Zn^{2+} were incubated with varying concentrations of M3M4 protein, and the fluorescence was measured. The Zn^{2+} dissociation constant for M3M4 was determined by fitting the curve to equation described below using GraphPad.

$$IC50 = Kd(M3M4) \left[1 + \frac{[FluoZin-3]}{Kd(FluoZin-3)} \right]$$

where IC50 is the concentration of M3M4 required to reduce the maximum fluorescence by 50%, [FluoZin-3] is the concentration of FluoZin-3, and $K_d(FluoZin-3)$ is the experimentally determined Zn^{2+} dissociation constant for FluoZin-3. To fit the binding curves using GraphPad, the fluorescence was normalized, and the curves were fit by constraining the minimum and maximum normalized fluorescence values. The minimum fluorescence was obtained in the absence of zinc and maximum fluorescence was obtained in the absence of protein.

4.2.7 Atomic absorption spectroscopy

Atomic absorption spectroscopy experiments were conducted by Dr. Elizabeth Bafaro. The purified M3M4 protein in elution buffer with an additional 1 mM TCEP was incubated with 4 molar equivalents of Zn^{2+} overnight at 4° C. Excess Zn^{2+} was removed by washing with chelex-100 treated 20 mM Hepes, 20% (v/v) glycerol, 1 mM TCEP, pH 7 using 3 kDa molecular weight cut-off centricons (Millipore). The protein samples were diluted in 10% (v/v) nitric acid (trace metal-free) for AAS analysis. Zn^{2+} was quantified by graphite furnace atomic absorption spectroscopy (Perkin Elmer PiNNAcle 900Z). Metal contents reported are the averages of at least three independent experiments. The metal content of proteins before Zn^{2+} addition was less than 0.1 moles Zn^{2+} per mole protein.

4.2.8 X-ray absorption spectroscopy

X-ray absorption spectroscopy was conducted by Tim Stemamler's laboratory. M3M4 samples were prepared at final concentrations of 1 mM Zn^{2+} in 20 mM HEPES and 30% glycerol at pH 7.0. Samples were loaded into Lucite XAS sample cells wrapped with Kapton tape. After loading, samples were flash frozen and stored in liquid N_2 until data collection. XAS data were collected at the National Synchrotron Light Source (NSLS), on beamline X3-b. Beamline X3-b utilized a Si[111] single crystal monochromator equipped with a Ni plated harmonic rejection/focusing mirror. During data collection, samples were maintained at 24° K using a He Displex Cryostat. Protein fluorescence excitation spectra were collected using a 31-element Ge solid-state detector, with a 0.6 μ M Cu fluorescence filter placed between the cryostat and detector. XAS spectra were measured in 5 eV increments in the pre-edge region (9600-9660 eV), 0.25 eV increments in the edge region (9,660-9740 eV) and 0.05 \AA^{-1} increments in the extended X-ray absorption fine structure (EXAFS) region (to $k = 14 \text{\AA}^{-1}$), integrating from 1s to 25s in a k3 weighted manner for a total scan length of approximately 50 minutes. X-ray energies were individually calibrated by

collecting Zn-foil absorption spectra simultaneously with the protein data. The first inflection point of the Zn-foil spectrum was assigned to 9,668 eV. Each fluorescence channel of each scan was examined for spectral anomalies, and data represent the average of 11 to 14 scans for each sample.

XAS data were processed using the Macintosh OS X version of the EXAFSPAK program suite¹⁶⁰ integrated with the Feff v8 software package for theoretical model generation¹⁶¹. Data reduction utilized a Gaussian function in the pre-edge region and a three-region cubic spline throughout the EXAFS region. Data were converted to k-space using a Zn E0 value of 9,668 eV. The k cubed weighted EXAFS was truncated at 1.0 and 13.5 Å⁻¹ for filtering purposes. This k range corresponds to a spectral resolution of ca. 0.115 Å for all zinc-ligand interactions; therefore only independent scattering environments outside 0.115 Å were considered resolvable in the EXAFS fitting analysis¹⁶². EXAFS fitting analysis was performed on raw/unfiltered data. EXAFS data were fit using both single and multiple scattering amplitude and phase functions calculated with the program Feff v8. Single scattering theoretical models were calculated for carbon, nitrogen, oxygen, and sulfur coordination to simulate zinc nearest-neighbor ligand environments. Scale factors (Sc) and E0 values used during the simulations were calibrated by fitting crystallographically characterized Zn models; specific values include a Scale Factor of 0.9, and E0 values for O, N, C and S of -15.54 eV were used in these simulations⁶⁹. Criteria for judging the best-fit simulation utilized both the lowest mean square deviation between data and fit (F'), corrected for the number of degrees of freedom and a reasonable Debye-Waller factor^{163, 164}.

4.3 Results

4.3.1 The intracellular loop of hZIP4 is disordered

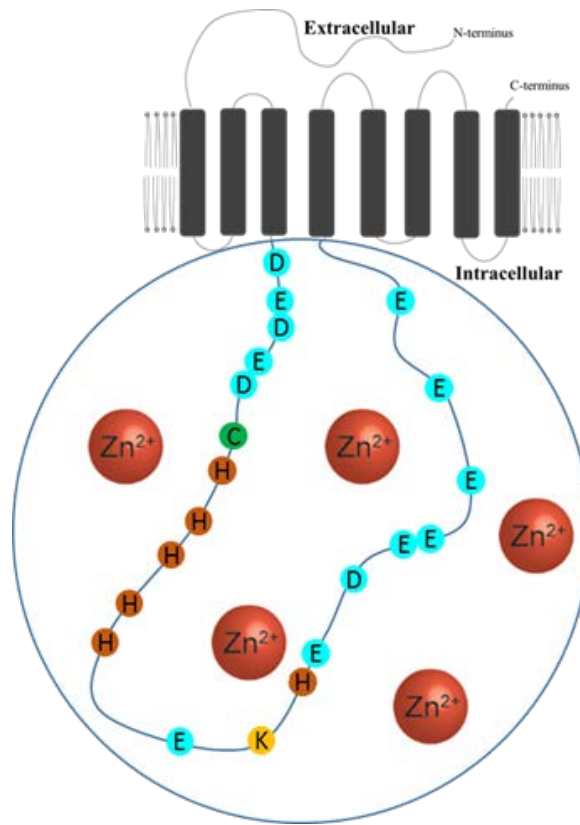
The hZIP4 protein (Figure 28A) was analyzed using the disorder predictor FoldIndex¹⁵⁵. The FoldIndex algorithm predicted that the majority of the hZIP4 protein is folded with the exception of the intracellular M3M4 loop (Figure 28B).

In support of the prediction, the amino acid sequence of the intracellular M3M4 domain contains a low proportion (17%) of order-promoting amino acids (W, C, F, I, Y, V, L, N) and a high proportion (64%) of disorder-promoting residues (A, R, G, Q, S, P, E, K)¹⁶⁵. To investigate the structural and functional properties of the large intracellular loop of hZIP4, we expressed the intracellular domain (residues 424-498 of the full-length hZIP4) fused to a Strep-tag in *E. coli* and purified the protein using a heat-cooling extraction method shown to improve the yield and purity for intrinsically disordered proteins^{157, 158}. Following affinity purification, yields of 1 mg protein L⁻¹ culture were obtained. N-terminal protein sequencing confirmed the identity of the purified protein as the M3M4 domain (data not shown). The purified protein had a slower than predicted mobility on SDS-PAGE, migrating at an apparent molecular mass of 16 kDa (Figure 29), which is 1.4 times higher than the molecular mass calculated from the amino acid sequence (11.4 kDa). Slower mobilities in SDS-PAGE have been observed for IDPs, which bind less SDS than globular proteins due to their unique amino acid compositions¹⁶⁵.

The disordered nature of the M3M4 domain was supported by far-UV circular dichroism (CD) spectroscopy. The CD spectrum (Figure 30) of the M3M4 domain showed a negative minimum at 203 nm, indicative of a random coil structure, and a weak negative shoulder at 220 nm, which may indicate a small degree of α -helical structure. Upon increasing the temperature from 5° C to 85° C, the CD spectra showed an isodichroic point at 208 nm (Figure 30B) which indicates that the M3M4 protein undergoes small temperature-induced conformational change. In general, the

Figure 28. The hZIP4 domain structure and predicted regions of disorder. (A) Schematic of the hZIP4 transporter with the sequence of the large cytosolic loop M3M4 shown. Histidine residues are colored red, cysteine is colored green, acidic residues are colored blue, and the lysine residue is yellow. (B) FoldIndex prediction of disordered regions within the hZIP4 protein. Amino acid residues with a negative FoldIndex score (colored red) are considered as disordered while those with positive scores (colored green) are considered to be in ordered regions.

A



B

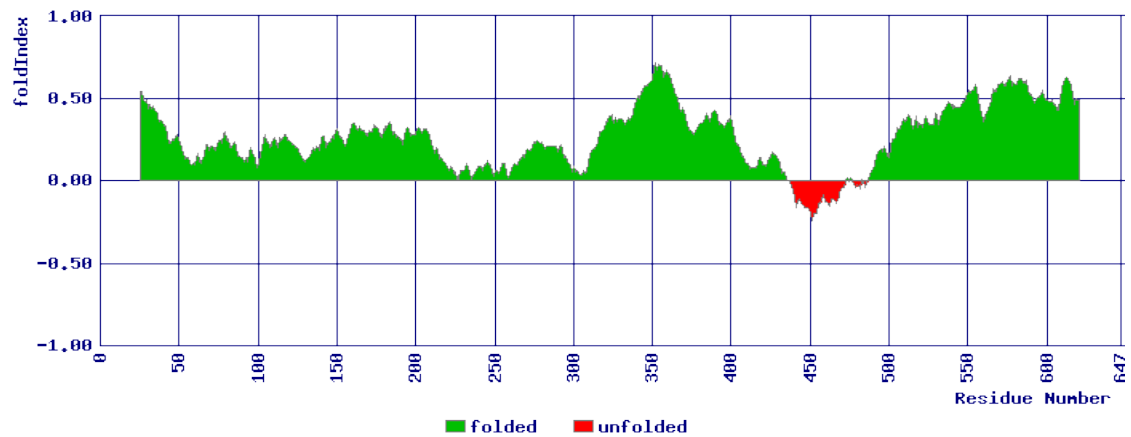


Figure 29. Purification of the recombinantly expressed M3M4 domain using the heat-cooling extraction method. Coomassie Blue stained SDS-PAGE gel of the purification fractions with molecular weight markers (M) indicated. After cell lysis using the heat-cooling extraction method, the cell lysate supernatant (LS) was applied to a *Strep*-Tactin column and the flow-through (FT) was collected. The column was washed with buffer (20 mM Hepes pH 8, 150 mM NaCl (W1) and 20 mM Hepes pH 8, 20% glycerol (W2)), and the protein was eluted in buffer containing desthiobiotin (E)

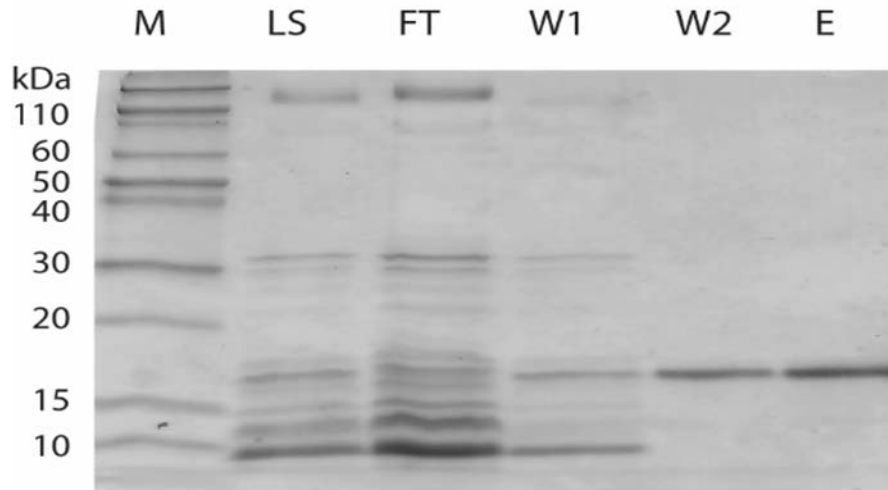
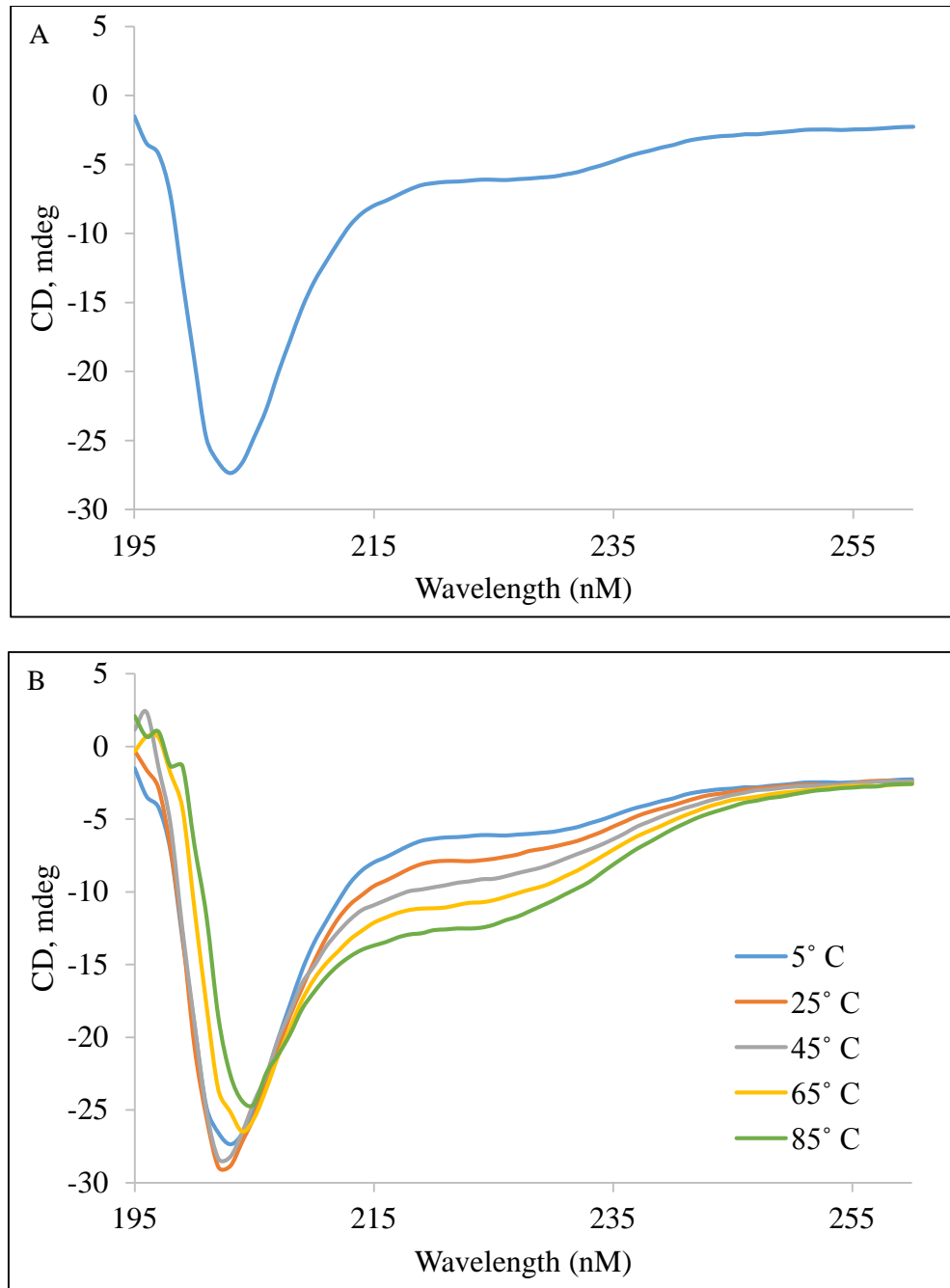


Figure 30. CD spectra of the purified M3M4 domain. The CD spectra was collected in 20 mM TRIS, pH 7 and 20 % (v/v) glycerol at (A) 5°C and (B) at increasing temperatures from 5° C to 85° C. Representative curves at 5° C (blue), 25° C (orange), 45° C (grey), 65° C (yellow) and 85° C (green) are shown.



CD data support the structural predictions that the intracellular M3M4 loop of hZIP4 is an intrinsically disordered region.

4.3.2 The intracellular M3M4 domain binds Zn²⁺ with nanomolar affinity

The number of Zn²⁺ ions that bind to the M3M4 domain was quantified by atomic absorption spectroscopy (AAS). For the AAS analysis, purified M3M4 protein was incubated with a four-fold molar excess of Zn²⁺ and loosely bound Zn²⁺ was removed by washing with buffer. As measured by AAS, the M3M4 domain binds Zn²⁺ with a stoichiometry of 2.2 ± 0.2 Zn²⁺ ions per protein molecule, demonstrating the presence of two binding sites for Zn²⁺ within the intracellular loop.

To investigate the binding affinity of the M3M4 domain for Zn²⁺, FluoZin-3 was used as a Zn²⁺ chelator in competition assays with the protein¹⁶⁶. FluoZin-3 shows an increase in fluorescence upon binding Zn²⁺ with a 1:1 stoichiometry. The dissociation constant of FluoZin-3 ($K_{d\text{fluoZin}}$) for Zn²⁺ was determined to be 21 ± 5 nM under our experimental conditions. The dissociation constant of FluoZin-3 for Zn²⁺ was determined individually for each experimental data set, and this value was used to fit the binding data within the same set of competition experiments. The M3M4 dissociation constant for Zn²⁺ was measured using a competition experiment with FluoZin-3 as described previously¹⁶⁶. In the competition experiments, equimolar amounts of FluoZin-3 and Zn²⁺ were titrated with purified M3M4 protein. The resulting competition data for the wild-type M3M4 domain (Fig. 31A) were fit using one- and two-site binding models. Error analysis of the two models indicated that the one-site model provided the best fit for the data despite the measured 2:1 Zn²⁺:protein stoichiometry observed for the M3M4 protein domain. This suggests either that the two Zn²⁺ ions bind to the M3M4 domain with similar affinities, which cannot be distinguished using the competition assay, or that the second Zn²⁺ ion binds to the protein with a much weaker binding affinity, which cannot be measured using the current assay method. Unfortunately, our attempts to measure a weaker Zn²⁺ binding affinity using a fluorescent indicator (Newport Green)

with a micromolar dissociation constant for Zn^{2+} were unsuccessful due to the tendency of the protein to aggregate at high Zn^{2+} concentrations as determined by dynamic light scattering experiments (data not shown). Thus, the intracellular M3M4 domain of the hZIP4 transporter binds at least one Zn^{2+} ion according to a one-site binding model with a macroscopic dissociation constant of 6 ± 1 nM (Fig. 31A).

4.3.3 Histidine and cysteine residues are involved in Zn^{2+} binding in the M3M4 domain

Cysteine, histidine, and the acidic residues aspartate and glutamate most commonly coordinate Zn^{2+} ¹⁰. The M3M4 domain contains one cysteine, six histidine and 13 acidic residues (Fig. 28A). In order to determine the contributions of these residues in Zn^{2+} binding, the M3M4 protein was treated with N-ethylmaleimide (NEM), diethyl pyrocarbonate (DEPC), and *N,N'*-dicyclohexyl carbodiimide (DCCD), which selectively labels cysteine, histidine, and aspartate and glutamate residues, respectively. Following labeling, the Zn^{2+} binding stoichiometry and dissociation constants were measured. The results (Table 7) indicate that labeling the acidic residues with DCCD did not affect either the Zn^{2+} :protein binding stoichiometry or the dissociation constant compared to the wild-type protein. However, labeling the protein with DEPC resulted in a complete loss of Zn^{2+} binding to the M3M4 protein as measured by AAS (Table 7). Consistent with this result, the dissociation constant for the DEPC-labeled protein could not be measured using the FluoZin-3 competition assay (Fig. 31B). A slight decrease in fluorescence signal was observed in the competition assay at high concentrations of the DEPC-treated M3M4 protein, which we postulate is the result of nonspecific interactions between the free Zn^{2+} and the protein. Finally, labeling the single cysteine residue in the M3M4 domain by treatment with NEM lowered the protein's binding affinity for Zn^{2+} such that the dissociation constant could not be measured using the competition assay (Fig. 31C), although the NEM-treated protein was still able

Figure 31. Normalized competitive binding curves for the determination of Zn^{2+} dissociation constants to the wild-type, labeled and mutant M3M4 proteins. The fluorescence emitted in the presence of various concentrations of M3M4 was normalized to F_{max} (the fluorescence of $1 \mu M$ Zn^{2+} and $1 \mu M$ FluoZin-3) and dissociation constants were determined using a one-site binding model (Equation 1). (A) Fluorescence inhibition curve for wild-type M3M4 protein. Representative fluorescence inhibition curves comparing wild-type (circles) and (B) DEPC treated wild-type protein (squares), (C) NEM treated wild-type protein (squares), (D) H438A mutant protein (squares), (E) H441A mutant protein (squares), (F) C436A (squares), (G) C436A/H438A/H441A triple mutant protein (squares), and (H) H443A/H446A/H448A triple mutant protein (squares). Data are the average of the assay done in triplicate for one protein preparation. Three independent protein preparations gave equivalent results. Error bars represent \pm one standard deviation.

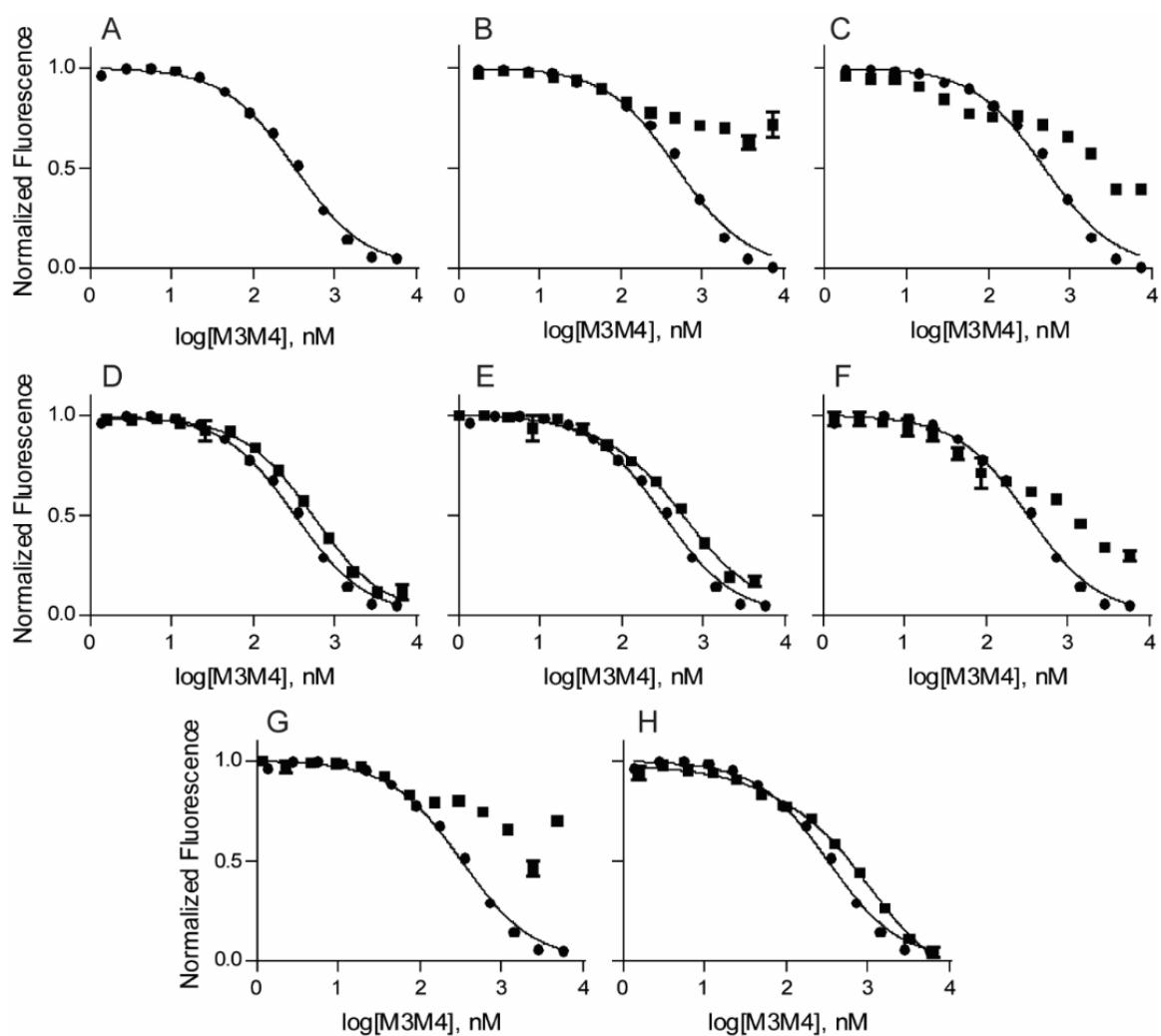


Table 7. Zn(II) binding stoichiometry and dissociation constants for M3M4

Protein	Zinc:protein stoichiometry	K_D (nM)
Labeling reagent		
Unlabeled	2.2 ± 0.2	5 ± 1 (n=3)
DCCD	2.3 ± 0.2	6 ± 1 (n=3)
DEPC	0.3 ± 0.1	No binding (n=3)
N-ethyl maleimide	1.7 ± 0.3	N.D. (n=3)
Mutation		
Wild-type	2.2 ± 0.2	6 ± 1 (n=5)
C436A	2.2 ± 0.2	N.D. (n=3)
H438A	2.1 ± 0.1	8 ± 1 (n=3)
H441A	2.0 ± 0.3	9 ± 2 (n=3)
H443A	2.4 ± 0.2	7 ± 1 (n=3)
H446A	2.4 ± 0.2	6 ± 2 (n=3)
H448A	2.4 ± 0.4	6 ± 2 (n=3)
H466A	2.7 ± 0.2	5.6 ± 0.2 (n=3)
C436A/H438A/H441A	1.3 ± 0.2	N.D. (n=3)
H443A/H446A/H448A	1.1 ± 0.2	12 ± 2 (n=3)

N.D. – Weaker binding. The dissociation constant could not be determined using the competition assay. Bold-faced are significantly different from wild-type.

to bind $1.7 \pm 0.3 \text{ Zn}^{2+}$ per protein molecule when treated with an excess of Zn^{2+} (Table 7). Based on the labeling data, we conclude that the histidine and cysteine residues, but not aspartate or glutamate residues, coordinate Zn^{2+} in the intracellular M3M4 loop of hZIP4.

To further investigate the role of the histidine and cysteine residues in Zn^{2+} coordination by M3M4, we individually mutated the six histidine and one cysteine residues to alanine. All single mutants retained the ability to bind two Zn^{2+} ions per molecule protein (Table 7). Interestingly, the H466A mutant protein was able to bind significantly higher amounts of Zn^{2+} . Competition assays with FluoZin-3 were performed. As with the wild-type protein, the binding data for the single histidine mutations were best fit to a one-site binding model, and the dissociation constants were calculated (Table 7). The single mutants H443A, H446A, H448A and H466A showed Zn^{2+} binding affinities that were comparable to the wild-type protein, whereas the single mutants H438A and H441A displayed binding affinities that were statistically different (p values < 0.05) from the wild-type protein (Table 7, Figure 31D and E). Although the H438A and H441A mutant proteins exhibited weaker binding affinities compared to the wild-type, the change in dissociation constants was not as dramatic as observed for the DEPC-labeled protein. The inability of any single histidine mutation to produce a marked change in Zn^{2+} binding affinity is likely due to stabilization of the Zn^{2+} ion by the remaining histidines and neighboring residues. Ligand substitution by neighboring residues has also been observed in a Zn^{2+} finger protein¹⁶⁷. In contrast to the histidine mutants, mutation of the single cysteine residue to alanine (C436A) resulted in a protein with a substantially weaker Zn^{2+} binding affinity that could not be measured using the FluoZin-3 competition assay (Figure 31F). Taken together, the single histidine and cysteine mutations in M3M4 indicated that C436, H438, and H441 are important residues contributing to Zn^{2+} binding.

Based on the results of the single mutants, we designed two triple mutants, C436A/H438A/H441A and H443A/H446A/H448A, and analyzed these mutants for Zn^{2+} binding. As expected, both triple

mutant proteins bound only one Zn^{2+} ion per molecule protein (Table 7). Also, the triple mutants showed significantly weaker Zn^{2+} binding affinities when compared to the wild-type domain (Table 7, Figure 31G and H). In the case of the H443A/H446A/H448A triple mutant, the measured dissociation constant was two-fold higher than that of the wild-type protein, whereas the C436A/H438A/H441A triple mutant yielded a substantially weaker dissociation constant that could not be measured using the FluoZin-3 competition assay. These data suggest that C436/H438/H441 and H443/H446/H448 likely form the two coordination sites for Zn^{2+} binding to the intracellular M3M4 domain, with the C436/H438/H441 having a tighter binding affinity for Zn^{2+} . The binding affinity data suggest that Zn^{2+} binds first to the higher affinity C436/H438/H441 site, followed by binding of the second Zn^{2+} to the H443/H446/H448 site.

4.3.4 EXAFS reveals the coordination geometry of Zn^{2+} bound to M3M4 (In collaboration with Timothy L. Stemmler Lab, Wayne State University)

In order to further elucidate the Zn^{2+} -binding properties of the M3M4 domain, the Zn^{2+} -bound protein was analyzed by X-ray absorption spectroscopy (XAS). The X-ray absorption near edge structure (XANES) portion of an XAS spectrum provides qualitative details regarding metal site structure with ligand details regarding metal site structure with ligand speciation and can be used to compare differences in metal binding sites on related protein samples. XANES spectra of M3M4 prepared with various stoichiometric amounts of Zn^{2+} revealed that the M3M4 protein with 0.5 and 1 molar equivalent of Zn^{2+} yielded similar XANES spectra, whereas the two Zn^{2+} -bound protein produced a distinctly different XANES edge (Figure 32A). These data are consistent with a model in which the two Zn^{2+} ions bind sequentially to the M3M4 domain. Further, simulations of the extended X-ray absorption fine structure (EXAFS) region of the XAS spectrum provide metrical details regarding the metal-ligand coordination environments for a metal in a metalloprotein at extremely high resolution ($\pm 0.02 \text{ \AA}$).¹⁶³ EXAFS spectra for the Zn^{2+} -bound M3M4 proteins, along with the Fourier transforms of the EXAFS data, are given in Figure

33. In each spectrum, the EXAFS at ca. $k = 4 \text{ \AA}^{-1}$ shows a beat pattern characteristic of imidazole scattering from a histidine residue coordinated to the protein-bound metal.^{ENREF_69¹⁶⁸} All spectra could be fit with nearest neighbor scattering constructed predominately with O/N ligands, and, in the case of M3M4 with 0.5 and 1 molar equivalent Zn^{2+} , with an additional sulfur scattering ligand (Table 8). No sulfur ligation was observed in the M3M4 protein with two Zn^{2+} bound, presumably since the sulfur scattering is a low component of the overall ligand scattering signal. Within the error of technique (± 0.5), all Zn^{2+} coordination numbers from the simulations are consistent with Zn^{2+} being tetra-coordinated. Based on the EXAFS analysis, we conclude that the first Zn^{2+} ion binds to a CysHis₃ site and the second Zn^{2+} ion binds to a site comprised solely of histidines. Long range scattering ($R > 2.8 \text{ \AA}$) is observed in the Fourier transforms of the samples, as expected given the suggested presence of imidazole coordination. Long-range scattering interactions could be easily simulated for Zn^{2+} -C/N interactions above $R = 2.8 \text{ \AA}$ using single scattering models, however coordination numbers for the fits were variable and consistent with an overlap between single and multiple scattering contributions at each of the long range bond lengths. Attempts to fit this data with a multiple scattering theoretical model compound for a Zn^{2+} -imidazole interaction were unsuccessful.

XAS was also used to evaluate Zn^{2+} coordination in the triple mutants (C436A/H438A/H441A and H443A/H446A/H448A). XANES spectra of the H443A/H446A/H448A mutant resembled the one Zn^{2+} -bound wild-type protein (Fig. 32B), and EXAFS data (Figure 33G, Table 7) showed the same CysHis₃ coordination geometry as the wild-type protein with a single Zn^{2+} ion bound. The C436A/H438A/H441A mutant protein showed an XANES spectrum intermediate between the one and two Zn^{2+} bound wild-type (Figure 32B), and the EXAFS analysis revealed a ligand

Figure 32. Normalized XANES spectra for wild-type and triple mutant Zn^{2+} -loaded M3M4 samples. (A) XANES spectra of wild-type M3M4 in the presence of 0.5 (gray line), 1 (black line) and 2 (dashed line) equivalents of Zn^{2+} . (B) XANES spectra of C436A/H438A/H441A triple mutant (gray dashed line) and H443A/H446A/H448A triple mutant (gray dashed line) loaded with 1 equivalent Zn^{2+} compared to wild-type M3M4 loaded with 1 (black solid line) or 2 (black dashed line) equivalents of Zn^{2+} .

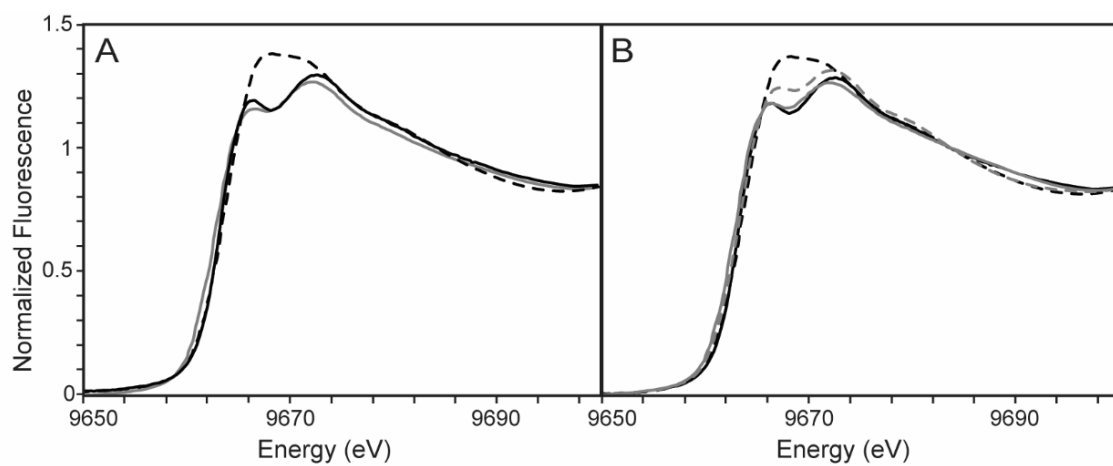


Figure 33. EXAFS and Fourier transform of the EXAFS data for wild-type and mutant Zn²⁺-loaded M3M4 proteins. Comparison of raw data (black) and simulations (green) for both the EXAFS (left) and Fourier transform (right). Wild-type M3M4 with 0.5 equivalents of Zn²⁺ (A, B), wild-type with 1 equivalent of Zn²⁺ (C, D), wild-type with 2 equivalents of Zn²⁺ (E, F), C436A/H438A/H441A triple mutant (G, H), and H443A/H446A/H448A triple mutant (I, J).

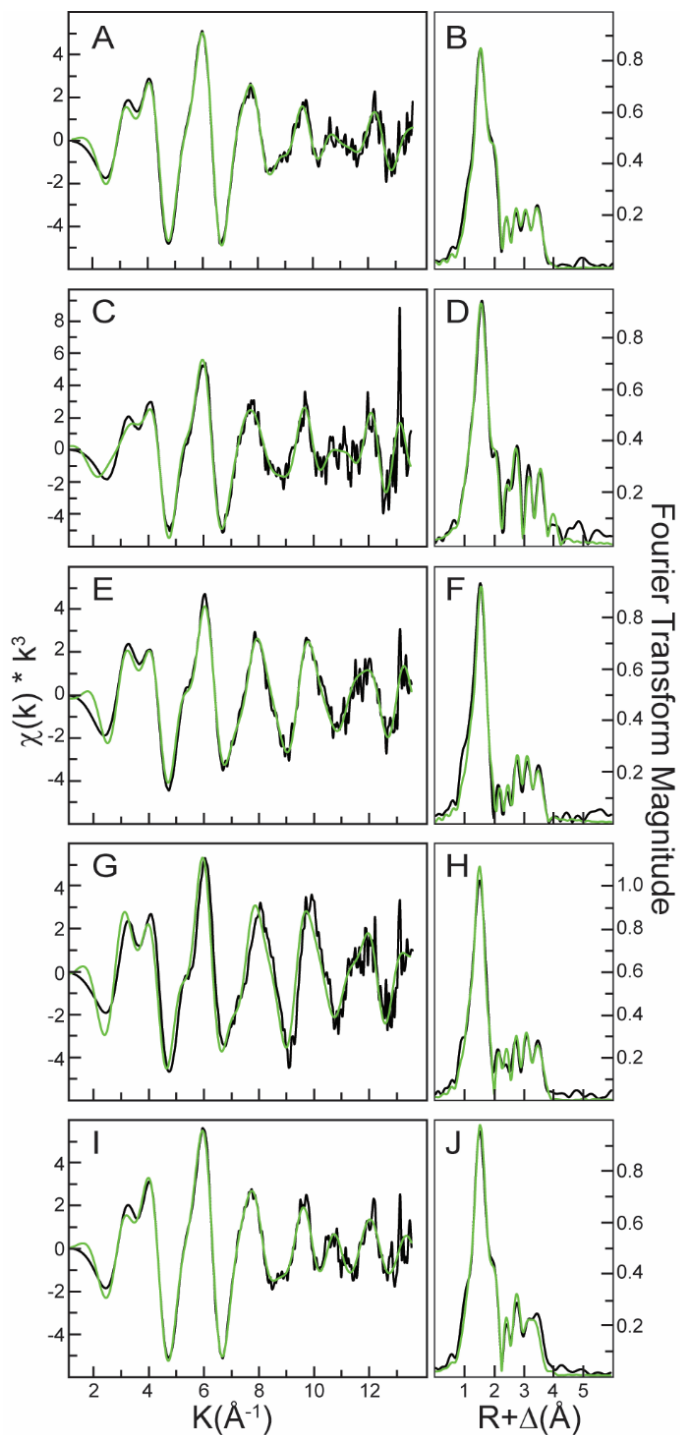


Table 8. EXAFS and Fourier transform of the EXAFS data for wild-type and mutant Zn²⁺-loaded M3M4 proteins. Comparison of raw data (black) and simulations (green) for both the EXAFS (left) and Fourier transform (right). Wild-type M3M4 with 0.5 equivalents of Zn²⁺ (A, B), wild-type with 1 equivalent of Zn²⁺ (C, D), wild-type with 2 equivalents of Zn²⁺ (E, F), C436A/H438A/H441A triple mutant (G, H), and H443A/H446A/H448A triple mutant (I, J).

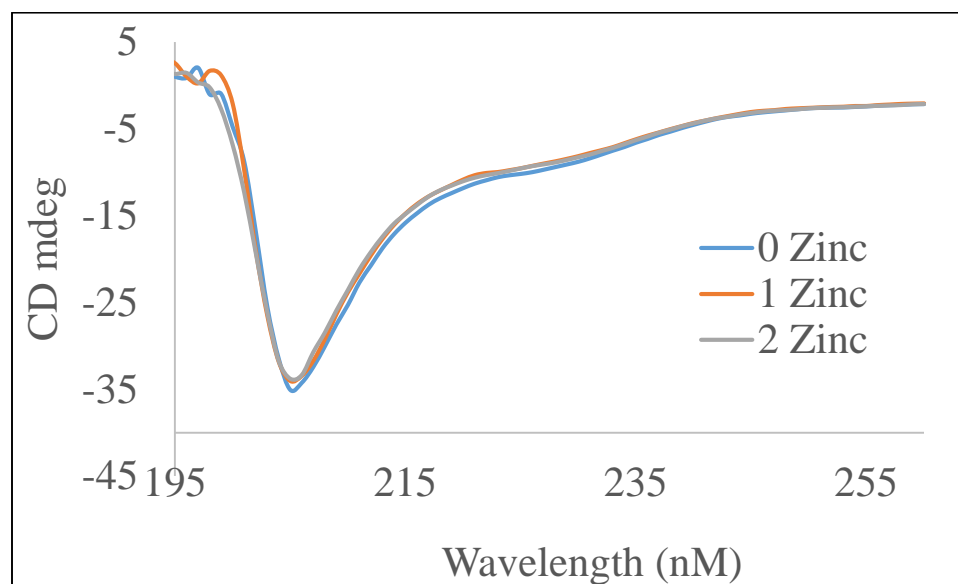
Nearest-Neighbor Ligand Environment ^a						
Sample	Fit ^b	Atom ^c	R(Å) ^d	C.N. ^e	σ ^{2f}	F' ^g
Wild-type + 0.5 Zn ²⁺	1	O/N	2.01	2.5	5.4	1.55
	2	O/N S	1.99 2.28	2.5 1.5	5.1 5.1	0.52
Wild-type + 1 Zn ²⁺	1	O/N	2.01	3.0	4.6	1.90
	2	O/N S	1.99 2.28	3.0 1.0	4.0 4.3	1.41
Wild-type + 2 Zn ²⁺	1	O/N	1.99	3.5	4.8	0.54
C436A/H438A/H441A	1	O/N	1.98	4.0	4.6	0.84
H443A/H446A/H448A	1	O/N	2.01	3.0	5.3	1.62
	2	O/N S	1.99 2.28	3.0 1.5	4.8 5.0	0.71

environment consisting of four histidine residues (Figure 33I, Table 8). Interestingly, addition of a second Zn^{2+} to the wild-type M3M4 protein distorts the average metal binding site away from a simple linear combination of the single loaded independent sites. Taken together, the XAS results are consistent with the model derived from mutagenesis analysis, in which two Zn^{2+} ions bind sequentially to two distinct sites within the M3M4 domain, with the CysHis₃ site comprising the first site and a histidine only site comprising the second site.

4.3.5 Structural changes to the M3M4 domain upon Zn^{2+} binding

Structural changes to the intracellular domain upon Zn^{2+} binding were monitored by CD spectroscopy. Upon sequential addition of Zn^{2+} to M3M4, only minor changes in the CD spectra were observed (Figure 34). Interestingly, the M3M4 protein undergoes a small structural change upon binding the second Zn^{2+} . However, the presence of the large negative peak at 203 nm in all the spectra indicates that the M3M4 protein domain remains largely disordered even in the Zn^{2+} -bound state.

Figure 34. Effect of Zn^{2+} on M3M4 CD spectra. The CD spectra of the M3M4 domain was collected presence of 0 (blue line), 1 (orange line) and 2 (grey line) molar equivalents of Zn^{2+} .

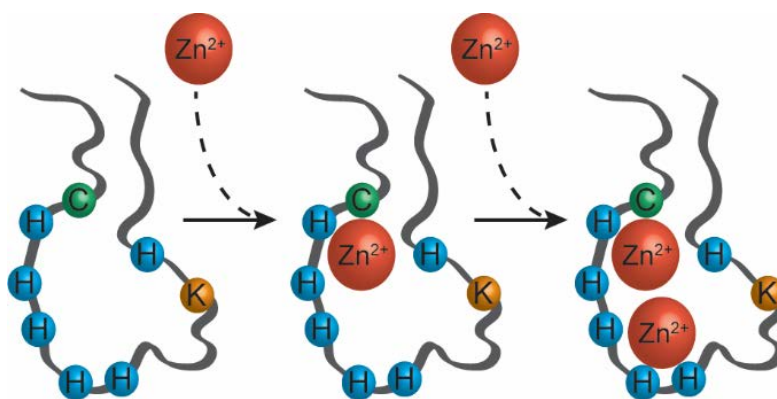


4.4 Discussion

In this study, our data provide the first direct evidence that the histidine-rich domain within the cytoplasmic M3M4 loop of hZIP4 binds two Zn^{2+} ions (Table 7). Moreover, we have shown by using XAS (Figure. 32 and 33) that Zn^{2+} binding occurs sequentially with the first Zn^{2+} binding to a site involving the single cysteine residue and three histidine residues (CysHis₃) followed by a second Zn^{2+} binding event to a site consisting solely of histidine residues (His₄). Based on the results of our mutagenesis analysis (Table 7), our data is consistent with the observation that single alanine replacement of histidine residues within the M3M4 domain does not eliminate zinc-dependent degradation of hZIP4⁹⁶. Equally, from the analysis of this data, we conclude that the CysHis₃ site is comprised of C436, H438 and H441, and the second site (His₄) is likely composed of H443, H446 and H448 and a fourth ligand, which may be H466 (Figure 31). Although mutation of H466 to alanine did not affect the Zn^{2+} binding affinity, the H466A mutant protein consistently bound higher amounts of Zn^{2+} than the wild-type or any of the other single mutants. We, therefore, speculate that mutation of H466, increases the structural flexibility of the protein domain, which may allow more adventitious Zn^{2+} binding to the M3M4 domain (Figure 31A). The fourth histidine ligand for the CysHis₃ site is likely a bridging ligand shared by the two sites. As Zn^{2+} ions are typically found in tetra-coordinated environments¹⁶⁹, binding of two Zn^{2+} ions would require a minimum of seven protein ligands with one ligand serving as a bridge. Bridging ligands have been observed in other Zn^{2+} binding proteins; for example, cysteine is a bridging ligand in metallothionein¹⁷⁰ and histidine serves as a bridging ligand in Cu, Zn superoxide dismutase¹⁷¹. Based on our data, we speculate that one of the histidines in the loop acts as a bridging ligand, but we cannot predict which histidine functions as the bridging ligand.

Using the FluoZin-3 competition assay, we measured a single apparent dissociation constant of 6 ± 1 nM for Zn^{2+} binding to the isolated M3M4 intracellular domain (Table 7, Figure 31A). The measured one-site binding reflects Zn^{2+} binding to the CysHis₃ site as the H443A/H446A/H448A

Figure 35. Proposed model of Zn^{2+} binding to M3M4



triple mutant displayed a binding affinity in the low nanomolar range, whereas a significantly weaker binding affinity binding that could not be measured using the FluoZin-3 indicator was observed for the C436A/H438A/H441A triple mutant. Thus, the first Zn^{2+} binds to the CysHis₃ site with a low nanomolar binding affinity followed by binding of the second Zn^{2+} to the His₄ site with a weaker, likely micromolar or higher, binding affinity. It should be noted that the dissociation constant measured for the purified M3M4 protein may not necessarily reflect the *in vivo* binding affinity of Zn^{2+} for this domain as interactions of the cytoplasmic loop with other regions of the hZIP4 transporter or with the lipid environment may modulate its affinity for Zn^{2+} . Nevertheless, the low nanomolar Zn^{2+} binding affinity of the CysHis₃ site within the M3M4 domain is comparable to other Zn^{2+} -binding proteins whose measured Zn^{2+} dissociation constants range from nanomolar to low picomolar or less¹⁷². The cytoplasmic concentration of free Zn^{2+} in eukaryotic cells is estimated to be in the picomolar to low nanomolar range¹⁷², which suggests that the CysHis₃ site may be occupied with Zn^{2+} under normal physiological conditions. The second, His₄, site would be unoccupied at normal cytosolic free Zn^{2+} concentrations. The His₄ site would become occupied with Zn^{2+} as the local Zn^{2+} concentration near the M3M4 domain is expected to be higher as hZIP4 functions to transport Zn^{2+} across the membrane. Thus, we propose that the His₄ site likely acts as a sensor to detect high cytosolic Zn^{2+} concentrations and control the level of hZIP4 in the plasma membrane accordingly. Only when both sites are occupied will hZIP4 be subjected to zinc-stimulated ubiquitination and degradation⁹⁶.

To investigate the structural basis for Zn^{2+} sensing by the M3M4 loop, a combination of protein structure prediction algorithms and CD spectroscopy were used. The cytoplasmic M3M4 loop of hZIP4 was predicted (Figure 28B) and shown to be intrinsically disordered (Figure 30). It is possible that the M3M4 domain adopts a more defined structure within the holo-hZIP4 protein. However, analysis of the prediction algorithms and our data suggest that M3M4 is mostly disordered. As IDPs and IDPRs tend to undergo disorder-to-order transitions upon binding partner

molecules, we sought to determine if the M3M4 cytosolic loop becomes ordered upon Zn^{2+} binding using CD spectroscopy to assess secondary structure. The M3M4 protein domain remains largely disordered in the Zn^{2+} -bound state (Figure 34). Recently, the occurrence of disorder in the bound state has been found to be a common feature of IDPs^{153, 173}. More than 40 IDPs have been shown to form “fuzzy” complexes upon interaction with their partners¹⁷³. “Fuzziness” is believed to be functionally advantageous, allowing IDPs or IDPRs the flexibility to interact with multiple partners or to undergo a variety of post-translational modifications, such as phosphorylation and ubiquitination^{153,173}. Also, the S490 residue of hZIP4 was identified to be phosphorylated in an analysis of the phosphoproteome of human embryonic stem cells¹⁷⁴. In addition to phosphorylation, hZIP4 was predicted using the UbPred server to undergo ubiquitination at K463 within the intracellular M3M4 loop¹⁷⁵. hZIP4 was shown to be ubiquitinated at high cytosolic Zn^{2+} concentrations and to undergo subsequent proteasomal degradation of the transporter⁹⁶. Taken together with our data on Zn^{2+} binding to the purified cytosolic domain, we propose a model whereby, at high cytosolic Zn^{2+} concentrations, Zn^{2+} binding to the low-affinity His₄ site, combined with an occupied CysHis₃ site, induces structural changes in the M3M4 intracellular loop, which may alter the post-translational modification status of hZIP4. Degradation in the proteasome is enhanced by the presence of a disordered protein region downstream of the ubiquitination site^{96, 176}.

The cytosolic loop of hZIP4 likely fulfills a number of roles, including proper processing and recycling of the transporter and possibly modulating Zn^{2+} transport through changes in post-translational modifications, all of which rely on its disordered state. As disordered regions tend not to be under strong evolutionary conservation¹⁷⁷, it is not surprising that the large cytosolic loop between transmembrane domains III and IV, which is characteristic of the LIV-I subfamily of ZIP transporters, is nonconserved. Among the human LIV-I subfamily members, the amino acid sequence and the number and arrangement of potential Zn^{2+} binding ligands varies. Thus, the cytosolic M3M4 domain likely functions as a protein-specific regulatory domain.

5. Future work

6.1 Define the driving force conditions for hZIP4

Ion transport membrane proteins are largely classified under ion channels, ion pumps and ion transporters¹⁷⁸. Ion channels have a well-defined pore and the selectivity of an ion is largely decided by physical interactions and pore size of the channel¹⁷⁸. To open the pore and transport ions towards the concentration gradient, a small conformational change is required, where the energy requirement for inducing such change is very small¹⁷⁸. The ion pumps require relatively more energy to pump the ions against the concentration gradient, which is derived from ATP hydrolysis¹⁷⁸. The ion transporter has a thermodynamically more complex mechanism of transport. Transporters are highly selective for a distinct ligand and undergo a large conformational change upon binding¹⁷⁸. The large conformational change requires high energetic interactions, which is being provided via ATP hydrolysis or by means of other favorable binding energies¹⁷⁸.

Sequence homology analysis of hZIP4 has revealed that the protein does not have an ATP binding domain. Under these circumstances, the electrochemical gradient could provide energy to facilitate a large conformational change for hZIP4¹⁷⁸. To eliminate the possibility of ion gradient facilitated zinc transport, we have used proton, sodium, potassium and chloride ion gradients. We have also used bicarbonate which has been reported as a co-transporter for hZIP2, hZIP8 and hZIP14. However, it is not clear what the driving force for zinc transport is. Interestingly, when using sodium citrate and sodium acetate to replace chloride, we found significant inhibition of transport activity. We could not rule out any conclusion based on this experiment since both these salts are known to reduce the intracellular pH and have a chelating effect as well. At this point, we cannot deny the possibility of hZIP4 being governed by intracellular conditions. By manipulating intracellular conditions such as changing intracellular salt concentration and pH, we can test the hypothesis of hZIP4 mediated transport in governed by intracellular ion gradients. However, using *X. laevis* oocytes for such experiments is not a viable option because of the stability of oocytes. To address all the challenges associated with hZIP4 driving force, we can express and purify the hZIP4

protein heterologously in *P. pastoris*. Successful reconstitution of the hZIP4 protein into the liposomes would provide us with more flexibility with respect to testing conditions such as salt gradient and pH both inside and outside.

6.2 Oligomeric state of hZIP4

In this study, we have shown that hZIP4 may function as a dimer. Our analysis is based on the effect of reducing agent during sample preparation of an SDS-PAGE gel. The oligomeric state of hZIP4 should be more definitively tested by a more direct approach. One such approach to test for the oligomeric state is with total internal reflection fluorescence microscopy, where hZIP4 is tagged with a fluorescence protein and the photo-bleaching effect is tracked against the time. The photo-bleaching pattern is directly corresponding to the oligomeric state of protein¹⁷⁹. However, one needs to be careful about the results as steric interference may interfere with the formation of dimer. An alternative approach could be cysteine cross-linking experiment¹⁸⁰.

6. References

1. J. Raulin, *Ann. Sci. Nat.*, 1869, 11, 93-99.
2. A. Prasad, *J. Lab. Clin. Med.*, 1963, 61, 537-549.
3. A. S. Prasad, A. R. Schulert, A. Miale, Z. Farid and H. H. Sandstead, *Am. J. Clin. Nutr.*, 1963, 12, 437-444.
4. H. H. Sandstead, A. S. Prasad, A. R. Schulert, Z. Farid, A. Miale, S. Bassilly and W. J. Darby, *Am. J. Clin. Nutr.*, 1967, 20, 422-442.
5. A. S. Prasad, *Am. J. Clin. Nutr.*, 1991, 53, 403-412.
6. G. J. Fosmire, *Am. J. Clin. Nutr.*, 1990, 51, 225-227.
7. W. Maret and A. Krężel, *Mol. Med.*, 2007, 13, 371-375.
8. P. Zalewski, I. Forbes, R. Seamark, R. Borlinghaus, W. Betts, S. Lincoln and A. Ward, *Chem. Biol.*, 1994, 1, 153-161.
9. Y. Li and W. Maret, *Exp. Cell Res.*, 2009, 315, 2463-2470.
10. W. Maret and Y. Li, *Chem. Rev.*, 2009, 109, 4682-4707.
11. R. A. Bozym, R. B. Thompson, A. K. Stoddard and C. A. Fierke, *ACS Chem. Biol.*, 2006, 1, 103-111.
12. M. Foster, R. Leapman, M. Li and I. Atwater, *Biophys. J.*, 1993, 64, 525-532.
13. C. Andreini, L. Banci, I. Bertini and A. Rosato, *J. Proteome Res.*, 2006, 5, 196-201.
14. K. A. McCall, C.-c. Huang and C. A. Fierke, *J. Nutr.*, 2000, 130, 1437S-1446S.
15. B. L. Vallee and D. S. Auld, *Biochemistry*, 1990, 29, 5647-5659.
16. W. N. Lipscomb and N. Sträter, *Chem. Rev.*, 1996, 96, 2375-2434.
17. K. Patel, A. Kumar and S. Durani, *Biochim. Biophys. Acta*, 2007, 1774, 1247-1253.
18. J. M. Matés, C. Pérez-Gómez and I. N. De Castro, *Clin. Biochem.*, 1999, 32, 595-603.
19. L. J. Machlin and A. Bendich, *FASEB J.*, 1987, 1, 441-445.
20. S. R. Powell, *J. Nutr.*, 2000, 130, 1447S-1454S.
21. W. Maret, *J. Nutr.*, 2000, 130, 1455S-1458S.
22. J. C. King, D. M. Shames and L. R. Woodhouse, *J. Nutr.*, 2000, 130, 1360S-1366S.
23. J. P. Liuzzi and R. J. Cousins, *Annu. Rev. Nutr.*, 2004, 24, 151-172.
24. S. Ripa and R. Ripa, *Minerva Med.*, 1994, 86, 37-43.
25. K. H. Brown, S. E. Wuehler and J. M. Peerson, *Food Nutr. Bull.*, 2001, 22, 113-125.
26. M. N. Hughes and R. K. Poole, *Microbiology*, 1991, 137, 725-734.
27. R. J. Cousins, J. P. Liuzzi and L. A. Lichten, *J. Biol. Chem.*, 2006, 281, 24085-24089.
28. S. R. Davis and R. J. Cousins, *J. Nutr.*, 2000, 130, 1085-1088.
29. U. Rana, R. Kothinti, J. Meeusen, N. M. Tabatabai, S. Krezoski and D. H. Petering, *J. Inorg. Biochem.*, 2008, 102, 489-499.
30. W. Maret, *Proc. Natl. Acad. Sci. USA*, 1994, 91, 237-241.
31. H. Shen, H. Qin and J. Guo, *Nutr. Res.*, 2008, 28, 406-413.
32. Y. Li and W. Maret, *J. Anal. At. Spectrom.*, 2008, 23, 1055-1062.
33. C. J. Haney, G. Grass, S. Franke and C. Rensing, *J. Ind. Microbiol. Biotechnol.*, 2005, 32, 215-226.
34. T. Kambe, H. Narita, Y. Yamaguchi-Iwai, J. Hirose, T. Amano, N. Sugiura, R. Sasaki, K. Mori, T. Iwanaga and M. Nagao, *J. Biol. Chem.*, 2002, 277, 19049-19055.
35. T. Fukada and T. Kambe, *Metallomics*, 2011, 3, 662-674.
36. L. A. Gaither and D. J. Eide, in *Zinc Biochemistry, Physiology, and Homeostasis*, Springer, 2001, pp. 65-84.
37. M. Lu and D. Fu, *Science*, 2007, 317, 1746-1748.
38. I. Lasry, Y. Golan, B. Berman, N. Amram, F. Glaser and Y. G. Assaraf, *J. Biol. Chem.*, 2014, 289, 7275-7292.
39. A. Michalczyk, J. Allen, R. Blomeley and M. Ackland, *Biochem. J.*, 2002, 364, 105-113.

40. Y. Chao and D. Fu, *J. Biol. Chem.*, 2004, 279, 12043-12050.
41. E. Ohana, E. Hoch, C. Keasar, T. Kambe, O. Yifrach, M. Hershfinkel and I. Sekler, *J. Biol. Chem.*, 2009, 284, 17677-17686.
42. M. Quadri, A. Federico, T. Zhao, G. J. Breedveld, C. Battisti, C. Delnooz, L.-A. Severijnen, L. D. T. Mammarella, A. Mignarri and L. Monti, *Am. J. Hum. Genet.*, 2012, 90, 467-477.
43. M. L. Guerinot, *Biochim. Biophys. Acta*, 2000, 1465, 190-198.
44. K. M. Taylor and R. I. Nicholson, *Biochim. Biophys. Acta*, 2003, 1611, 16-30.
45. K. Wang, B. Zhou, Y.-M. Kuo, J. Zemansky and J. Gitschier, *Am. J. Hum. Genet.*, 2002, 71, 66-73.
46. W. Chowanadisai, D. M. Graham, C. L. Keen, R. B. Rucker and M. A. Messerli, *Proc. Natl. Acad. Sci. USA*, 2013, 110, 9903-9908.
47. K. Taylor, H. Morgan, A. Johnson, L. Hadley and R. Nicholson, *Biochem. J*, 2003, 375, 51-59.
48. T. P. Dalton, L. He, B. Wang, M. L. Miller, L. Jin, K. F. Stringer, X. Chang, C. S. Baxter and D. W. Nebert, *Proc. Natl. Acad. Sci. USA*, 2005, 102, 3401-3406.
49. N. A. Begum, M. Kobayashi, Y. Moriwaki, M. Matsumoto, K. Toyoshima and T. Seya, *Genomics*, 2002, 80, 630-645.
50. K. Taylor, H. Morgan, A. Johnson and R. Nicholson, *FEBS Lett.*, 2005, 579, 427-432.
51. N. Zhao, J. Gao, C. A. Enns and M. D. Knutson, *J. Biol. Chem.*, 2010, 285, 32141-32150.
52. F. Wang, B.-E. Kim, M. J. Petris and D. J. Eide, *J. Biol. Chem.*, 2004, 279, 51433-51441.
53. B. L. Mihelich, E. A. Khramtsova, N. Arva, A. Vaishnav, D. N. Johnson, A. A. Giangreco, E. Martens-Uzunova, O. Bagasra, A. Kajdacsy-Balla and L. Nonn, *J. Biol. Chem.*, 2011, 286, 44503-44511.
54. N. Kagara, N. Tanaka, S. Noguchi and T. Hirano, *Cancer Sci.*, 2007, 98, 692-697.
55. K. Taylor, H. Morgan, A. Johnson and R. Nicholson, *Biochem. J*, 2004, 377, 131-139.
56. L. Huang, C. P. Kirschke, Y. Zhang and Y. Y. Yu, *J. Biol. Chem.*, 2005, 280, 15456-15463.
57. B.-H. Bin, T. Fukada, T. Hosaka, S. Yamasaki, W. Ohashi, S. Hojyo, T. Miyai, K. Nishida, S. Yokoyama and T. Hirano, *J. Biol. Chem.*, 2011, 286, 40255-40265.
58. B. Milon, D. Dhermy, D. Pountney, M. Bourgeois and C. Beaumont, *FEBS Lett.*, 2001, 507, 241-246.
59. L. A. Gaither and D. J. Eide, *J. Biol. Chem.*, 2001, 276, 22258-22264.
60. M. M. Desouki, J. Geradts, B. Milon, R. B. Franklin and L. C. Costello, *Mol. Cancer*, 2007, 6, 37.
61. L. A. Gaither and D. J. Eide, *J. Biol. Chem.*, 2000, 275, 5560-5564.
62. W. Matsuura, T. Yamazaki, Y. Yamaguchi-Iwai, S. Masuda, M. Nagao, G. K. Andrews and T. Kambe, *Biosci. Biotechnol. Biochem.*, 2009, 73, 1142-1148.
63. D. J. Eide, *Pflügers Archiv*, 2004, 447, 796-800.
64. M.-C. Franz, A. Simonin, S. Graeter, M. A. Hediger and G. Kovacs, *J. Biomol. Screen.*, 2014, 19, 909-916.
65. R. A. Colvin, C. P. Fontaine, D. Thomas, T. Hirano, T. Nagano and K. Kikuchi, *Arch. Biochem. Biophys.*, 2005, 442, 222-228.
66. C. Hogstrand, P. Kille, R. I. Nicholson and K. M. Taylor, *Trends Mol. Med.*, 2009, 15, 101-111.
67. K. Girijashanker, L. He, M. Soleimani, J. M. Reed, H. Li, Z. Liu, B. Wang, T. P. Dalton and D. W. Nebert, *Mol. Pharmacol.*, 2008, 73, 1413-1423.
68. J. Dufner-Beattie, S. J. Langmade, F. Wang, D. Eide and G. K. Andrews, *J. Biol. Chem.*, 2003, 278, 50142-50150.

69. J. Dufner-Beattie, F. Wang, Y.-M. Kuo, J. Gitschier, D. Eide and G. K. Andrews, *J. Biol. Chem.*, 2003, 278, 33474-33481.
70. L. He, K. Girijashanker, T. P. Dalton, J. Reed, H. Li, M. Soleimani and D. W. Nebert, *Mol. Pharmacol.*, 2006, 70, 171-180.
71. Z. Liu, H. Li, M. Soleimani, K. Girijashanker, J. M. Reed, L. He, T. P. Dalton and D. W. Nebert, *Biochem. Biophys. Res. Commun.*, 2008, 365, 814-820.
72. P. Kaler and R. Prasad, *Am J. Physiol. Renal Ph.*, 2007, 292, F217-F229.
73. Y. Yu, A. Wu, Z. Zhang, G. Yan, F. Zhang, L. Zhang, X. Shen, R. Hu, Y. Zhang and K. Zhang, *J. Nutr. Biochem.*, 2013, 24, 1697-1708.
74. J. J. Pinilla-Tenas, B. K. Sparkman, A. Shawki, A. C. Illing, C. J. Mitchell, N. Zhao, J. P. Liuzzi, R. J. Cousins, M. D. Knutson and B. Mackenzie, *Am. J. Physiol. Cell Ph.*, 2011, 301, C862-C871.
75. S. Küry, B. Dréno, S. Bézieau, S. Giraudet, M. Kharfi, R. Kamoun and J.-P. Moisan, *Nat. Genet.*, 2002, 31, 239-240.
76. S. Schmitt, S. Küry, M. Giraud, B. Dréno, M. Kharfi and S. Bézieau, *Hum. Mutat.*, 2009, 30, 926-933.
77. V. Garza-Rodríguez, C. Liy-Wong, S. Küry, S. Schmitt, I. S. Jamall and J. Ocampo-Candiani, *Pediatr. Dermatol.*, 2015, 32, e124-e125.
78. W. Maret and H. H. Sandstead, *J. Trace Elem. Med. Biol.*, 2006, 20, 3-18.
79. A. S. Prasad, *Adv. Nutr.*, 2013, 4, 176-190.
80. T. Donahue and O. J. Hines, *Cancer Biol. Ther.*, 2010, 9, 243-245.
81. M. Li, Y. Zhang, Z. Liu, U. Bharadwaj, H. Wang, X. Wang, S. Zhang, J. P. Liuzzi, S.-M. Chang and R. J. Cousins, *Proc. Natl. Acad. Sci. USA*, 2007, 104, 18636-18641.
82. B. P. Weaver, Y. Zhang, S. Hiscox, G. L. Guo, U. Apte, K. M. Taylor, C. T. Sheline, L. Wang and G. K. Andrews, *PLoS One*, 2010, 5, e13158.
83. Y. Lin, Y. Chen, Y. Wang, J. Yang, V. F. Zhu, Y. Liu, X. Cui, L. Chen, W. Yan, T. Jiang, G. W. Hergenroeder, S. A. Fletcher, J. M. Levine, D. H. Kim, N. Tandon, J.-j. Zhu and M. Li, *Neuro Oncol.*, 2013, 15, 1008-1016.
84. Y. Zhang, U. Bharadwaj, C. D. Logsdon, C. Chen, Q. Yao and M. Li, *Clin. Cancer. Res.*, 2010, 16, 1423-1430.
85. S. Küry, M. Kharfi, R. Kamoun, A. Taïeb, E. Mallet, J. J. Baudon, C. Glastre, B. Michel, F. Sebag and D. Brooks, *Hum. Mutat.*, 2003, 22, 337-338.
86. A. Nakano, H. Nakano, K. Nomura, Y. Toyomaki and K. Hanada, *J. Invest. Dermatol.*, 2003, 120, 963-966.
87. S. Kilic, M. Giraud, S. Schmitt, S. Bézieau and S. Küry, *Br. J. Dermatol.*, 2007, 157, 386-387.
88. A. B. Hardy, K. J. Prentice, S. Froese, Y. Liu, G. K. Andrews and M. B. Wheeler, *PLoS One*, 2015, 10, e0119136.
89. Y. Liu, B. Batchuluun, L. Ho, D. Zhu, K. J. Prentice, A. Bhattacharjee, M. Zhang, F. Pourasgari, A. B. Hardy and K. M. Taylor, *J. Biol. Chem.*, 2015, 290, 18757-18769.
90. P. V. Hornbeck, B. Zhang, B. Murray, J. M. Kornhauser, V. Latham and E. Skrzypek, *Nucleic Acids Res.*, 2015, 43, D512-D520.
91. K. M. Taylor, S. Hiscox, R. I. Nicholson, C. Hogstrand and P. Kille, *Sci. Signal.*, 2012, 5, ra11.
92. S. S. Krishna, I. Majumdar and N. V. Grishin, *Nucleic Acids Res.*, 2003, 31, 532-550.
93. T. Kambe and G. K. Andrews, *Mol. Cell. Biol.*, 2009, 29, 129-139.
94. S. Ehsani, A. Salehzadeh, H. Huo, W. Reginold, C. L. Pocanschi, H. Ren, H. Wang, K. So, C. Sato and M. Mehrabian, *J. Mol. Biol.*, 2012, 422, 556-574.

95. F. Wang, B.-E. Kim, J. Dufner-Beattie, M. J. Petris, G. Andrews and D. J. Eide, *Hum. Mol. Genet.*, 2004, 13, 563-571.
96. X. Mao, B.-E. Kim, F. Wang, D. J. Eide and M. J. Petris, *J. Biol. Chem.*, 2007, 282, 6992-7000.
97. B.-E. Kim, F. Wang, J. Dufner-Beattie, G. K. Andrews, D. J. Eide and M. J. Petris, *J. Biol. Chem.*, 2004, 279, 4523-4530.
98. M. L. Bernhardt, B. Y. Kong, A. M. Kim, T. V. O'Halloran and T. K. Woodruff, *Biol. Reprod.*, 2012, 86, 114.
99. T. Fukada, S. Yamasaki, K. Nishida, M. Murakami and T. Hirano, *J. Biol. Inorg. Chem.*, 2011, 16, 1123-1134.
100. E. L. Que, R. Bleher, F. E. Duncan, B. Y. Kong, S. C. Gleber, S. Vogt, S. Chen, S. A. Garwin, A. R. Bayer, V. P. Dravid, T. K. Woodruff and T. V. O'Halloran, *Nat. Chem.*, 2015, 7, 130-139.
101. C. Lorenz, M. Pusch and T. J. Jentsch, *Proc. Natl. Acad. Sci. USA*, 1996, 93, 13362-13366.
102. R. Richards and R. E. Dempski, *J. Vis. Exp.*, 2011, e2627.
103. R. A. Valentine, K. A. Jackson, G. R. Christie, J. C. Mathers, P. M. Taylor and D. Ford, *J. Biol. Chem.*, 2007, 282, 14389-14393.
104. R. D. Palmiter and S. D. Findley, *EMBO J.*, 1995, 14, 639.
105. G. Dahl, E. Levine, C. Rabadan-Diehl and R. Werner, *Eur. J. Biochem.*, 1991, 197, 141-144.
106. S. Sheng, C. J. Perry and T. R. Kleyman, *J. Biol. Chem.*, 2002, 277, 50098-50111.
107. C. Clarke, C. Benham, A. Bridges, A. George and H. Meadows, *J. Physiol.*, 2000, 523, 697-703.
108. J. G. Reyes, *Am. J. Physiol. Cell Ph.*, 1996, 270, C401-C410.
109. L. C. Costello, C. C. Fenselau and R. B. Franklin, *J. Inorg. Biochem.*, 2011, 105, 589-599.
110. J. F. Da Silva and R. J. P. Williams, *The biological chemistry of the elements: the inorganic chemistry of life*, Oxford University Press, 2001.
111. V. L. Mendoza and R. W. Vachet, *Anal. Chem.*, 2008, 80, 2895-2904.
112. A. Gupta and S. Lutsenko, *Future Med. Chem.*, 2009, 1, 1125-1142.
113. H. Zhao and D. Eide, *Proc. Natl. Acad. Sci. USA*, 1996, 93, 2454-2458.
114. H. Zhao and D. Eide, *J. Biol. Chem.*, 1996, 271, 23203-23210.
115. K. T. Simons, I. Ruczinski, C. Kooperberg, B. A. Fox, C. Bystroff and D. Baker, *Proteins: Struct. Funct. Bioinform.*, 1999, 34, 82-95.
116. H. Kamisetty, S. Ovchinnikov and D. Baker, *Proc. Natl. Acad. Sci. USA*, 2013, 110, 15674-15679.
117. A. R. Ortiz, A. Kolinski and J. Skolnick, *J. Mol. Biol.*, 1998, 277, 419-448.
118. K. Katoh, K. Misawa, K. i. Kuma and T. Miyata, *Nucleic Acids Res.*, 2002, 30, 3059-3066.
119. R. C. Edgar, *Nucleic Acids Res.*, 2004, 32, 1792-1797.
120. C. B. Do, M. S. Mahabhashyam, M. Brudno and S. Batzoglou, *Genome Res.*, 2005, 15, 330-340.
121. A. Krogh, M. Brown, I. S. Mian, K. Sjölander and D. Haussler, *J. Mol. Biol.*, 1994, 235, 1501-1531.
122. S. Raman, R. Vernon, J. Thompson, M. Tyka, R. Sadreyev, J. Pei, D. Kim, E. Kellogg, F. DiMaio, O. Lange, L. Kinch, W. Sheffler, B. H. Kim, R. Das, N. V. Grishin and D. Baker, *Proteins: Struct. Funct. Bioinform.*, 2009, 77, 89-99.
123. N. Coudray, S. Valvo, M. Hu, R. Lasala, C. Kim, M. Vink, M. Zhou, D. Provasi, M. Filizola, J. Tao, J. Fang, P. A. Penczek, I. Ubarretxena-Belandia and D. L. Stokes, *Proc. Natl. Acad. Sci. USA*, 2013, 110, 2140-2145.
124. J. Söding, *Bioinformatics*, 2005, 21, 951-960.

125. P. Barth, J. Schonbrun and D. Baker, *Proc. Natl. Acad. Sci. USA*, 2007, 104, 15682-15687.
126. V. Yarov-Yarovoy, P. G. DeCaen, R. E. Westenbroek, C.-Y. Pan, T. Scheuer, D. Baker and W. A. Catterall, *Proc. Natl. Acad. Sci. USA*, 2012, 109, E93-E102.
127. Q. Cong and N. V. Grishin, *BMC Biol.*, 2012, 10, 82.
128. O. F. Lange, P. Rossi, N. G. Sgourakis, Y. Song, H.-W. Lee, J. M. Aramini, A. Ertekin, R. Xiao, T. B. Acton, G. T. Montelione and D. Baker, *Proc. Natl. Acad. Sci. USA*, 2012, 109, 10873-10878.
129. Y. Zhang and J. Skolnick, *Proteins: Struct. Funct. Bioinform.*, 2004, 57, 702-710.
130. F. DiMaio, A. Leaver-Fay, P. Bradley, D. Baker and I. André, *PLoS One*, 2011, 6, e20450.
131. K. L. Dürr, N. N. Tavraz, R. E. Dempksi, E. Bamberg and T. Friedrich, *J. Biol. Chem.*, 2009, 284, 3842-3854.
132. M. Lazdunski, C. Petitclerc, D. Chappelet and C. Lazdunski, *Eur. J. Biochem.*, 1971, 20, 124-139.
133. D. Sanders, *J. Membr. Biol.*, 1986, 90, 67-87.
134. J. Xu and Y. Zhang, *Bioinformatics*, 2010, 26, 889-895.
135. Y. Zhang and J. Skolnick, *Nucleic Acids Res.*, 2005, 33, 2302-2309.
136. T. A. Hopf, L. J. Colwell, R. Sheridan, B. Rost, C. Sander and D. S. Marks, *Cell*, 2012, 149, 1607-1621.
137. T. Nugent and D. T. Jones, *Proc. Natl. Acad. Sci. USA*, 2012, 109, E1540-E1547.
138. C. H. Wu, R. Apweiler, A. Bairoch, D. A. Natale, W. C. Barker, B. Boeckmann, S. Ferro, E. Gasteiger, H. Huang, R. Lopez, M. Magrane, M. J. Martin, R. Mazumder, C. O'Donovan, N. Redaschi and B. Suzek, *Nucleic Acids Res.*, 2006, 34, D187-D191.
139. D. Kozma, I. Simon and G. E. Tusnády, *Nucleic Acids Res.*, 2013, 41, D524-D529.
140. B. P. Pedersen, H. Kumar, A. B. Waight, A. J. Risenmay, Z. Roe-Zurz, B. H. Chau, A. Schlessinger, M. Bonomi, W. Harries, A. Sali, A. K. Johri and R. M. Stroud, *Nature*, 2013, 496, 533-536.
141. L. R. Gabriel, S. Wu and H. E. Melikian, *J. Vis. Exp.*, 2013.
142. Y. Wei and D. Fu, *J. Biol. Chem.*, 2006, 281, 23492-23502.
143. R. E. Dempksi, *Curr Top Membr*, 2012, 69, 221-245.
144. W. Lin, J. Chai, J. Love and D. Fu, *J. Biol. Chem.*, 2010, 285, 39013-39020.
145. M. G. Madej, S. Dang, N. Yan and H. R. Kaback, *Proc. Natl. Acad. Sci. USA*, 2013, 110, 5870-5874.
146. M. G. Madej and H. R. Kaback, *Proc. Natl. Acad. Sci. USA*, 2013, 110, E4831-E4838.
147. Å. Västermark, B. Lunt and M. Saier, *J. Mol. Microbiol. Biotechnol.*, 2014, 24, 82-90.
148. Å. Västermark and M. H. Saier, *Proc. Natl. Acad. Sci. USA*, 2014, 111, E1162-E1163.
149. V. N. Uversky, *Protein Sci.*, 2013, 22, 693-724.
150. T. Flock, R. J. Weatheritt, N. S. Latysheva and M. M. Babu, *Curr. Opin. Struct. Biol.*, 2014, 26, 62-72.
151. B. Xue, L. Li, S. O. Meroueh, V. N. Uversky and A. K. Dunker, *Mol Biosyst*, 2009, 5, 1688-1702.
152. Y. Minezaki, K. Homma and K. Nishikawa, *J. Mol. Biol.*, 2007, 368, 902-913.
153. J. Habchi, P. Tompa, S. Longhi and V. N. Uversky, *Chem. Rev.*, 2014, 114, 6561-6588.
154. L. A. Lichten and R. J. Cousins, *Annu. Rev. Nutr.*, 2009, 29, 153-176.
155. J. Prilusky, C. E. Felder, T. Zeev-Ben-Mordehai, E. H. Rydberg, O. Man, J. S. Beckmann, I. Silman and J. L. Sussman, *Bioinformatics*, 2005, 21, 3435-3438.
156. R. Kim, S. J. Sandler, S. Goldman, H. Yokota, A. J. Clark and S.-H. Kim, *Biotechnol. Lett.*, 1998, 20, 207-210.
157. S. Yi, A. Brickenden and W.-Y. Choy, *Protein Expr. Purif.*, 2008, 57, 1-8.

158. F. Campos, G. Guillén, J. L. Reyes and A. A. Covarrubias, *Protein Expr. Purif.*, 2011, 80, 47-51.
159. S. C. Burdette, G. K. Walkup, B. Spingler, R. Y. Tsien and S. J. Lippard, *J. Am. Chem. Soc.*, 2001, 123, 7831-7841.
160. G. George and I. Pickering, EXAFSPAK: A Suite of Computer Programs for Analysis of X-ray Absorption Spectra, Stanford Synchrotron Radiation Laboratory, Stanford, CA, 2000.
161. J. Rehr and A. Ankudinov, *J. Synchrotron. Radiat.*, 2001, 8, 61-65.
162. P. J. Riggs-Gelasco, T. L. Stemmler and J. E. Penner-Hahn, *Coord. Chem. Rev.*, 1995, 144, 245-286.
163. K. Z. Bencze, K. C. Kondapalli and T. L. Stemmler, in *Applications of Physical Methods to Inorganic and Bioinorganic Chemistry*, 2007, pp. 513-528.
164. J. J. Cotelesage, M. J. Pushie, P. Grochulski, I. J. Pickering and G. N. George, *J. Inorg. Biochem.*, 2012, 115, 127-137.
165. P. Tompa, *Trends Biochem. Sci.*, 2002, 27, 527-533.
166. L. M. De León-Rodríguez, A. J. Lubag, J. A. López, G. Andreu-de-Riquer, J. C. Alvarado-Monzón and A. D. Sherry, *Med. Chem. Commun.*, 2012, 3, 480-483.
167. C. A. Blasie and J. M. Berg, *Inorg. Chem.*, 2000, 39, 348-351.
168. T. L. Stemmler, T. M. Sossong, J. I. Goldstein, D. E. Ash, T. E. Elgren, D. M. Kurtz and J. E. Penner-Hahn, *Biochemistry*, 1997, 36, 9847-9858.
169. M. Laitaoja, J. Valjakka and J. Jänis, *Inorg. Chem.*, 2013, 52, 10983-10991.
170. G. Meloni, K. Zovo, J. Kazantseva, P. Palumaa and M. Vašák, *J. Biol. Chem.*, 2006, 281, 14588-14595.
171. H. E. Parge, R. A. Hallewell and J. A. Tainer, *Proc. Natl. Acad. Sci. USA*, 1992, 89, 6109-6113.
172. T. Kočańczyk, A. Drozd and A. Krężel, *Metallomics*, 2015, 7, 244-257.
173. M. Fuxreiter and P. Tompa, *Adv. Exp. Med. Biol.*, 2012, 725, 1-14.
174. L. M. Brill, W. Xiong, K.-B. Lee, S. B. Ficarro, A. Crain, Y. Xu, A. Terskikh, E. Y. Snyder and S. Ding, *Cell Stem Cell*, 2009, 5, 204-213.
175. P. Radivojac, V. Vacic, C. Haynes, R. R. Cocklin, A. Mohan, J. W. Heyen, M. G. Goebel and L. M. Iakoucheva, *Proteins: Struct. Funct. Bioinform.*, 2010, 78, 365-380.
176. S. Prakash, L. Tian, K. S. Ratliff, R. E. Lehotzky and A. Matouschek, *Nat. Struct. Mol. Biol.*, 2004, 11, 830-837.
177. C. J. Brown, A. K. Johnson, A. K. Dunker and G. W. Daughdrill, *Curr. Opin. Struct. Biol.*, 2011, 21, 441-446.
178. G. R. Dubyak, *Adv. Physiol. Ed.*, 2004, 28, 143-154.
179. A. Penna, A. Demuro, A. V. Yeromin, S. L. Zhang, O. Safrina, I. Parker and M. D. Cahalan, *Nature*, 2008, 456, 116-120.
180. M. Mense, P. Vergani, D. M. White, G. Altberg, A. C. Nairn and D. C. Gadsby, *EMBO J.*, 2006, 25, 4728-4739.